Complex Image Theory and Applications in Boundary Detection in Geo-Steering Using Data from a Directional Resistivity LWD Tool

A Dissertation

Presented to

The Faculty of the Department of Electrical and Computer Engineering

University of Houston

In Partial Fulfillment

of the Requirements for the Degree

Doctor of Philosophy

in Electrical Engineering

by

Jing Wang

May 2014

Complex Image Theory and Applications in Boundary Detection in Geo-Steering Using Data from a Directional Resistivity LWD Tool

Jing Wang

Approved:

Chair of the Committee
Richard C. Liu, Professor
Electrical and Computer Engineering

Committee Members:

Donald R. Wilton, Professor
Electrical and Computer Engineering

David R. Jackson, Professor
Electrical and Computer Engineering

Thomas K. Holley, Professor
Petroleum Engineering

Heidar Malki, Professor
Engineering Technology

Suresh K. Khator, Associate Dean
Cullen College of Engineering

Badrinath Roysam, Professor and Chair
Electrical and Computer Engineering

Acknowledgements

This dissertation would not have been possible without the support of many people. First of all, the sincere gratitude should be given to my adviser Professor Dr. Richard C. Liu. His advice, encouragement, prodding, and example have challenged me to grow tremendously. I am very grateful for all the time and effort that he has devoted to me over the past several years. The knowledge and experience I got will be the valuable assets of the future life.

I would also like to thank the other members of my committee, Dr. Donald R. Wilton, Dr. David R. Jackson, Dr. Heidar Malki, and Dr. Thomas K. Holley, for the comments and suggestions that have challenged and encouraged me in my work.

Secondly, I want to thank to all the individuals for sharing the literatures and providing invaluable assistance during my study in University of Houston: Yajuan Kong, Zhijuan Zhang, Changming Lin, Boyuan Yu, Yinxi Zhang, Mengsu Zhou, Bo Gong, Aobo Jin, Dr. Ning Yuan and Dr. Xiaochun Nie. It is really a pleasure to work with you. Special thanks to Donghui Han. Thanks to him for being all together with me and supporting me.

Finally, I thank my beloved families. Thanks for their understanding and endless support, through the duration of my studies.

Complex Image Theory and Applications in Boundary Detection in Geo-Steering Using Data from a Directional Resistivity LWD Tool

An Abstract of a Dissertation

Presented to

The Faculty of the Department of Electrical and Computer Engineering

University of Houston

In Partial Fulfillment

of the Requirements for the Degree

Doctor of Philosophy

in Electrical Engineering

by

Jing Wang

May 2014

Abstract

Geo-steering is the process of controlling and adjusting the direction of the drilling bit in a horizontal or deviated well, in real time to keep the drilling in the desired zone. One of the most challenging steps of Geo-steering is the boundary detection, which is to calculate the distance from the bit to upper or lower boundary based on the measured data from an LWD tool. Generally, calculating the distance from bit to boundary is an inversion problem. To speed up the inversion process, a fast forward modeling algorithm is critical.

In this study, the Complex Image Theory applied in finite conductivity layered media is derived to speed up the forward modeling of the geo-steering system. Two approximation results are shown in detail in dealing with the two general cases of dipole radiation. The first one is when the dipole is placed in the relative high resistive layer. The second one is when the dipole is placed in the relative high conductive layer. The algorithm is tested in both two-layer and three-layer cases and in high deviated well. Compared with the results from the full solution (the result from INDTRI), the Complex Image Theory has satisfactory accuracy and when the number of logging points is 600,000, it is 160 times faster. Error only exists in area two ft. or three ft. away from boundary. By considering the power of real source, the possibility of real application is investigated. The tolerance in different frequencies, spacing and conductivity

combinations is discussed too. The simulation results show that the Complex Image Theory works in most geo-steering situations. The proposed method reduces the simulation time and improves the real-time performance of the control system.

The distance inversion is developed for two-layer formation. The inversion results show that the algorithm works well even at the position 10 ft. away from the boundary. The anti-noise capacity of the propose method is measured by further involving random white noise in the simulation scenario. The relative error of simulation is as low as 5% in the area six ft. away from the boundary. With higher conductivity contrast formation, the proposed method is even more robust.

Table of Contents

Acknowledgements v

Abstract viii

Table of Contents x

List of Figures xiii

List of Tables xvii

Chapter 1 Introduction 1

1.1 Directional Resistivity Logging Tool 1

1.1.1 Principle of Triaxial Logging Tool 2

1.1.2 Propagation Logging Tool Configuration 4

1.1.3 Logging While Drilling (LWD) Tool Measurements 5

1.2 Literature Survey 6

1.3 Dissertation Objective 7

1.4 Overview of the Dissertation 8

1.5 Main Contributions of the Dissertation 9

Chapter 2 Theory of Forward Modeling 10

2.1 Magnetic Dipoles in Homogeneous Medium 10

2.2 Review of Traditional Image Theory 11

2.3 Complex Image Theory in Non-perfect Medium 13

2.3.1 Horizontal Dipole in Half Space 14

2.3.2 Dipole in Lossless Half Space 15

2.3.3 Dipole in the Dissipative Media 18

Chapter 3 Simulation Results and Discussion 23

3.1 1D Formation Model 23

3.2 Tool Configuration 24

3.3 Simulation Results 25

3.3.1 $R_1 = R_3 = 1$ Ohm.m, $R_3 = 100$ Ohm.m 25

3.3.2 $R_1 = R_3 = 1$ Ohm.m, $R_3 = 10$ Ohm.m 30

3.3.3 $R_1 = R_3 = 100$ Ohm.m, $R_2 = 1$ Ohm.m 37

3.3.4 $R_1 = 1$ Ohm.m, $R_1 = 20$ Ohm.m, $R_1 = 0.5$ Ohm.m 41

3.4 Discussion 46

3.4.1 Effects of Conductivity Contrast 47

3.4.2 Frequency 49

3.4.3 Spacing 50

3.4.4 Calculation Speed 53

3.4.5 Logging with high deviated angle 54

Chapter 4 Boundary Distance Inversion 60

4.1 Theory of Inversion 60

4.2 Workflow of Inversion Problem 60

4.3 Processing Flow of Boundary Detection in Geo-steering................................. 61

4.4 Bolzano Bisection Method.. 62

4.5 Simulation Results 63

4.5.1 Sensitivity of Depth 63

4.5.2 R_1 = 1 Ohm.m, R_2 = 10 Ohm.m.. 65

4.5.3 R_1 = 1 Ohm.m, R_2 = 100 Ohm.m.. 70

4.6 Simulation Results with Noise added 72

4.6.1 R_1 = 1 Ohm.m, R_2 = 10 Ohm.m.. 73

4.6.2 R_1 = 1 Ohm.m, R_2 = 100 Ohm.m.. 75

Chapter 5 Conclusion 78

Reference 80

Appendix I IMAGE 12 USER MANUAL... 82

List of Figures

Figure 1.1 Basic structure of triaxial tool 2

Figure 1.2 Tool configurations of directional resistivity tool (a) Tool with tilted antennas (b) Tool with orthogonal antennas 5

Figure 2.1 Image theory of PEC interface 12

Figure 2.2 Summary of image theory 13

Figure 2.3 A horizontal dipole placed in half space model 14

Figure 2.4 Two-layer equivalent model by applying the image theory 17

Figure 2.5 Three-layer equivalent model by applying the image theory 18

Figure 3.1 Three-layer model 23

Figure 3.2 Azitrack tool configuration.. 24

Figure 3.3 Tool response H_{zx} component ($\sigma_1 = \sigma_3 = 1, \sigma_2 = 0.01$, 2MHz, long) 26

Figure 3.4 Phase difference and attenuation ($\sigma_1 = \sigma_3 = 1, \sigma_2 = 0.01$, 2 MHz, long)........ 26

Figure 3.5 Tool response Hzx component ($\sigma_1 = \sigma_3 = 1, \sigma_2 = 0.01$, 2 MHz, short).......... 27

Figure 3.6 Phase difference and attenuation ($\sigma_1 = \sigma_3 = 1, \sigma_2 = 0.01$, 2 MHz, short)....... 28

Figure 3.7 Tool response H_{zx} component ($\sigma_1 = \sigma_3 = 1, \sigma_2 = 0.01$, 400 KHz, long)......... 29

Figure 3.8 Phase difference and attenuation ($\sigma_1 = \sigma_3 = 1, \sigma_2 = 0.01$, 400 KHz, long) 29

Figure 3.9 Tool response H_{zx} component ($\sigma_1 = \sigma_3 = 1, \sigma_2 = 0.01$, 400 KHz, short)........ 31

Figure 3.10 Phase difference and attenuation ($\sigma_1 = \sigma_3 = 1, \sigma_2 = 0.01$, 400 KHz, short) . 31

Figure 3.11 Tool response H_{zx} component ($\sigma_1 = \sigma_3 = 1, \sigma_2 = 0.1$, 2 MHz, long) 32

Figure 3.12 Phase difference and attenuation ($\sigma_1 = \sigma_3 = 1$, $\sigma_2 = 0.1$, 2 MHz, long) 32

Figure 3.13 Tool response H_{zx} component ($\sigma_1 = \sigma_3 = 1$, $\sigma_2 = 0.1$, 2 MHz, short) 33

Figure 3.14 Phase difference and attenuation ($\sigma_1 = \sigma_3 = 1$, $\sigma_2 = 0.1$, 2 MHz, short)....... 34

Figure 3.15 Tool response H_{zx} component ($\sigma_1 = \sigma_3 = 1$, $\sigma_2 = 0.1$, 400 KHz, long)......... 34

Figure 3.16 Phase difference and attenuation ($\sigma_1 = \sigma_3 = 1$, $\sigma_2 = 0.1$, 400 KHz, long).... 35

Figure 3.17 Tool response H_{zx} component ($\sigma_1 = \sigma_3 = 1$, $\sigma_2 = 0.1$, 400 KHz, short)........ 35

Figure 3.18 Phase difference and attenuation ($\sigma_1 = \sigma_3 = 1$, $\sigma_2 = 0.1$, 400 KHz, short) ... 36

Figure 3.19 Tool response H_{zx} component ($\sigma_1 = \sigma_3 = 0.01$, $\sigma_2 = 1$, 2 MHz, long)........... 37

Figure 3.20 Phase difference and attenuation ($\sigma_1 = \sigma_3 = 0.01$, $\sigma_2 = 1$, 2 MHz, long) 38

Figure 3.21 Tool response H_{zx} component ($\sigma_1 = \sigma_3 = 0.01$, $\sigma_2 = 1$, 2 MHz, short).......... 38

Figure 3.22 Phase difference and attenuation ($\sigma_1 = \sigma_3 = 0.01$, $\sigma_2 = 1$, 2 MHz, short) 39

Figure 3.23 Tool response H_{zx} component ($\sigma_1 = \sigma_3 = 0.01$, $\sigma_2 = 1$, 400 KHz, long)........ 39

Figure 3.24 Phase difference and attenuation ($\sigma_1 = \sigma_3 = 0.01$, $\sigma_2 = 1$, 400 KHz, long)... 40

Figure 3.25 Tool response H_{zx} component ($\sigma_1 = \sigma_3 = 0.01$, $\sigma_2 = 1$, 400 KHz, short)....... 40

Figure 3.26 Phase difference and attenuation ($\sigma_1 = \sigma_3 = 0.01$, $\sigma_2 = 1$, 400 KHz, short).. 41

Figure 3.27 Tool response H_{zx} component ($\sigma_1 = 1, \sigma_2 = 0.05, \sigma_3 = 2$, 2 MHz, long)........ 42

Figure 3.28 Phase difference and attenuation ($\sigma_1 = 1, \sigma_2 = 0.05, \sigma_3 = 2$, 2 MHz, long)... 43

Figure 3.29 Tool response H_{zx} component ($\sigma_1 = 1, \sigma_2 = 0.05, \sigma_3 = 2$, 2 MHz, short)....... 43

Figure 3.30 Phase difference and attenuation ($\sigma_1 = 1, \sigma_2 = 0.05, \sigma_3 = 2$, 2 MHz, short).. 44

Figure 3.31 Tool response H_{zx} component ($\sigma_1 = 1, \sigma_2 = 0.05, \sigma_3 = 2$, 400 KHz, long) 44

Figure 3.32 Phase difference and attenuation ($\sigma_1 = 1, \sigma_2 = 0.05, \sigma_3 = 2$, 400 KHz, long) 45

Figure 3.33 Tool response H_{zx} component ($\sigma_1 = 1, \sigma_2 = 0.05, \sigma_3 = 2$, 400 KHz, short) ... 45

Figure 3.34 Phase difference and attenuation ($\sigma_1 = 1, \sigma_2 = 0.05, \sigma_3 = 2$, 400 KHz, short)46

Figure 3.35 Observation point 1ft. away from boundary... 47

Figure 3.36 Absolute error of 2MHz tool at 1ft away from boundary 48

Figure 3.37 Relative error of 2 MHz tool at 1ft away from boundary............................. 48

Figure 3.38 Voltage signal generated by cross component H_{zx} of single turn transmitter ($\sigma_1 = \sigma_3 = 1, \sigma_2 = 0.01$) 50

Figure 3.39 Two-layer model with boundary at z = 0ft.. 50

Figure 3.40 Cross component response vs. 100nV in different spacing (400 KHz) 51

Figure 3.41 Cross component response vs. 100nV in different spacing in log scale (400 KHz).. 52

Figure 3.42 Cross component response vs. 100nV in different spacing (2 MHz)............ 52

Figure 3.43 Cross component response vs. 100nV in different spacing in log scale (2MHz) 53

Figure 3.44 High deviated well in 3-layer formation 54

Figure 3.45 Tool response H_{zx} component (Dipping = 85^o) 55

Figure 3.46 Tool response H_{zx} component (Dipping = 75^o) 56

Figure 3.47 Tool response H_{zx} component (Dipping = 65^o) 57

Figure 3.48 Tool response H_{zx} component (Dipping = 60^o) 58

Figure 3.49 Tool response H_{zx} component in the middle layer (Dipping = 60^o) 58

Figure 4.1 Flow chart of inversion problem 61

Figure 4.2 Boundary distance inversion flow 61

Figure 4.3 Testing model of inversion processing (R_1:R_2 = 1:10) 63

Figure 4.4 Depth sensitivity of H_{zx} (0ft. to 10 ft.) 64

Figure 4.5 Depth sensitivity of H_{zx} (4ft. to 10 ft.) 65

Figure 4.6 Zoom in cross component H_{zx} of tool response 67

Figure 4.7 Amplitude of the cross component H_{zx} 68

Figure 4.8 Zoom in amplitude of the cross component H_{zx} 68

Figure 4.9 Relative error of the inversion results (H_{zx} _abs, R_1:R_2 = 1:10) 69

Figure 4.10 Testing model of inversion processing (R_1:R_2 = 1:100) 70

Figure 4.11 Relative error of the inversion results (H_{zx} _real, R_1:R_2 = 1:100) 71

Figure 4.12 Comparison of the relative error in different formation 72

Figure 4.13 Relative error with different noise added (R_1:R_2 = 1:10) 74

Figure 4.14 Relative error with different noise added (R_1:R_2 = 1:100) 77

Figure I.1 A tool is located horizontally in the production layer 82

Figure I.2 Two-layer model 86

Figure I.3 *zx* component of the 2-layered model 87

Figure I.4 Three-layer model 88

Figure I.5 *zx* component of the 3-layered model 89

List of Tables

Table 1 Computation speed testing 54

Table 2 Distance inversion table (H_{zx} _real, R_1:R_2 = 1:10) 66

Table 3 Distance inversion table (H_{zx} _abs, R_1:R_2 = 1:10) 69

Table 4 Distance inversion table (H_{zx} _abs, R_1:R_2 = 1:100) 71

Table 5 Distance inversion table with 1% noise added (H_{zx} _abs, R_1:R_2 = 1:10) 74

Table 6 Distance inversion table with 5% noise added (H_{zx} _abs, R_1:R_2 = 1:10) 74

Table 7 Distance inversion table with 5% noise added (H_{zx} _abs, R_1:R_2 = 1:100) 76

Chapter 1 Introduction

Real time geo-steering system is playing a more and more important role in oil and gas explorations. The purpose of real-time geo-steering is to steer the drilling system inside the production layer and in between the shoulder beds. A measurement of how far the bit is from the boundary is needed in such control. Directional resistivity has been used in geo-steering in past years as the measurement to compute the distance to bed, dipping angles and anisotropy, and others.

1.1 Directional Resistivity Logging Tool

Due to the anisotropy of formation, the resistivity varies differently in different directions, thus the concept Directional Resistivity. Anisotropy (the variation of properties with direction) usually has two classes. One is called particle shape anisotropy, most commonly found in shales. Sands and carbonates may also have such property. It is caused by the oriented arrangement of solid particle, whose orientation is usually parallel to the bedding plane. This results the electric current to flow more easily parallel to the bedding plane than perpendicular to it. The second anisotropy is due to the thin layer scale structure. The shale has high conductivity, however sand has high resistivity. When they are combined to format the thin layered structure, the horizontal resistivity R_h is different from the vertical resistivity R_v.

1.1.1 Principle of Triaxial Logging Tool

The triaxial logging tool is designed to measure all necessary electrical components of magnetic field in anisotropy formation, which include three pairs of transmitters and main receivers, shown in Figure 1.1 [1].

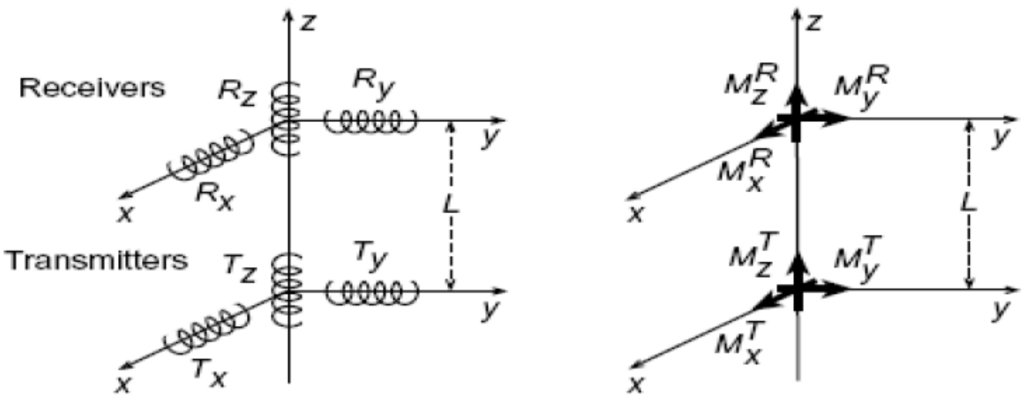

Figure 1.1 Basic structure of triaxial tool

For spacing of each transmitter – receiver pair, a 3*3 tensor of magnetic field is measured

$$\bar{H} = \begin{bmatrix} H_x^x & H_x^y & H_x^z \\ H_y^x & H_y^y & H_y^z \\ H_z^x & H_z^y & H_z^z \end{bmatrix}, \tag{1}$$

where H_i^j is the magnetic field radiated by the i-th transmitter and received by j-th receiver. Because the magnetic field is proportional to the apparent conductivity of the formation, by multiplying one coefficient matrix **K**, a tensor of apparent conductivities σ_{app} is given by

$$\sigma_{app} = K\overline{H} = \begin{bmatrix} \sigma_{app\,x}^{\;\;x} & \sigma_{app\,x}^{\;\;y} & \sigma_{app\,x}^{\;\;z} \\ \sigma_{app\,y}^{\;\;x} & \sigma_{app\,y}^{\;\;y} & \sigma_{app\,y}^{\;\;z} \\ \sigma_{app\,z}^{\;\;x} & \sigma_{app\,z}^{\;\;y} & \sigma_{app\,z}^{\;\;z} \end{bmatrix}. \tag{2}$$

For transverse isotropy (TI) formation, the tensor is simplified into

$$\sigma_{TI\_app} = \begin{bmatrix} \sigma_{app\,x}^{\;\;x} & 0 & 0 \\ 0 & \sigma_{app\,x}^{\;\;x} & 0 \\ 0 & 0 & \sigma_{app\,z}^{\;\;z} \end{bmatrix}. \tag{3}$$

For bi-isotropic (BI) Formation, the tensor is simplified into

$$\sigma_{BI\_app} = \begin{bmatrix} \sigma_{app\,x}^{\;\;x} & 0 & 0 \\ 0 & \sigma_{app\,y}^{\;\;y} & 0 \\ 0 & 0 & \sigma_{app\,z}^{\;\;z} \end{bmatrix}. \tag{4}$$

For isotropic formation, the tensor is simplified into one parameter σ_{app}.

Triaxial logging tool is designed to measure the anisotropy property of the formation, in the application of geo-steering, we take advantage of the boundary sensitivity of the cross component. By analyzing the received signal of cross component, the boundary distance can be calculated. If the logging tool is placed in a homogenous isotropy formation, because x, y and z directions are orthogonal, the receiver towards each direction can only receive the signal from the transmitter with the same direction. However, if there is one boundary, due to the reflection, the polarization will be different. Then, the off-diagonal components will be nonzero. The amplitude and phase of the received off-diagonal components will be varying at different observation positions. Reversely, if the off-diagonal components can be measured firstly, the boundary information can be deduced accordingly.

1.1.2 Propagation Logging Tool Configuration

Two configurations of directional resistivity tool are used generally nowadays, as shown in Figure 1.2. One is an extension of the conventional propagation resistivity tool, shown in Figure 1.2(a). Two titled receiver antennas inclined 45^o with respect to the tool axis are added. This configuration is used by Schlumberger [2-3] and Halliburton [2]. This new deep directional EM tool has both horizontal and vertical sets of antennas measuring both R_h and R_v. The resistivity is calculated from the voltage ratio of the two receiver antennas. The other configuration, shown in Figure 1.2(b), used by Baker Hughes [4], is proposed by Wang. It employs orthogonal, or fully tilted, transmitter and receiver antennas. The orthogonal configuration provides only directional sensitive information and is free of direct coupling between the transmitter and receiver antennas. Instead of measuring the voltage ratio, this new approach could read the directly voltage signal from a main receiver antenna and a bucking antenna, which allows removal of many environment effects, such as tool eccentricity and tool bending.

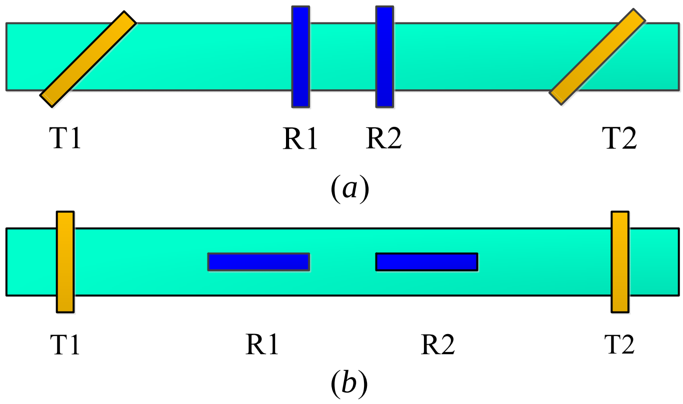

Figure 1.2 Tool configurations of directional resistivity tool (a) Tool with tilted antennas (b) Tool with orthogonal antennas

As shown in Figure 1.2, both configurations are symmetric. The symmetric configuration enables removal or amplification of sensitivities to dip, anisotropy, and nearby boundaries, resulting in simplified responses and interpretation. Because the transmitter antenna and receiver antennas are not orthogonal, the measured response is a combination of the direction-sensitive information and direction-in-sensitive from the total measurement. There is direct coupling between the transmitter and receiver antennas.

1.1.3 Logging While Drilling (LWD) Tool Measurements

Compared with induction tool, the LWD is working in a relatively higher frequency range, which comes with more loss of energy. For higher accuracy and sensitivity, the phase shift and amplitude ratio of two receivers are introduced as an additional measurement. A conversion table from phase shift and amplitude to the apparent conductivity of the formation will be set up for each frequency and spacing. By look up the received phase shift and amplitude ratio in the conversion table, the apparent conductivity of the formation can be obtained.

1.2 Literature Survey

Traditionally, the boundary information is estimated based on comparing the resistivity response in different spacings of the LWD tool. Boundary responses of the LWD tool from resistive-to-conductive and conductive-to-resistive formation structures are different. By comparing these responses and analyzing together with seismic mapping, the position of the boundary and the distance between the bit and boundaries can be predicted [5-6]. However, due to the limited accuracy of seismic data and the qualitative nature of this method, its result is usually not satisfactory. Therefore, the real time control of the drilling system is largely dependent on the experience of the operators.

Bittar presents a differential measurement approach, based on the standard propagation resistivity tool [7], by placing two tilted antennas on a drill string to get the bed information from the ratio of two signals at different tool azimuth angles. The measurements contain both the direction-sensitive information and direction-insensitive information. In 2006, Wang proposes a new approach that employs an orthogonal transmitter and receiver antennas [4]. The voltage signals from a main receiver antenna and a bucking antenna directly represent the only directional sensitive information.

To meet the real-time requirement of industry, a fast forward modeling method is desirable. Currently, most of the forward modeling methods are based on full solution. In 2005, Omeragic proposes a model-based (parametric) inversion method to detect distances to both upper and lower shoulder beds [3]. In 2006, Wang shows the inversion of distance to a bed based on a full 1-D forward model [4]. In the same publication, Wang first adopts the image theory to interpret the directional resistivity measurement and shows that the image theory can be used in a quantitative computation tool [4].

The conventional image theory is used to simplify the inhomogeneous problem to a homogenous problem when the source is over the perfect electric conductor (PEC) or perfect magnetic conductor (PMC) interface. In 1969, Wait extends the approximate discrete image theory to a finite conducting interface [8]. Then Bannister further develops this extension to arbitrary sources [9]. In 1984, I. V. Lindell and E. Alanen post the continuous exact image source over a dissipate plane [10].

The application of the image source could extremely simplify the forward modeling and speed up the calculation. Wang publishes more cases verifying the feasibility of the complex image in well-logging [11]. This method is powerful for both qualitative and quantitative analysis of a logging response in a stratified formation.

1.3 Dissertation Objective

The controlling process of geo-steering can be modeled as a feedback system. There are mainly two parts in it. The first one is to get the received signal from the tool and the second one is to recover the boundary information from the received signal. This dissertation focuses on the second part.

Much work have been done and methods been proposed in controlling of steering. However, these efforts mainly focus on estimation or rely on searching in table with complicated data sets and interpolations. To the best of our knowledge, no one tries to inverse out the exact distance value. Previous study has proved that it's possible to apply the image theory to the simulation of tool response. However, application of this theory is only limited in the case when the tool is placed in the relative high resistive layer, which is not practical in real application.

In this dissertation, we will propose a fast simulation algorithm based on the complex image theory, which not only can be used into the case when the tool is placed in the relative high resistive layer, but also works in the case when the tool is placed in the relative high conductive layer. The forward modeling of formation speeds up greatly by using the proposed theory. The time used to inverse the boundary distance will thus be reduced extremely.

1.4 Overview of the Dissertation

The dissertation is organized as following. Chapter 1 gives a brief introduction to the background of the problem, the research status and the objective of this dissertation.

Chapter 2 derives the theory used in to the forward modeling. It includes, firstly, the radiation theory of magnetic dipole in homogeneous medium; secondly, the analytical derivation of the complex image theory, which contains two general cases. One is when the tool is place in the relative high resistive layer. The other is when the tool is placed in the relative high conductive layer.

Chapter 3 presents data verification of the forward model. The analytical full solution results are compared with the simulation results. It is shown that our proposed method has a high accuracy. The tolerance, computation speed, possibility of real application and sensitivity are discussed as well.

Chapter 4 discusses the inversion method. A bisection method is used to inverse the boundary distance. The inversion method is tested on a two-layer model. The results show that our method is of great precision.

Finally, conclusion is given in Chapter 5.

Appendix I is a user's guide of the forward modeling code IMAG12, which uses the proposed complex image method. Input and output file format are explained. Simulation examples are given in two-layer and three-layer formations.

1.5 Main Contributions of the Dissertation

1. Extend the complex image theory to the relative high conductive side;

2. Investigate the performance of the complex image theory in different frequencies, spacing and different conductivity contrast formations;

3. Develop the simulation code to the high deviated well;

4. Investigate the component depth sensitivity. Explore inversion method based on the amplitude of the cross component;

5. Discuss the effect of noise in inversion process. Investigate the reliability of the inversion process.

Chapter 2 Theory of Forward Modeling

2.1 Magnetic Dipoles in Homogeneous Medium

As a start, we consider homogeneous isotropic medium. Assuming the harmonic time dependence to be $e^{j\omega}$, Maxwell's equations for the electric and magnetic fields are

$$\nabla \times \mathbf{H}(r) = j\omega\varepsilon\mathbf{E}(r) \text{ and} \tag{5a}$$

$$\nabla \times \mathbf{E}(r) = -j\omega\varepsilon\mathbf{H}(r) - j\omega\mu\mathbf{M}_s(r), \tag{5b}$$

where $\mathbf{M}_s$ is the moment of the magnetic dipole. $\varepsilon = \varepsilon^{'} - j\dfrac{\sigma}{\omega}$ is the complex dielectric permittivity. $\varepsilon^{'}$ is the dielectric permittivity and σ is the conductivity of the medium.

In order to solve equation (5), we introduce the Hertz vector potential $\mathbf{\Pi}$

$$\mathbf{E} = -j\omega\mu\nabla \times \mathbf{\Pi} \text{ and} \tag{6a}$$

$$\mathbf{H} = \nabla \times \nabla \times \mathbf{\Pi} - \mathbf{M}_s. \tag{6b}$$

Substituting equation (6) into (5), we can obtain the equation for the Hertz potential

$$\nabla^2\mathbf{\Pi} + k^2\mathbf{\Pi} = -\mathbf{M}_s\delta(r), \tag{7}$$

where $k^2 = \omega^2\mu\varepsilon$. Solving equation (7), we can obtain the Hertz potential. The electric and magnetic field in homogeneous medium can then be obtained from equation (6). For a z-directed magnetic dipole $\mathbf{M} = (0, 0, M_z)^T$, the hertz potential is given by

$$\Pi = \frac{M_z e^{-jkr}}{4\pi r}\hat{z}. \tag{8}$$

For an x-directed magnetic dipole $\mathbf{M} = (M_x, 0, 0)^T$, the hertz potential is given by

$$\Pi = \frac{M_x e^{-jkr}}{4\pi r}\hat{x}. \tag{9}$$

And for a y-directed magnetic dipole $\mathbf{M} = \left(0, M_y, 0\right)^T$, the hertz potential is given by

$$\Pi = \frac{M_y e^{-jkr}}{4\pi r}\hat{y}. \tag{10}$$

Substituting equations (8-10) into equation (6b), we can obtain the magnetic field generated by a magnetic dipole $\mathbf{M} = \left(M_x, M_y, M_z\right)\delta\left(r\right)$ in a homogeneous isotropic medium

$$H_{xx} = \frac{e^{-jkr}}{4\pi}\left[\frac{k^2}{r} - \frac{jk}{r^2} - \frac{k^2x^2+1}{r^3} + \frac{3jkx^2}{r^4} + \frac{3x^2}{r^5}\right], \tag{11}$$

$$H_{yy} = \frac{e^{-jkr}}{4\pi}\left[\frac{k^2}{r} - \frac{jk}{r^2} - \frac{k^2y^2+1}{r^3} + \frac{3jky^2}{r^4} + \frac{3y^2}{r^5}\right], \tag{12}$$

$$H_{zz} = \frac{e^{-jkr}}{4\pi}\left[\frac{k^2}{r} - \frac{jk}{r^2} - \frac{k^2z^2+1}{r^3} + \frac{3jkz^2}{r^4} + \frac{3z^2}{r^5}\right], \tag{13}$$

$$H_{yx} = H_{xy} = -\frac{xye^{-jkr}}{4\pi}\left[\frac{k^2}{r^3} - \frac{3jk}{r^4} - \frac{3}{r^5}\right], \tag{14}$$

$$H_{zx} = H_{xz} = -\frac{xze^{-jkr}}{4\pi}\left[\frac{k^2}{r^3} - \frac{3jk}{r^4} - \frac{3}{r^5}\right] \text{ and} \tag{15}$$

$$H_{zy} = H_{yz} = -\frac{yze^{-jkr}}{4\pi}\left[\frac{k^2}{r^3} - \frac{3jk}{r^4} - \frac{3}{r^5}\right]. \tag{16}$$

2.2 Review of Traditional Image Theory

Generally, image theory is to convert an inhomogeneous problem to a homogeneous one by introducing an image source. Then the homogeneous space green function could be used to solve the field distribution, which is much easier and faster than the full solution.

The conventional image theory is referring to one electrical dipole over the PEC interface, shown in Figure 2.1. There is no field in the lower half space. The field of upper half space can be calculated by replacing the interface by introducing an image source at lower space and applying the homogeneous green function. The field in upper space will be the summation of the fields generated by both sources. The two-layer inhomogeneous problem is then converted into a homogeneous problem.

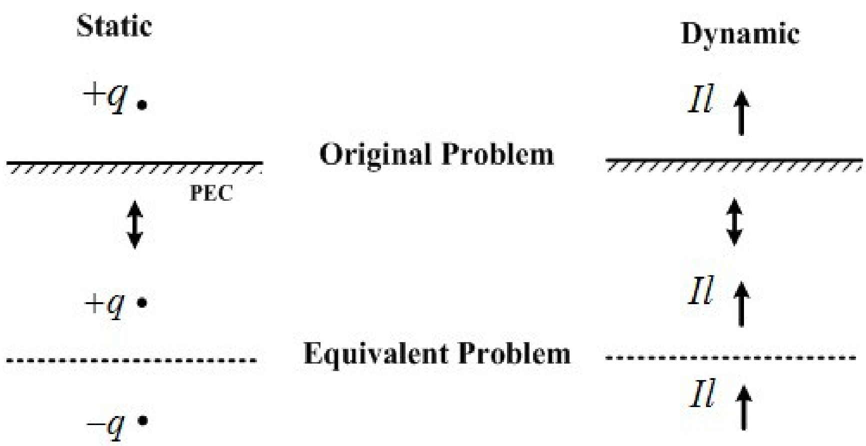

Figure 2.1 Image theory of PEC interface

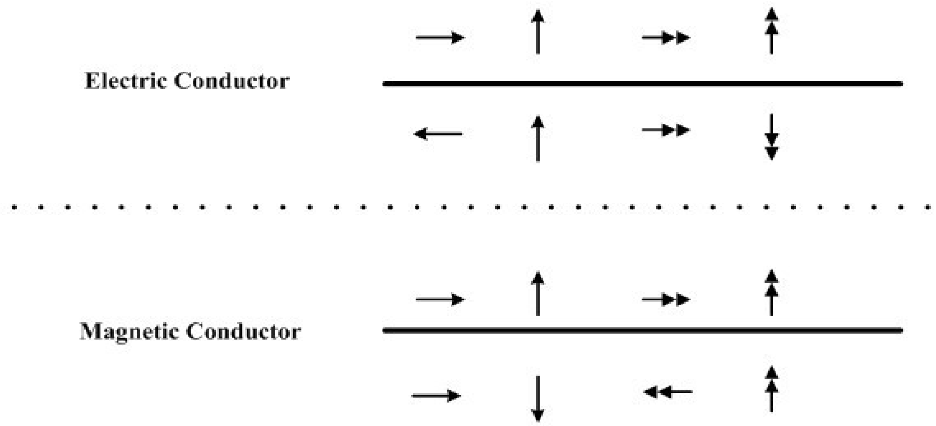

Figure 2.2 Summary of image theory

More generally, the image sources of electrical dipoles (represented by single arrows) and magnetic dipoles (represented by double arrows) over PEC and PMC respectively are shown in Figure 2.2. Over the electric conductor, the image sources of the horizontal electrical dipole and vertical magnetic dipole have the opposite direction from the original sources. This agrees with the fact that the tangential current does not radiate along the PEC plane. Similarly, when the vertical electrical dipole and horizontal magnetic dipole are over the magnetic conductor, there is no field radiation either.

2.3 Complex Image Theory in Non-perfect Medium

For deriving the complex image theory used into the application of geo-steering, the transmitter of the directional resistivity logging tool is exacted to a horizontally placed magnetic dipole source. This assumption is consistent with the real implement of the transmitter antenna, which is a coil antenna around the tool body.

2.3.1 Horizontal Dipole in Half Space

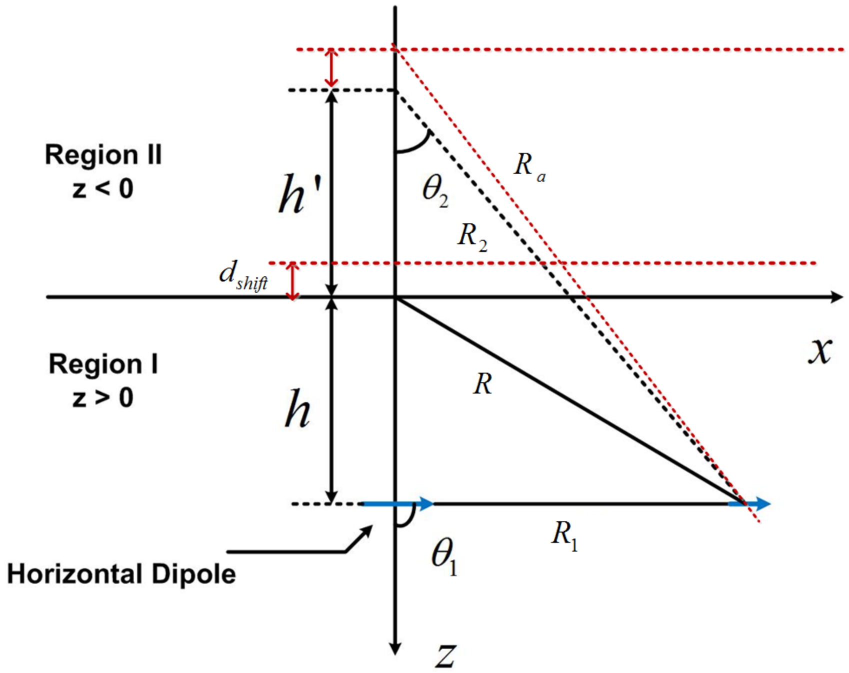

Figure 2.3 A horizontal dipole placed in half space model

Let a horizontal electrical dipole of moment p be placed at (0, 0, h) pointing at positive x axis as shown in Figure 2.3. It has been derived that the Hertz potential functions in this two regions satisfying the following two equations respectively,

$$\nabla^2 \mathbf{\Pi}_1 + \gamma_1^2 \mathbf{\Pi}_1 = \mathbf{p}\delta(x)\delta(y)\delta(z-h), \quad z \geq 0 \qquad \text{and} \tag{17a}$$

$$\nabla^2 \mathbf{\Pi}_2 + \gamma_2^2 \mathbf{\Pi}_2 = 0, \qquad z \leq 0, \tag{17b}$$

where $\gamma_1^2 = \omega^2 \mu_0 (\varepsilon_1 - j\sigma_1/\omega)$ and $\gamma_2^2 = \omega^2 \mu_0 (\varepsilon_2 - j\sigma_2/\omega)$.

The Hertz potential in Region I could be decomposed into two directions

$$\mathbf{\Pi}_1 = x'\Pi_{1x} + z'\Pi_{1z}. \tag{18}$$

2.3.2 Dipole in Lossless Half Space

If the dipole is within the air and above a conductive media, as shown in Figure 2.3, $\gamma_1{}^2 = \gamma_0{}^2 = \omega^2\mu_0\varepsilon_0$ and $\gamma_2{}^2 = \gamma^2 = \omega^2\mu_0\left(\varepsilon - j\,\sigma/\omega\right)$. The Hertz potential expressions for HMD are [12],

$$\Pi_{1x} = \frac{p}{4\pi}\left[\frac{e^{-\gamma_0 R_1}}{R_1} + \int_0^\infty \frac{u_0 - u}{u_0 + u} J_0\left(\lambda\rho\right) e^{-u_0(z+h)} \frac{\lambda}{u_0} d\lambda\right] \text{ and} \tag{19a}$$

$$\Pi_{1z} = \frac{p}{2\pi}\left[\int_0^\infty \frac{\left(u - u_0\right) e^{-u_0(z+h)}}{\left(\gamma_0^2 u + \gamma^2 u_0\right)} J_1\left(\lambda\rho\right)\lambda^2 d\lambda\right]\cos\phi, \tag{19b}$$

where

$R_1 = \left[\rho^2 + \left(z-h\right)^2\right]^{1/2}$,
$u_0 = \left(\lambda^2 - \gamma_0^2\right)^{1/2}$ and
$u = \left(\lambda^2 - \gamma^2\right)^{1/2}$.

For the application in well-logging, most cases are low frequency and satisfy the quasi-static condition, where we can assume $u_0 \approx \lambda$, then

$$P_m = \int_0^\infty \frac{u_0 - u}{u_0 + u} J_0\left(\lambda\rho\right) e^{-u_0(z+h)} \frac{\lambda}{u_0} d\lambda \approx -\int_0^\infty \frac{u - \lambda}{u + \lambda} J_0\left(\lambda\rho\right) e^{-\lambda(z+h)} d\lambda. \tag{20}$$

The Taylor-series expansion of the function f (λ) can be written in the form

$$f\left(\lambda\right) = e^{\lambda d_{shift}} \frac{u - \lambda}{u + \lambda} = \sum_{n=0}^{\infty} a_n \lambda^n, \tag{21}$$

where $d_{shift} = \left(1 - j\right)\delta$ and $a_n = \left(1/n!\right) f^{(n)}\left(0\right)$.

Approximate using only the first term and consequently,

$$\Pi_{1x} \approx \frac{p}{4\pi}\left(\frac{1}{R_1}-\frac{1}{R_a}\right) \text{ and} \tag{22}$$

$$\Pi_{1z} \approx \frac{p\cos\phi}{4\pi\rho}\left[\frac{\left(d_{shift}+z+h\right)}{R_a}-\frac{\left(z+h\right)}{R_2}\right], \tag{23}$$

where $R_a = \left[\rho^2 + \left(z+h+d_{shift}\right)^2\right]^{1/2}$ and $R_2 = \left[\rho^2 + \left(z+h\right)^2\right]^{1/2}$. Because the boundary shift d_{shift} is very small. The difference between R_a and R_2 is almost zero, which means

$$\frac{(d_{shift}t+z+h)}{R_a}-\frac{\left(z+h\right)}{R_2} \approx 0. \tag{24}$$

Then, with the assumption of quasi-static, the Hertz potential of the horizontal dipole placed in a two-layer half space media can be simplified to one component

$$\Pi_{1x} \approx \frac{p}{4\pi}\left(\frac{1}{R_1}-\frac{1}{R_a}\right) \text{ and} \tag{25}$$

$$\Pi_{1z} \approx 0. \tag{26}$$

Therefore, the Sommerfeld integral is simplified to a summation of two terms. Both are in x direction and located at $z=h$ and $z=-\left(h+d_{shift}\right)$, respectively. The total field is the superposition of the fields radiated by the two discrete sources in the homogeneous medium.

We can extend this case when the boundary is not perfect conductive and the source region is within the relative low conductive media. The non-perfect conductive boundary can be approximated as a perfect conductive boundary by introducing a complex depth shift d_{shift}. By shifting the boundary, the conventional image theory could be applied.

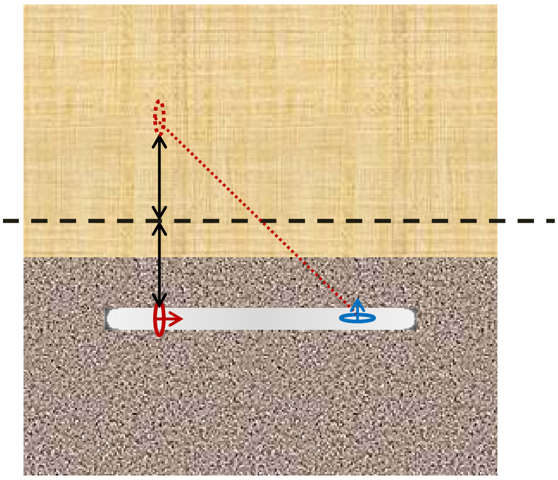

Figure 2.4 Two-layer equivalent model by applying the image theory

The equivalent two-layer model is shown in Figure 2.4, in which the remote bed (upper layer, where the image source is located) is much more conductive than the near bed (lower layer, where the original source is located). Bannister gave the shifts for horizontal and vertical magnetic dipoles respectively. They are

$$d_{VMD\_shift} = \frac{1}{\sqrt{k_b^2 - k_n^2}} \quad \text{and} \quad d_{HMD\_shift} = \frac{\sqrt{k_b^2 - k_n^2}}{-k_n^2}, \tag{27}$$

where $k_b^2 = \omega^2 \mu \varepsilon_b - j\omega\mu\sigma_b$ and $k_n^2 = \omega^2 \mu \varepsilon_n - j\omega\mu\sigma_n$ are the wave numbers of near bed and the remote bed. If we further assume that the remote bed is sufficiently more conductive than the near bed [9]. Then the shift distance can be simplified to

$$d_{VMD\_shift} = d_{HMD\_shift} \approx \frac{1}{jk_n}. \tag{28}$$

For the logging tool with spacing L, the H field received by the receiver is

$$H_{xz} = \frac{P}{4\pi} \frac{e^{-jk_b r}}{r^3} \left(k_b{}^2 r^2 - 3jk_b r - 3\right) \frac{\left(2d_{shift} + 2h\right)L}{r} \quad \text{and} \tag{29a}$$

$$H_{xx} = \frac{P}{4\pi}\left[\frac{e^{-jk_b r}}{r^3}\left(k_b^2 r^2 - 3jk_b r - 3\right)\left(\frac{2d_{shift} + 2h}{r}\right)^2 + \frac{2e^{-jk_b r}}{r^3}\left(jk_b r + 1\right)\right] + \frac{P}{4\pi}\frac{e^{-jk_b L}}{L^3}\left(jk_b L + 1\right). \tag{25b}$$

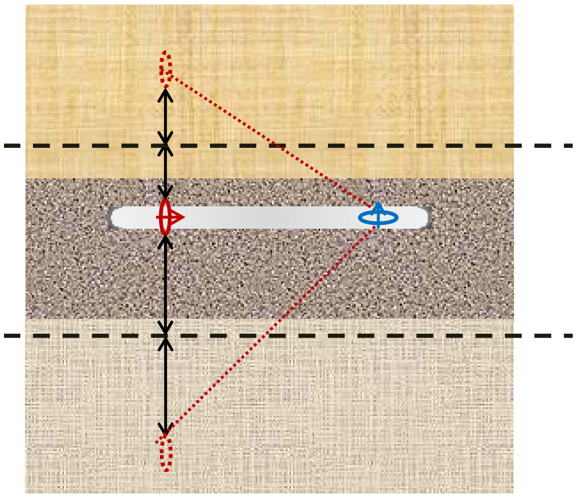

Figure 2.5 Three-layer equivalent model by applying the image theory

Consider a three-layer model as shown in Figure 2.5. In this model, for each boundary, only the first image is considered. According to the application condition of the approximated image theory, the middle layer, where the drilling bit is in, has the higher resistivity compared with the other two adjacent layers. Then the three-layer model is simplified into a homogeneous model with three sources.

2.3.3 Dipole in the Dissipative Media

Consider another case when region I is dissipative, while that region II is non-conductive. The parameters of those two regions are $\gamma_1^2 = \gamma^2 = \omega^2 \mu_0 \left(\varepsilon - j\sigma/\omega\right)$, $\gamma_2^2 = \gamma_0^2 = \omega^2 \mu_0 \varepsilon_0$. Then, the Hertz potential in the two regions become

$$\Pi_{1x} = \frac{p}{4\pi}\left[\frac{e^{-\gamma R_1}}{R_1} + \int_0^\infty \frac{u-u_0}{u+u_0} J_0\left(\lambda\rho\right) e^{-u(z+h)} \frac{\lambda}{u} d\lambda\right] \text{ and} \tag{30a}$$

$$\Pi_{1z} = \frac{p}{2\pi}\left[\int_0^\infty \frac{\left(u_0 - u\right) e^{-u(z+h)}}{\left(\gamma_0^2 u + \gamma^2 u_0\right)} J_1\left(\lambda\rho\right) \lambda^2 d\lambda\right] \cos\phi, \tag{26b}$$

where

$R_0 = \left[\rho^2 + \left(z-h\right)^2\right]^{1/2}$,

$u_0 = \left(\lambda^2 - \gamma_0^2\right)^{1/2}$ and

$u = \left(\lambda^2 - \gamma^2\right)^{1/2}$.

Define $n = \left(\varepsilon_r - j\,\sigma/\omega\varepsilon_0\right)^{1/2}$, $\gamma = n\gamma_o$ and apply Sommerfeld identity (31) in (29),

$$\frac{e^{-\gamma_1 R_2}}{R_2} = \int_0^\infty \frac{J_0\left(\lambda\rho\right)}{u} e^{-u|z+h|} \lambda d\lambda. \tag{31}$$

The Hertz potential can be rewritten as

$$\Pi_{1x} = \frac{p}{4\pi}\left[\frac{e^{-\gamma R_1}}{R_1} - \frac{e^{-\gamma R_2}}{R_2} + 2\int_0^\infty \frac{J_0\left(\lambda\rho\right) e^{\left[-u(z+h)\right]}}{u+u_0} \lambda d\lambda\right] \text{ and} \tag{32a}$$

$$\Pi_{1z} = -\frac{p}{2\pi}\left(1-n^2\right)\left[\int_0^\infty \frac{J_1\left(\lambda\rho\right) e^{-u(z+h)}}{\left(u+u_0\right)\left(n^2 u_0 + u\right)} \lambda^2 d\lambda\right] \cos\phi, \tag{29b}$$

where $R_1 = \left[\rho^2 + \left(z-h\right)^2\right]^{1/2}$ and $R_2 = \left[\rho^2 + \left(z+h\right)^2\right]^{1/2}$. To simply these expressions, by using Lien's method [13], define the abbreviations,

$G_1 = \dfrac{e^{-\gamma R_1}}{R_1}$, $\quad G_2 = \dfrac{e^{-\gamma R_2}}{R_2}$,

$U = 2\displaystyle\int_0^\infty \frac{J_1\left(\lambda\rho\right) e^{\left[-u(z+h)\right]}}{u+u_0} \lambda d\lambda$ and

$$W = -2\left(1-n^2\right)\left[\int_0^\infty \frac{J_1(\lambda\rho)e^{-u(z+h)}}{(u+u_0)\left(n^2u_0+u\right)}\lambda^2 d\lambda\right]$$
$$= 2\left(1-n^2\right)\frac{\partial}{\partial x}\int_0^\infty \frac{J_0(\lambda\rho)e^{-u(z+h)}}{(u+u_0)\left(n^2u_0+u\right)}\lambda d\lambda.$$

The Hertz potential function $\mathbf{\Pi}_1$ is then given by

$$\mathbf{\Pi}_1 = \frac{p}{4\pi}\left(G_1 - G_2 + U\right)x' + Wz'. \tag{33}$$

The field components in Region I can be found by following Norton method in cylindrical coordinates

$$\frac{\partial W}{\partial z} = -2\frac{\partial}{\partial x}\int_0^\infty \left(\frac{1}{u_0+u} - \frac{n^2}{n^2u_0+u}\right)J_0(\lambda\rho)e^{-u(z+h)}\lambda d\lambda. \tag{34}$$

Define $V = 2n^2\int_0^\infty \frac{J_0(\lambda\rho)e^{-u(z+h)}}{n^2u_0+u}\lambda d\lambda$, then

$$\frac{\partial W}{\partial z} = -\frac{\partial U}{\partial x} + \frac{\partial V}{\partial x}. \tag{35}$$

The divergence of $\mathbf{\Pi}_1$, therefore, is given by

$$\nabla \bullet \mathbf{\Pi}_1 = \frac{\partial}{\partial x}\left(G_1 - G_2 + V\right). \tag{36}$$

Because $H_1 = \nabla\left(\nabla \bullet \mathbf{\Pi}_1\right) + \gamma^2\mathbf{\Pi}_1$, the z component is

$$H_{1z} = \gamma^2 W + \frac{\partial^2}{\partial x \partial z}\left(G_1 - G_2 + V\right). \tag{37}$$

Transfer the solution into cylindrical coordinates and apply the Sommerfeld's integral representation of spherical wave function, equation (31), the integral in equation (34) becomes

$$-2\frac{\partial}{\partial x}\int_0^\infty \left(1 - \frac{u}{n^2u_0+u}\right)J_0(\lambda\rho)e^{-u(z+h)}\lambda d\lambda = 2\frac{\partial^2 G_2}{\partial z \partial \rho} - \frac{1}{n^2}\frac{\partial^2 V}{\partial z \partial \rho}. \tag{38}$$

Furthermore, in the low frequency assumption, using the leading term of the asymptotic expression of the Bessel function, the approximate expression of *V* is given [11]

$$H_{1z} = \frac{\partial^2}{\partial z \partial \rho}\left(G_1 + G_2 - \frac{V}{n^2}\right)\cos\phi. \tag{39}$$

Form equation (39), the cross *z* component is generated by original source G_1, image source G_2 and a correction term related to *V*. Roy Harold Lien gave the low frequency approximation of the integral *V* under the assumption that $\left|n^2\right| \gg 1$ and $\left|jnkR_2/2\right| \gg 1$, the leading term approximation is given as

$$V = 2k_0\rho^{-1}e^{-j\gamma(z+h)} \text{ and} \tag{40}$$

$$H_{1z} = \frac{\partial^2}{\partial z \partial \rho}\left(G_1 + G_2\right)\cos\phi - \frac{2k_0}{n^2\rho^2}\gamma e^{-j\gamma(z+h)}\cos\phi. \tag{41}$$

Considering the tool is always located in *xz* plane and parallel with *x* axis, $\phi = 0^o$, we will have

$$H_{1z} = \frac{\partial^2}{\partial z \partial \rho}\left(G_1 + G_2\right) + H_c \text{ and} \tag{42}$$

$$H_c = -\frac{2k_0}{n^2\rho^2}\gamma e^{-jr(z+h)}. \tag{43}$$

The final expressions for the magnetic field in Region I, for the case $\sigma/\omega\varepsilon \gg 1$, is generated by the original source placed at $z = h$, an image place at $z = -h$ and a correction term expressed in equation (43).

Then, the H field received by the receiver in cylindrical coordinator is

$$
\begin{aligned}
H_{xz} = \frac{P}{4\pi}\Bigg\{ & \frac{1}{2}\left[-n^2k^2 + j3nkr_1^{-1} + 3r_1^{-2}\right]\sin 2\theta_1 G_1 \\
& + \frac{1}{2}\left[-n^2k^2 + j3nkr_2^{-1} + 3r_2^{2}\right]\sin 2\theta_2 G_2 - \frac{1}{n^2}\frac{\partial^2 V}{\partial z \partial \rho}\Bigg\} \text{ and}
\end{aligned}
\tag{44a}
$$

$$
\begin{aligned}
H_{xx} = \frac{P}{4\pi}\Big\{ & \left[n^2k^2\cos^2\theta_1 + jnk(2-3\cos^2\theta_1)r_1^{-1} + \left(2-3\cos^2\theta_1\right)r_1^{-2}\right]G_1 \\
& + \left[n^2k^2 - j3nkr_2^{-1} - 3r_2^{-2}\right]\cos^2\theta_2 G_2 - \frac{1}{\rho}\frac{\partial V}{\partial \rho}\Big\},
\end{aligned}
\tag{44b}
$$

where θ_1 and θ_2 are the angles shown in Figure 2.3.

.

Chapter 3 Simulation Results and Discussion

3.1 1D Formation Model

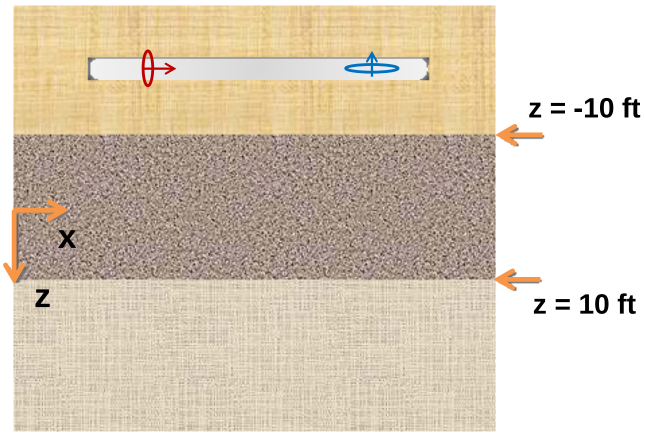

Figure 3.1 Three-layer model

If the borehole is neglected and only the depth variation is considered, an isotropic formation could be modeled as a layered medium, as shown in Figure 3.1. In this model, the *z* direction is the depth direction. In the application of geo-steering, the tool is always kept in the production layer, which means in most cases, the tool is placed horizontally. The testing points will be along the *z* direction. Then the received signal is a function of distance from the tool position to the boundary. According to the electrical properties of the near bed and remote bed, two cases are possible. One is when the tool is within the high resistive bed. The other is when the tool is in the high conductive bed. For these two cases, different approximations must be used to apply the complex image method. For each case, the simulation results generated by the complex image method will be presented together with the results obtained by a full solution code, which is named INDTRI developed by the Well Logging Lab at the University of Houston. The Hankel integral is solved by 283 points fast Hankel transform. The relative permittivity and permeability of each layer are set to be 1. That is because, firstly, the tool is working at relatively low frequency, the effect of permittivity is not significant. Secondly, in the most cases, the earth is nonmagnetic. We can always neglect the permeability of the earth.

3.2 Tool Configuration

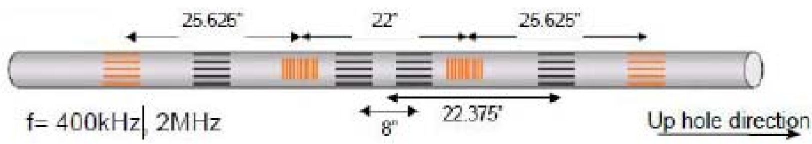

Figure 3.2 Azitrack tool configuration

Figure 3.2 shows the geo-steering tool made by Baker Hughes. This tool works at two frequencies, 2 MHz and 400 KHz. The configuration is symmetric, which is called a compensated LWD configuration. As shown in Figure 3.2, there are several different spacings. For convenience sake without losing generality, only two spacings are tested. The long spacing is 33.375 in. and the short spacing is 22.265 in.

In the following simulation, actually, we only consider the radiation of dipole source and neglect the effect of mandrel. The reason why we can use this assumption is that, firstly, compared with the geological size of the formation, the size of the mandrel can be neglected. Secondly, the effect of mandrel is to enhance or reduce the magnitude of the field, but not change the distribution. The third one is the effect of the mandrel can be compensated by the symmetrical configuration. So, in the following simulation, the tool with one transmitter and one receiver, but without mandrel, is simulated.

3.3 Simulation Results

3.3.1 R_1 = R_3 =1 Ohm.m, R_3 = 100 Ohm.m

Consider the three-layer model, as shown in Figure 3.1. The high resistivity layer is in the middle. The parameters of these three layers are $\varepsilon_{r1} = \varepsilon_{r3} = 1$, $\mu_{r1} = \mu_{r3} = 1$, and $\sigma_1 = \sigma_3 = 1$ for the upper and lower layer, $\varepsilon_{r2} = 1$, $\mu_{r2} = 1$, and $\sigma_2 = 0.01$ for the middle layer. The boundaries are at z = 10 ft. and z = -10 ft. This is the general case when the drilling bit is in the high resistivity layer.

a) Frequency = 2 MHz, spacing = 33.375 in.

Figure 3.3 shows simulation results of the cross component H_{zx}. The red circle indicates result calculated by approximated method and the blue dash line is the result of a full solution. From the results, we can see that the image method works pretty well. Even when the tool crosses the boundary, there is only small error between the approximation and full solution. Here, the results show that when the tool is working at 2 MHz, the long spacing channel works well. The cross component could represent the boundary information. Compared with the full solution results, there is no much error.

Figure 3.4 shows the phase shift and attenuation of the compensated propagation tool. These two parameters will be used in inversing the apparent resistivity of the formation. Compared with the full solution results, there is noticeable error when the logging tool is close to the boundary. Because our three-layer model is symmetrical, the simulation results are also symmetrical.

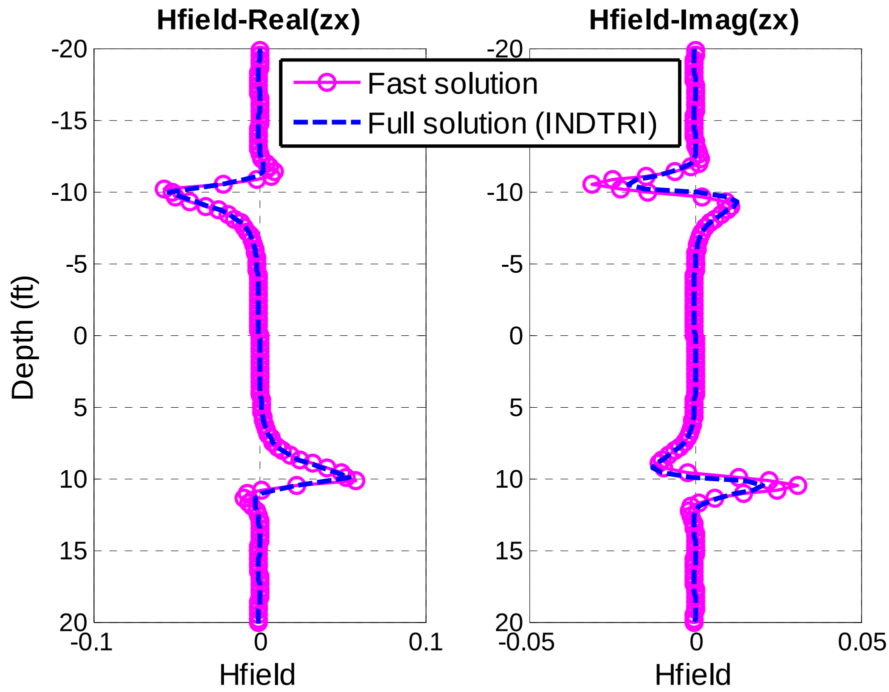

Figure 3.3 Tool response H_{zx} component ($\sigma_1 = \sigma_3 = 1, \sigma_2 = 0.01$, 2MHz, long)

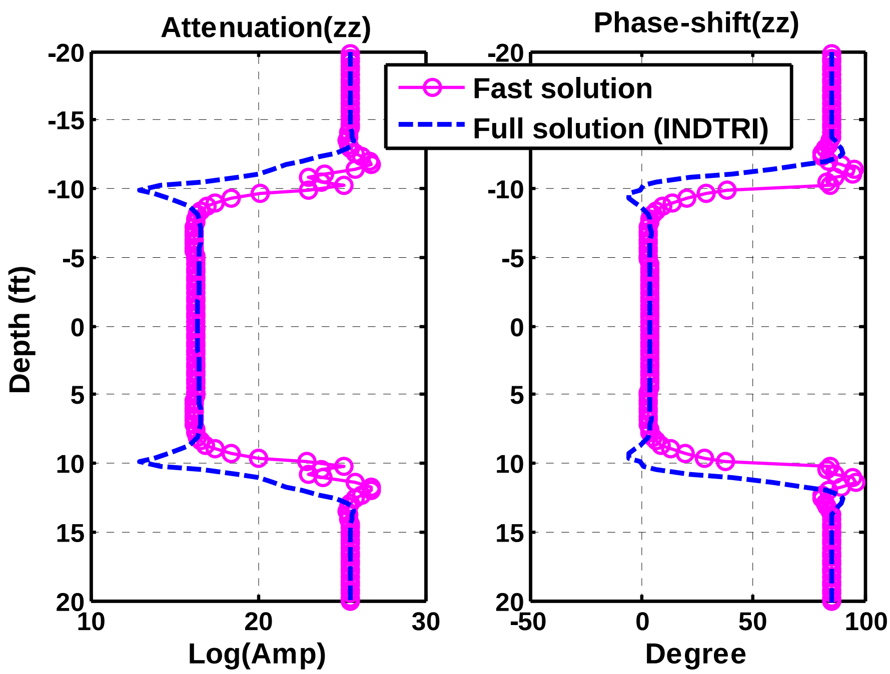

Figure 3.4 Phase difference and attenuation ($\sigma_1 = \sigma_3 = 1, \sigma_2 = 0.01$, 2 MHz, long)

b) Frequency = 2 MHz, spacing = 22.265 in.

Figure 3.5 and Figure 3.6 give the simulation results when the logging tool is working at 2 MHz and the spacing is short. Compared with the full solution results, the approximation method also works well. Only small error appears around boundary. Compared with the long spacing case, cross component H_{zx} has a little more error at the boundary. Phase shift and attenuation are a little bit better. Although in this case, the error of cross component is a little bit larger, it doesn't affect the boundary information.

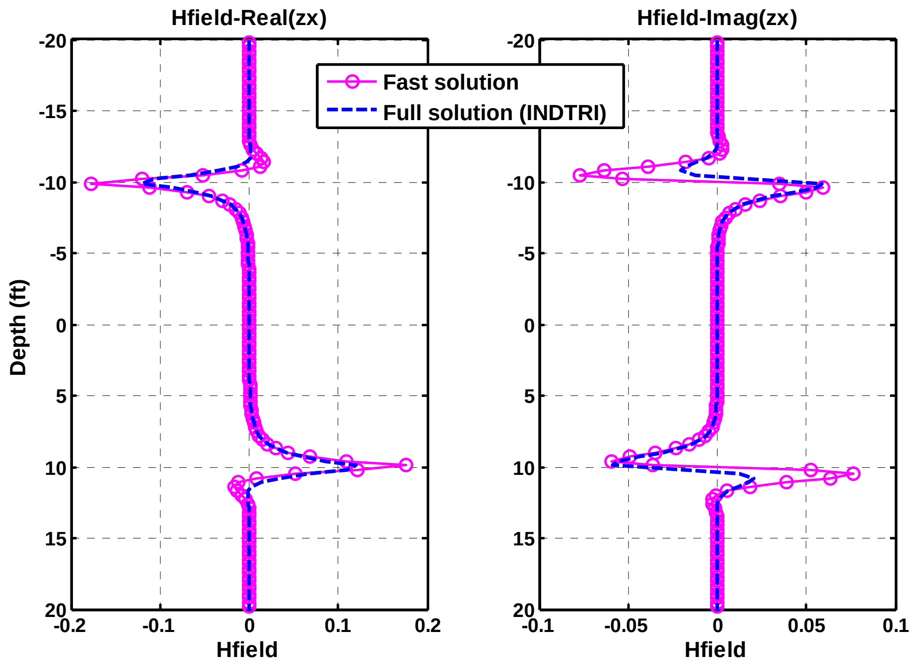

Figure 3.5 Tool response Hzx component ($\sigma_1 = \sigma_3 = 1, \sigma_2 = 0.01$, 2 MHz, short)

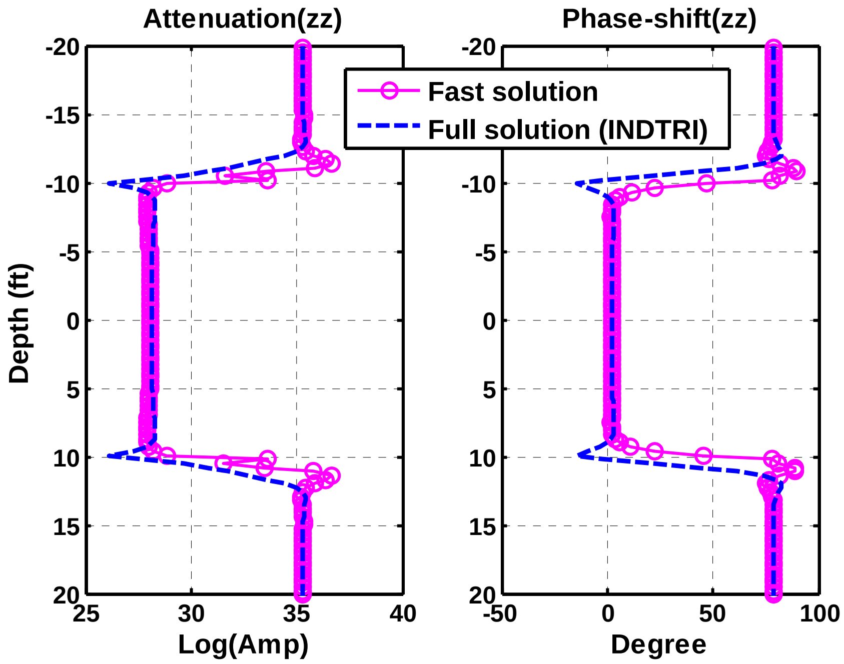

Figure 3.6 Phase difference and attenuation ($\sigma_1 = \sigma_3 = 1$, $\sigma_2 = 0.01$, 2 MHz, short)

c) Frequency = 400 KHz, spacing = 33.375 in.

When the tool is working at 400 KHz and the spacing is long, the simulation results are shown in Figure 3.7. The real part of the cross component H_{zx} still matches well with full solution results, even when the logging point is at the boundary. Image part of H_{zx} has a little bit more error. Based on this property, we consider that the boundary inversion could be developed only in term of the real part of H_{zx}.

Figure 3.8 shows the phase shift and attenuation of the logging tool, when it is working at 400 KHz and the spacing is long. The results shows that, in most range, the simulation results of the approximation method agree with the full solution results. Only exception is around the boundaries, where noticeable error is witnessed.

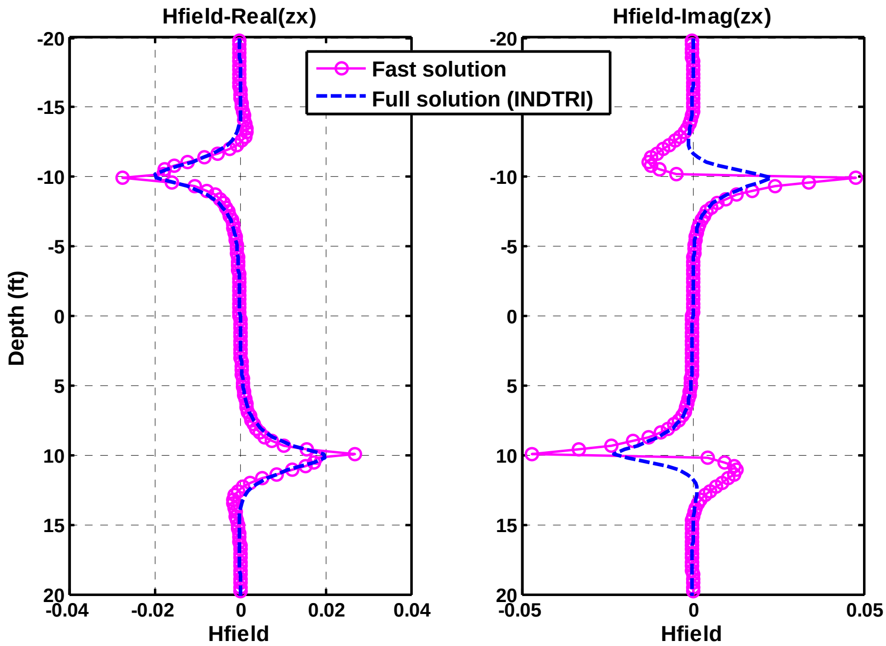

Figure 3.7 Tool response H_{zx} component ($\sigma_1 = \sigma_3 = 1, \sigma_2 = 0.01$, 400 KHz, long)

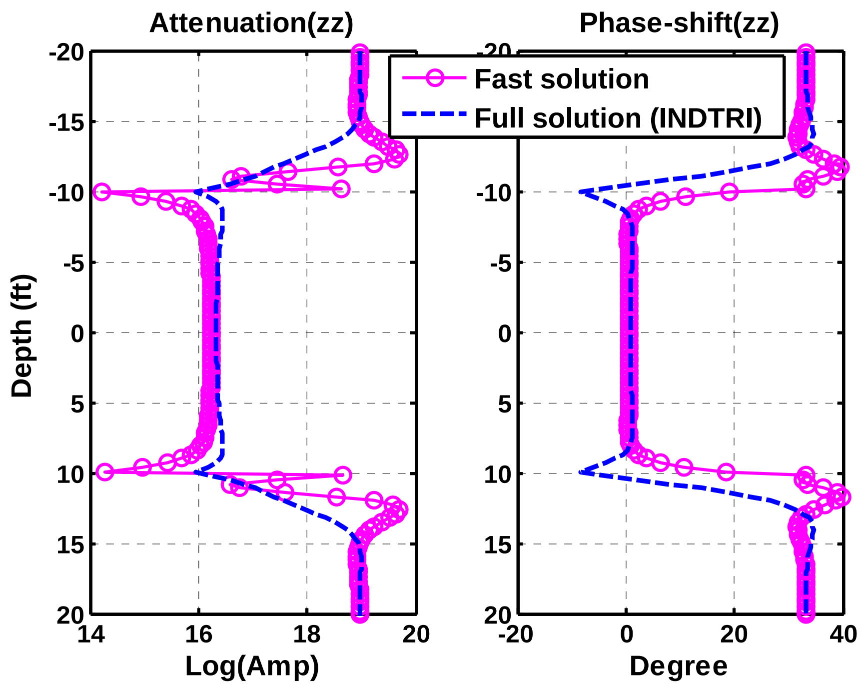

Figure 3.8 Phase difference and attenuation ($\sigma_1 = \sigma_3 = 1, \sigma_2 = 0.01$, 400 KHz, long)

a) Frequency = 400 KHz, spacing = 22.265 in.

When the tool is working at 400 KHz with short spacing, the cross component H_{zx} is not as good as before, as shown in Figure 3.9. Not only image part, but also real part of H_{zx} deviates from full solution around the boundaries. However, this error only exists within the area 2 in. away from the boundaries. For the application of geo-steering, this distance is relatively small. So, this error is acceptable.

Figure 3.10 shows the phase shift and attenuation when the tool is working at 400 KHz and with short spacing. Compared with other channels, the simulation results of the approximation method show enough agreement with the full solution results. Error only occurs near the boundaries. Based on the phase shift and attenuation, the apparent conductivities of the three layers could be inversed.

3.3.2 $R_1 = R_3 = 1$ Ohm.m, $R_3 = 10$ Ohm.m

Consider the three-layer model, as shown in Figure 3.1. The resistivity of the middle layer is reduced 10 times. The parameters of these three layers are $\varepsilon_{r1} = \varepsilon_{r3} = 1$, $\mu_{r1} = \mu_{r3} = 1$, and $\sigma_1 = \sigma_3 = 1$ for the upper and lower layer, $\varepsilon_{r2} = 1$, $\mu_{r2} = 1$, and $\sigma_2 = 0.1$ for the middle layer. The boundaries are at z = 10 ft. and z = -10 ft. This is also the general case when the drilling bit is in the high resistivity layer.

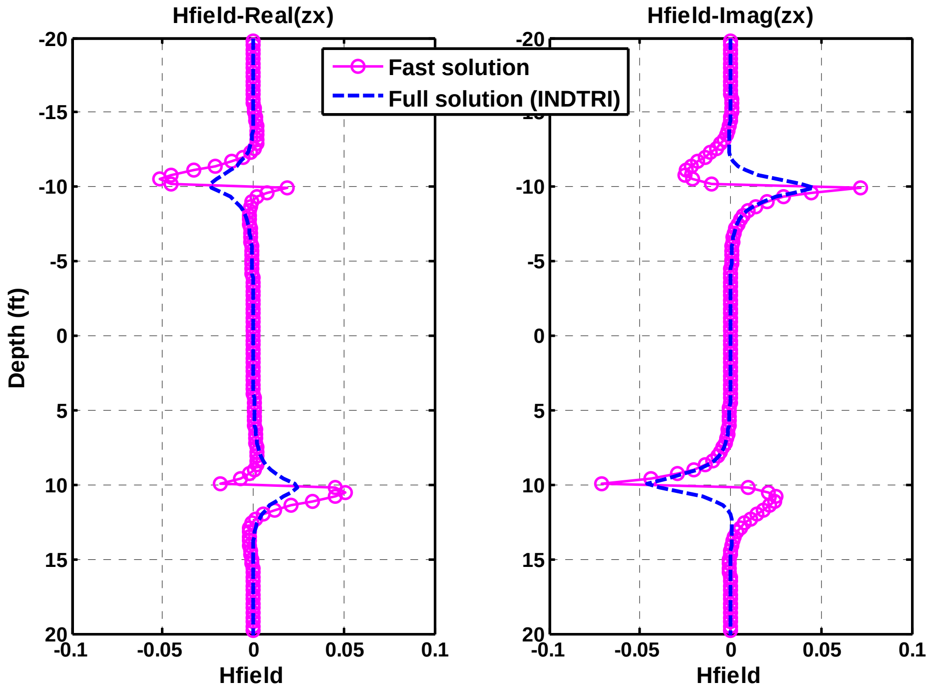

Figure 3.9 Tool response H_{zx} component ($\sigma_1 = \sigma_3 = 1$, $\sigma_2 = 0.01$, 400 KHz, short)

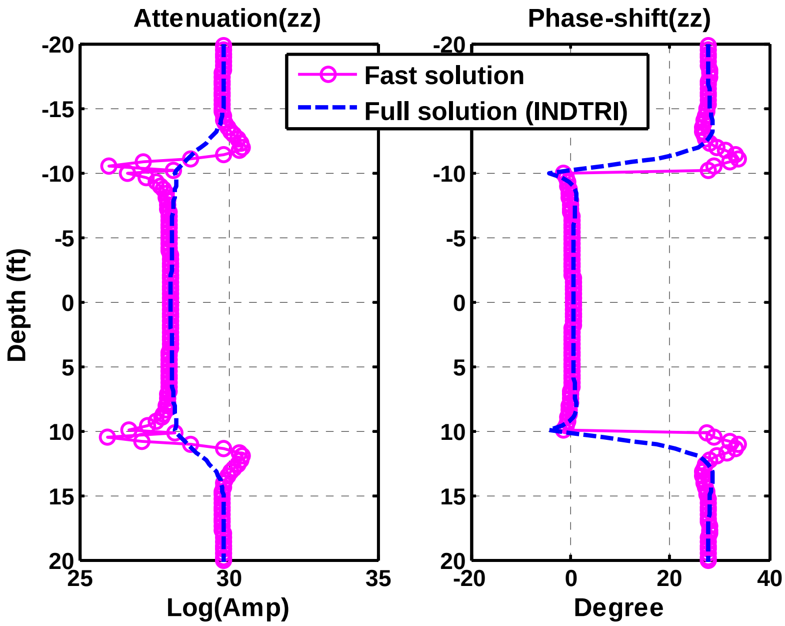

Figure 3.10 Phase difference and attenuation ($\sigma_1 = \sigma_3 = 1$, $\sigma_2 = 0.01$, 400 KHz, short)

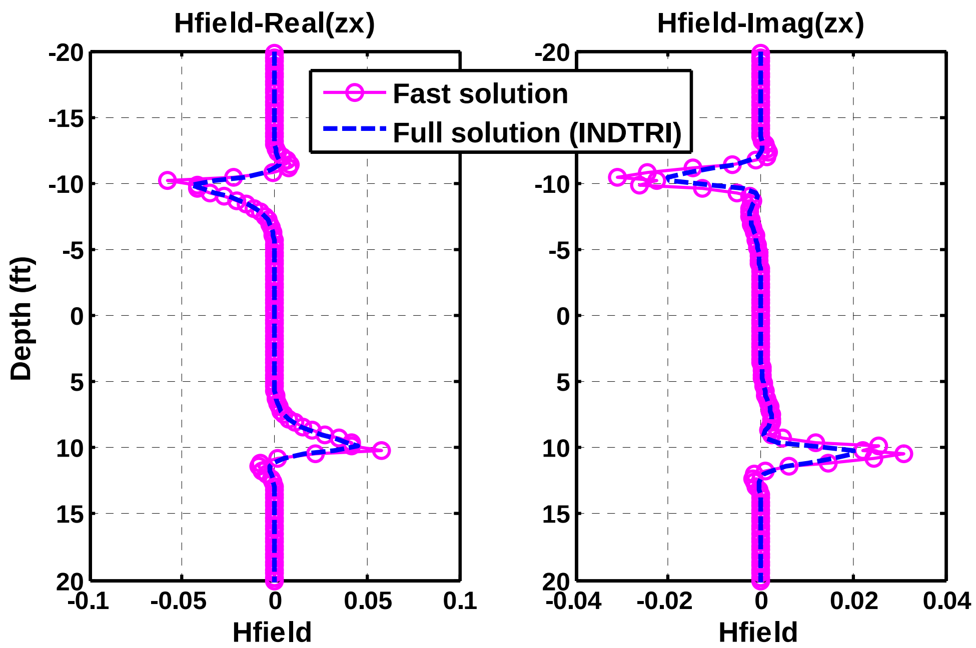

Figure 3.11 Tool response H_{zx} component ($\sigma_1 = \sigma_3 = 1$, $\sigma_2 = 0.1$, 2 MHz, long)

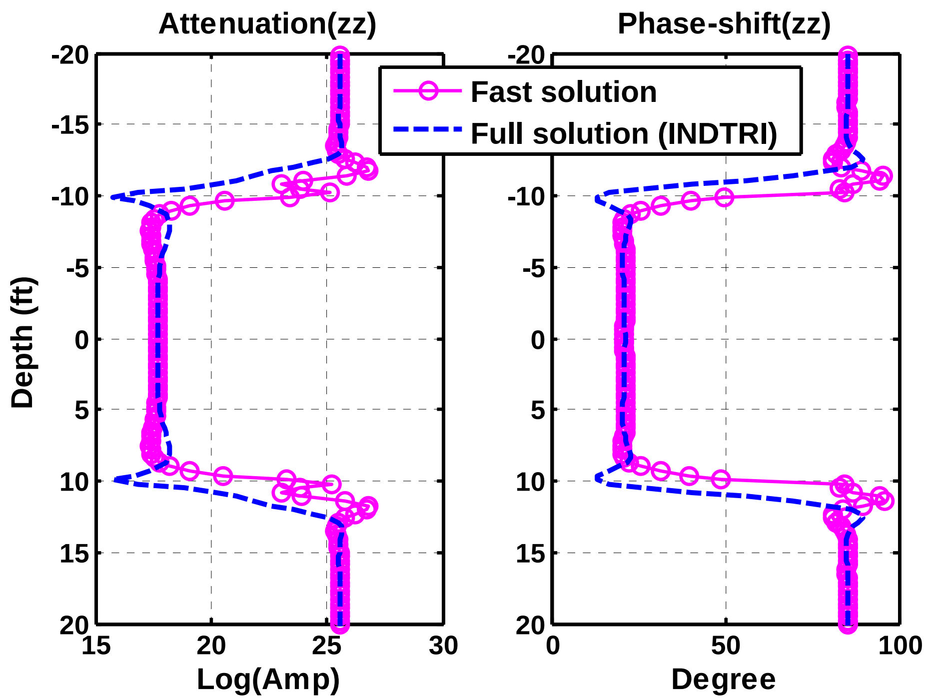

Figure 3.12 Phase difference and attenuation ($\sigma_1 = \sigma_3 = 1$, $\sigma_2 = 0.1$, 2 MHz, long)

a) Frequency = 2 MHz, spacing = 33.375 in.

Figure 3.11 gives the simulation results when the tool is working at relative high frequency and long spacing, where the middle layer of the formation is relatively less resistive. The figure shows that the cross component H_{zx} simulated by approximation method has a good agreement with the data given by full solution. This means this approximation method can be applied into the forward modeling of geo-steering tool and the simulation results are good enough to be used to extract boundary information.

b) Frequency = 2 MHz, spacing = 22.265 in.

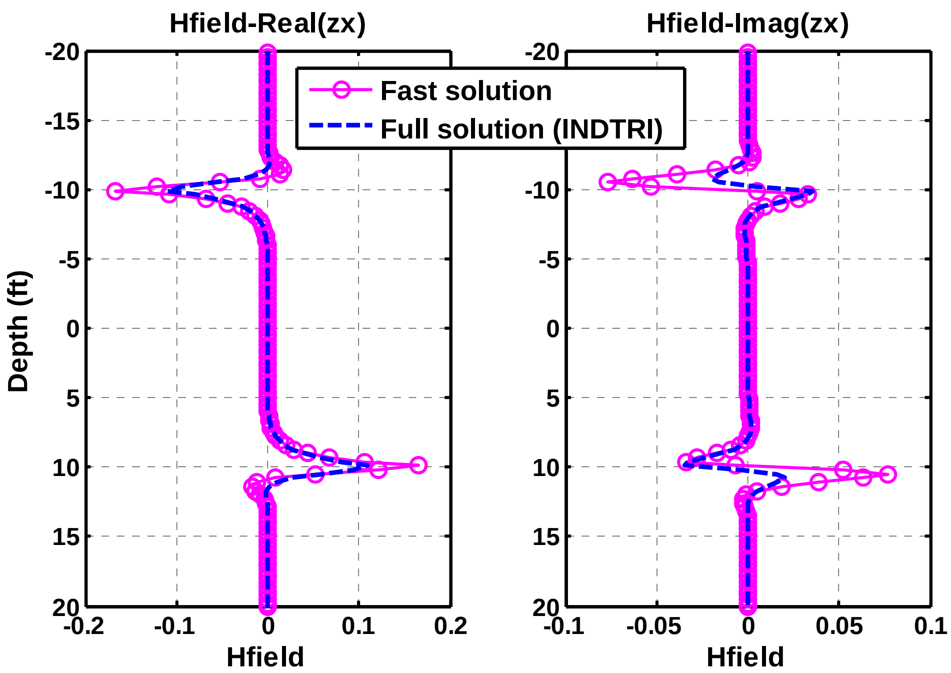

Figure 3.13 Tool response H_{zx} component ($\sigma_1 = \sigma_3 = 1, \sigma_2 = 0.1$, 2 MHz, short)

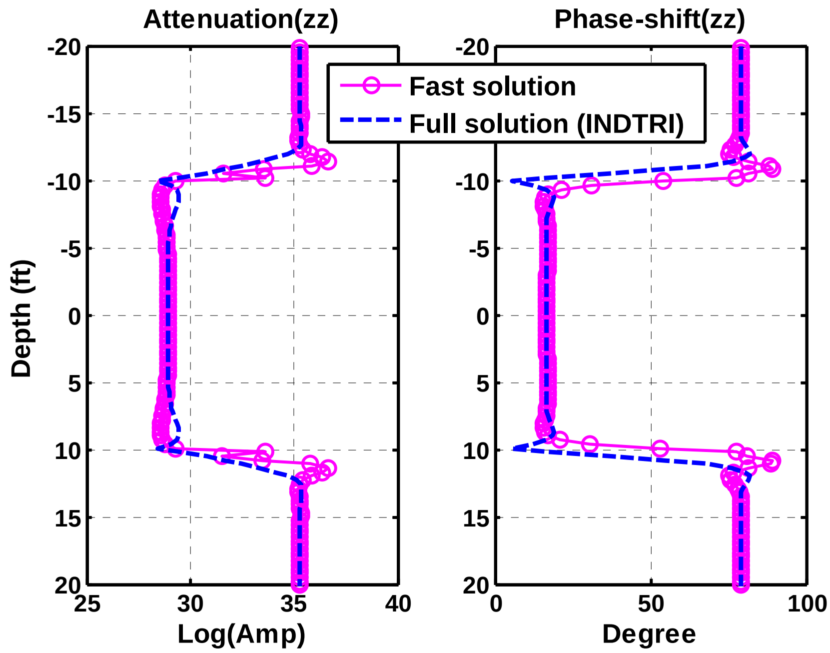

Figure 3.14 Phase difference and attenuation ($\sigma_1 = \sigma_3 = 1, \sigma_2 = 0.1$, 2 MHz, short)

c) Frequency = 400 KHz, spacing = 33.375 in.

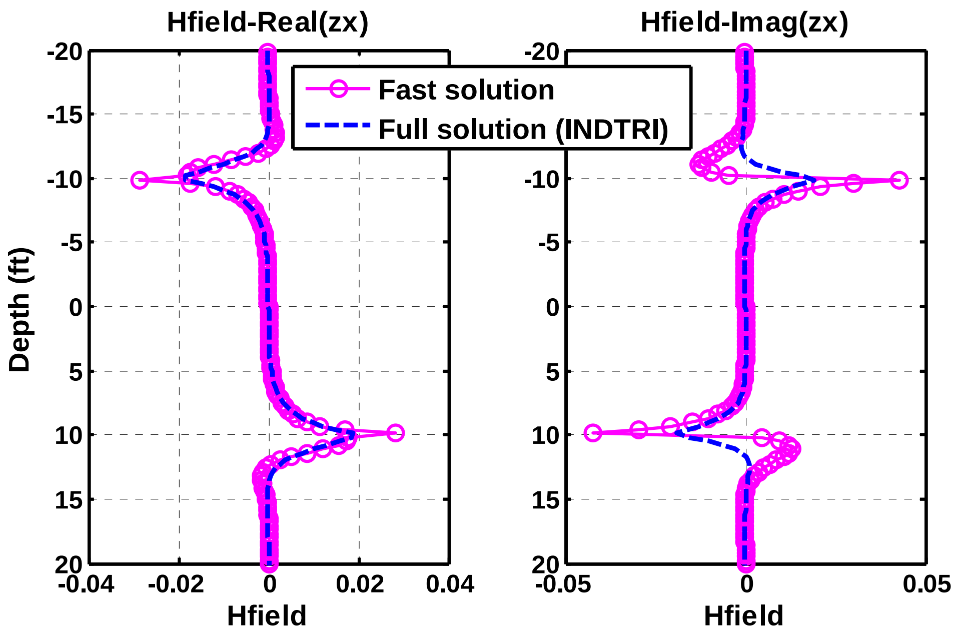

Figure 3.15 Tool response H_{zx} component ($\sigma_1 = \sigma_3 = 1, \sigma_2 = 0.1$, 400 KHz, long)

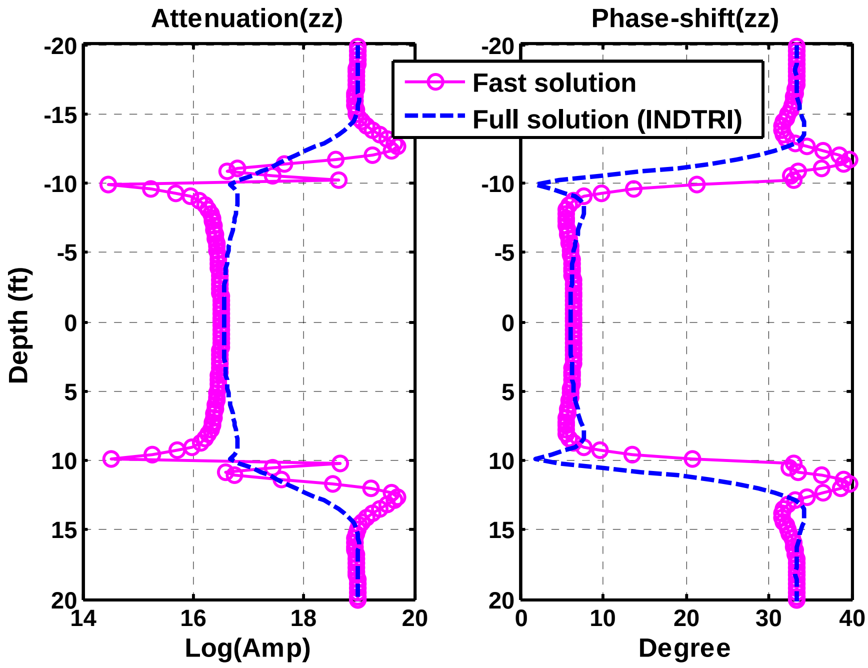

Figure 3.16 Phase difference and attenuation ($\sigma_1 = \sigma_3 = 1$, $\sigma_2 = 0.1$, 400 KHz, long)

d) Frequency = 400 KHz, spacing = 22.265 in.

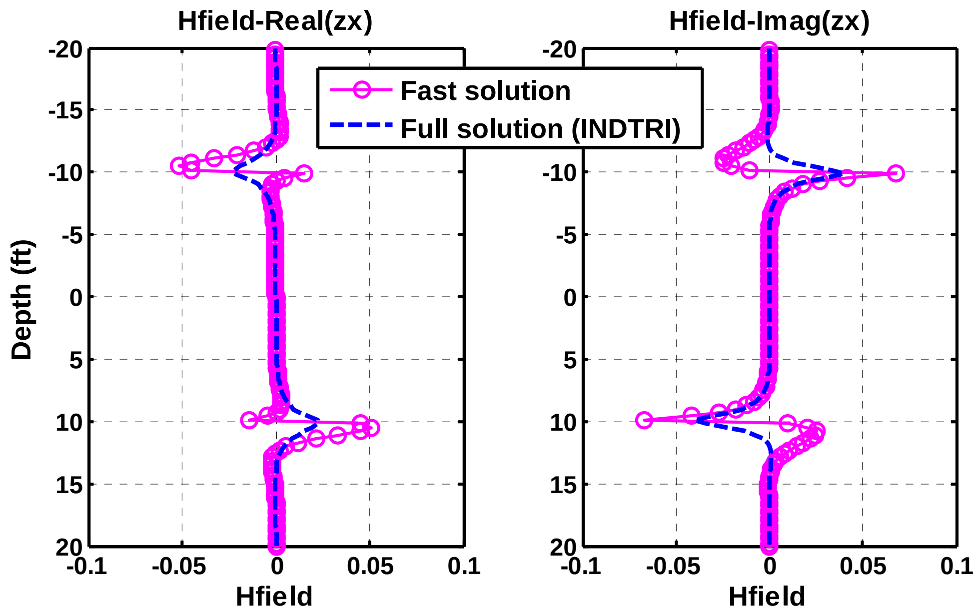

Figure 3.17 Tool response H_{zx} component ($\sigma_1 = \sigma_3 = 1$, $\sigma_2 = 0.1$, 400 KHz, short)

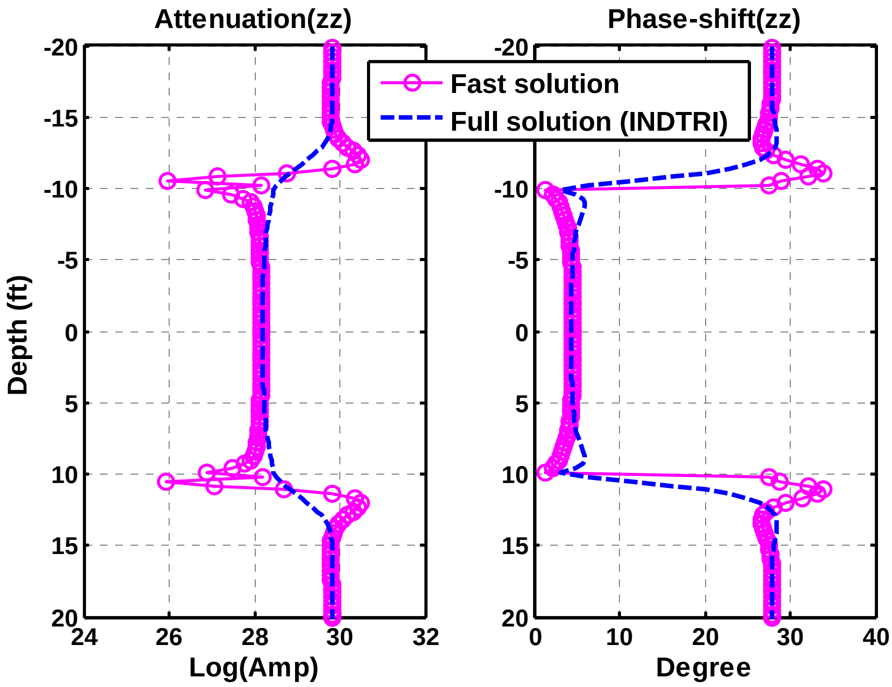

Figure 3.18 Phase difference and attenuation ($\sigma_1 = \sigma_3 = 1$, $\sigma_2 = 0.1$, 400 KHz, short)

Figure 3.13 to Figure 3.18 show the simulation results when the tool is working in other three channels. As in the first case, the approximation method works well in all other three channels, 2M with short spacing, 400 KHz with long spacing and 400 KHz with short spacing. Although when the frequency is lower, the error around boundaries becomes larger, however, the accuracy is still within an acceptable range. From the results of phase shift and attenuation, the apparent resistivity of each layer can be inverted. Based on the inverted resistivity and the cross component H_{zx} data, the boundary information can be extracted.

3.3.3 $R_1 = R_3$ =100 Ohm.m, R_2 = 1 Ohm.m

In this case, the formation model is also three-layer. The difference between this and previous two cases is that, in this case, the middle layer is of high conductive and two remote layers are of relatively high resistive. In this case, the parameters of these three layers are $\varepsilon_{r1} = \varepsilon_{r3} = 1$, $\mu_{r1} = \mu_{r3} = 1$, and $\sigma_1 = \sigma_3 = 0.01$ for the upper and lower layer, $\varepsilon_{r2} = 1$, $\mu_{r2} = 1$, and $\sigma_2 = 1$ for the middle layer. The boundaries are at z = 10 ft. and z = -10 ft. This is also the general case when the drilling bit is in the high resistivity layer.

a) Frequency = 2 MHz, spacing = 33.375 in.

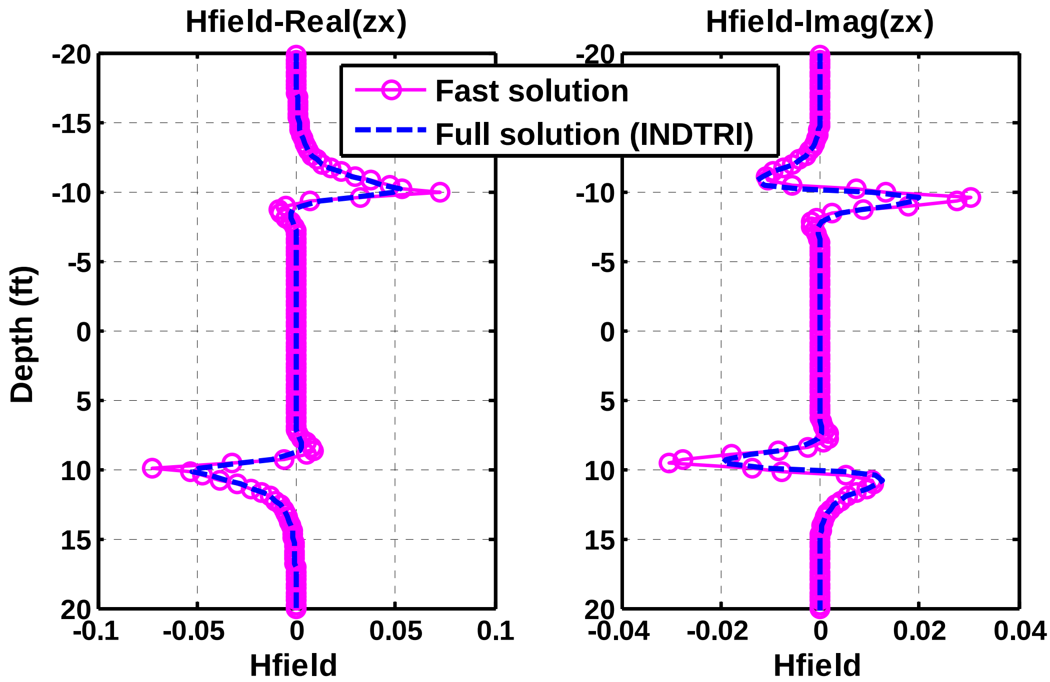

Figure 3.19 Tool response H_{zx} component ($\sigma_1 = \sigma_3 = 0.01$, $\sigma_2 = 1$, 2 MHz, long)

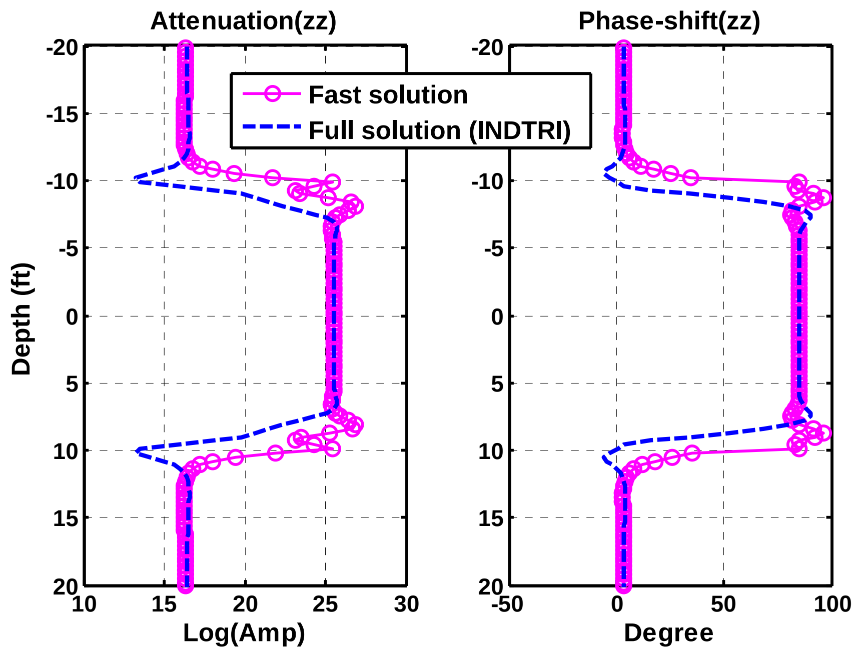

Figure 3.20 Phase difference and attenuation ($\sigma_1 = \sigma_3 = 0.01$, $\sigma_2 = 1$, 2 MHz, long)

b) Frequency = 2 MHz, spacing = 22.265 in.

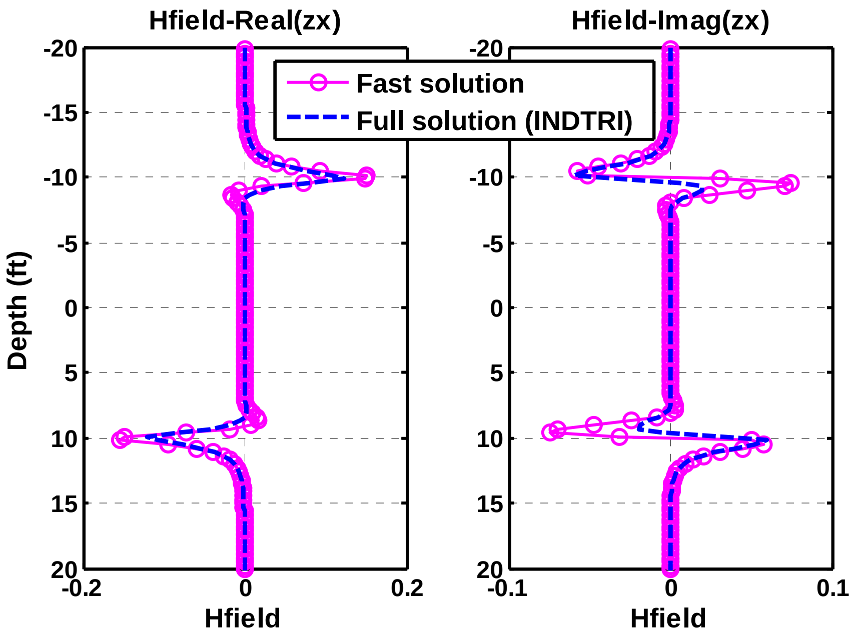

Figure 3.21 Tool response H_{zx} component ($\sigma_1 = \sigma_3 = 0.01$, $\sigma_2 = 1$, 2 MHz, short)

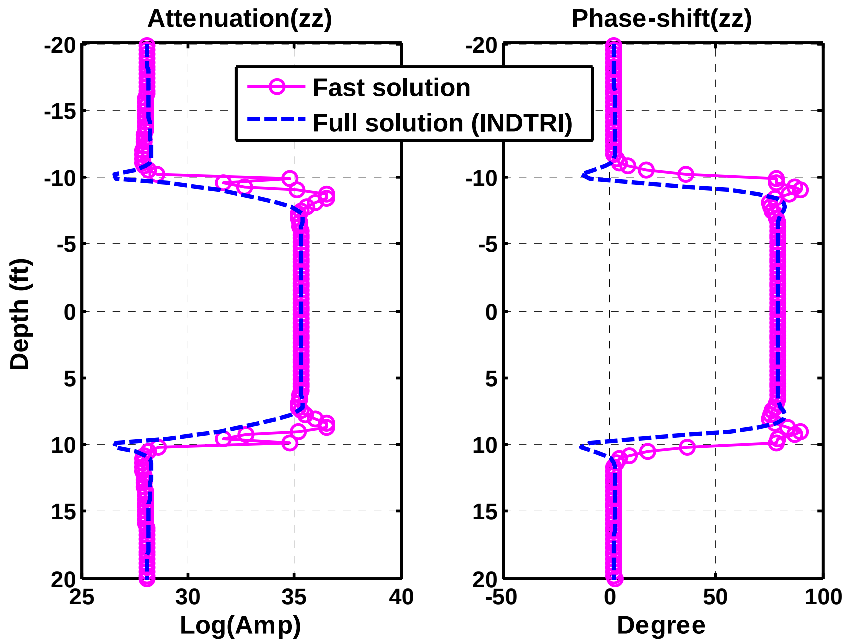

Figure 3.22 Phase difference and attenuation ($\sigma_1 = \sigma_3 = 0.01$, $\sigma_2 = 1$, 2 MHz, short)

c) Frequency = 400 KHz, spacing = 33.375 in.

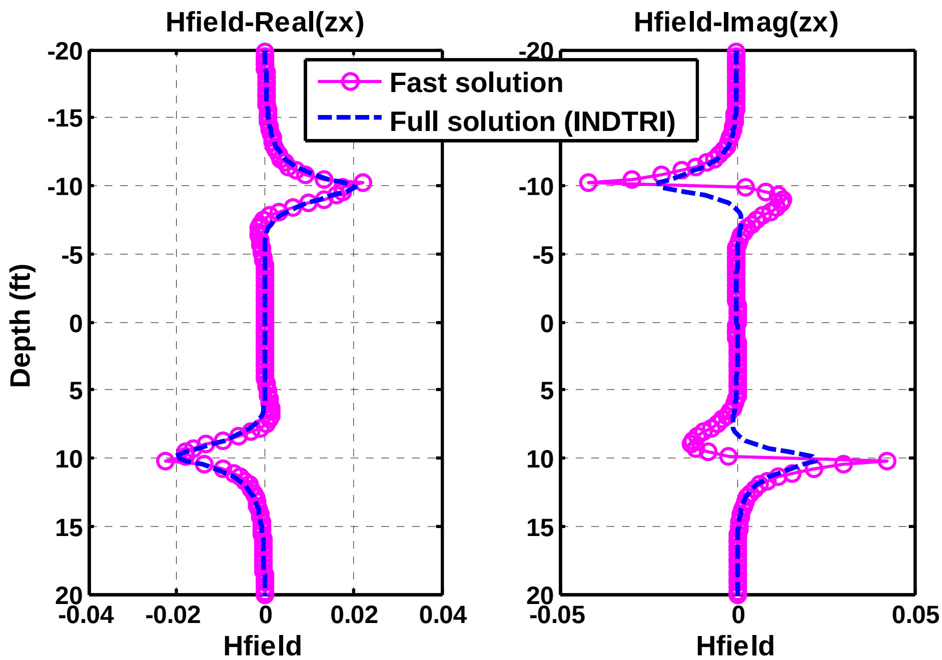

Figure 3.23 Tool response H_{zx} component ($\sigma_1 = \sigma_3 = 0.01$, $\sigma_2 = 1$, 400 KHz, long)

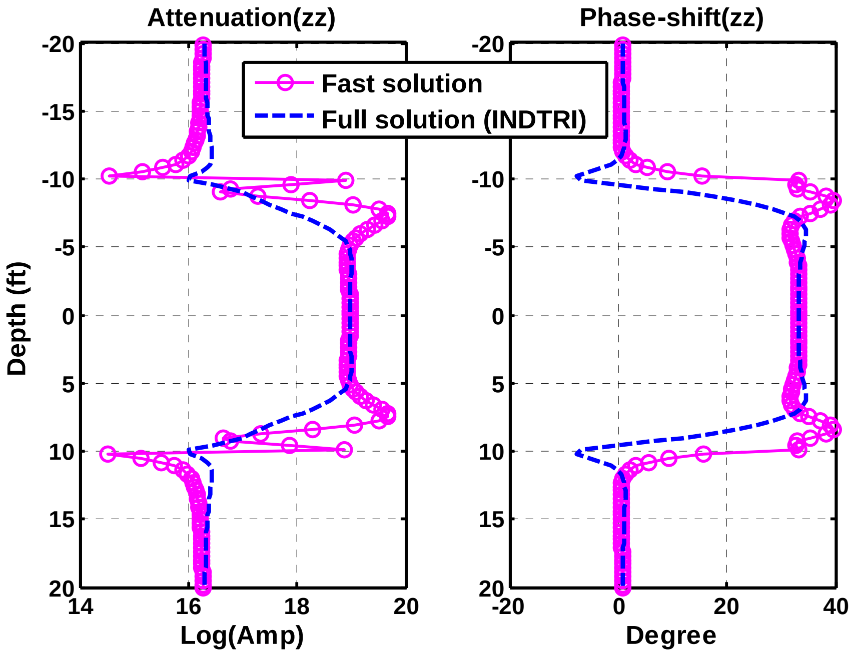

Figure 3.24 Phase difference and attenuation ($\sigma_1 = \sigma_3 = 0.01$, $\sigma_2 = 1$, 400 KHz, long)

d) Frequency = 400 KHz, spacing = 22.265 in.

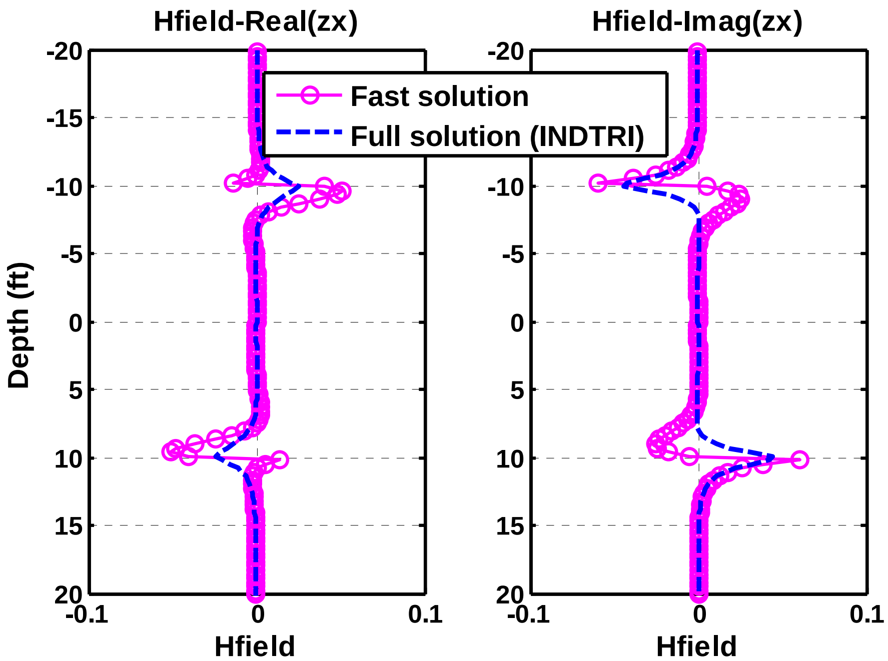

Figure 3.25 Tool response H_{zx} component ($\sigma_1 = \sigma_3 = 0.01$, $\sigma_2 = 1$, 400 KHz, short)

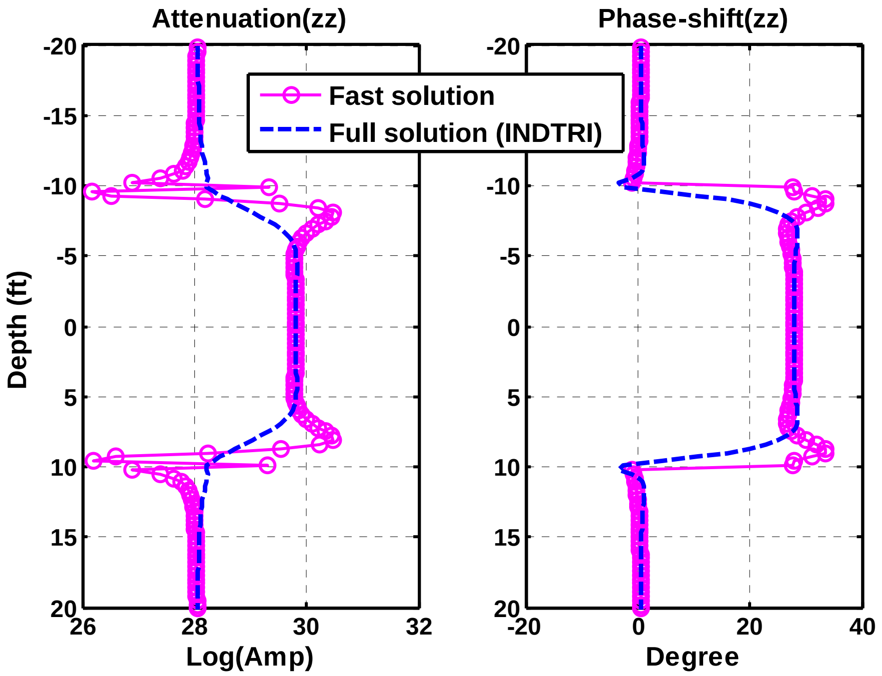

Figure 3.26 Phase difference and attenuation ($\sigma_1 = \sigma_3 = 0.01$, $\sigma_2 = 1$, 400 KHz, short)

Figure 3.19 to Figure 3.26 show the simulation results of full channels, when the middle layer of the formation is high conductive. Because the three-layer model is treated as the combination of two independent boundaries, the simulation results are similar to the ones where the middle layer is of high resistive. We find that the approximation method works well in this case. The cross component H_{zx}, phase shift and attenuation are all good enough to be used into boundary detection.

3.3.4 R_1 = 1 Ohm.m, R_1 = 20 Ohm.m, R_1 = 0.5 Ohm.m

In all the previous three cases, the upper layer and lower layer have the same conductivity, which means the models are all symmetrical. The unsymmetrical case is also tested. The parameters of these three layers are $\varepsilon_{r1} = \varepsilon_{r2} = \varepsilon_{r3} = 1$, $\mu_{r1} = \mu_{r2} = \mu_{r3} = 1$, and $\sigma_1 = 1, \sigma_2 = 0.05, \sigma_3 = 2$. The boundaries are at z = 10 ft. and z = -10 ft. This case is more general as in real application.

Similar, four channels are all tested in this case. As is expected, the approximation method also works well in this unsymmetrical formation. The approximation method can be also used into the layer with relatively high conductivity. One additional term was introduced to correct the image results. The real part of cross components H_{zx} has more accuracy than the imaginary part, which indicates that it is better to extract the boundary information only from the real part of the signal. Compared with the cross component, although there is a little bit more error of phase shift and attenuation, the logging values away from boundaries are good enough to invert the apparent resistivity of the formation. So, the approximation method can be used into the application of geo-steering. The boundary information can be extracted from the cross component.

a) Frequency = 2 MHz, spacing = 33.375 in.

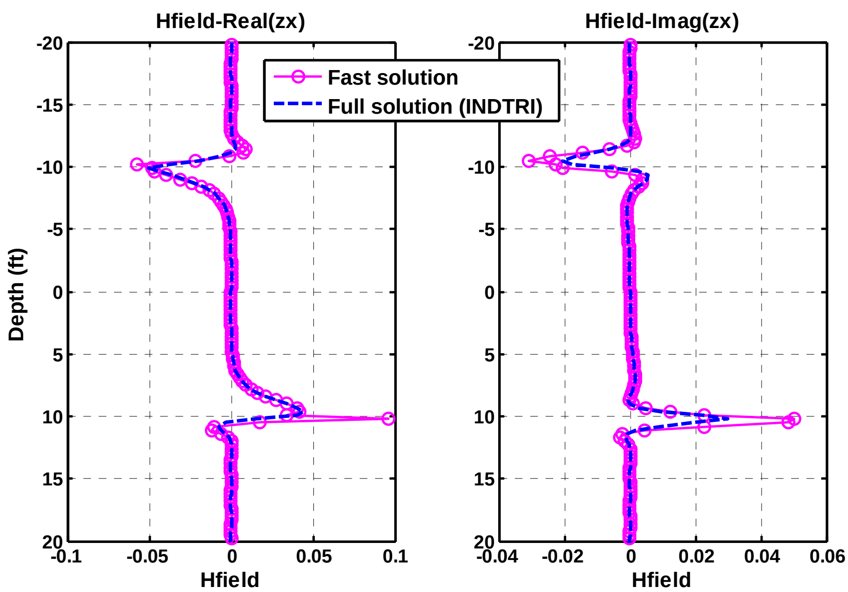

Figure 3.27 Tool response H_{zx} component ($\sigma_1 = 1, \sigma_2 = 0.05, \sigma_3 = 2$, 2 MHz, long)

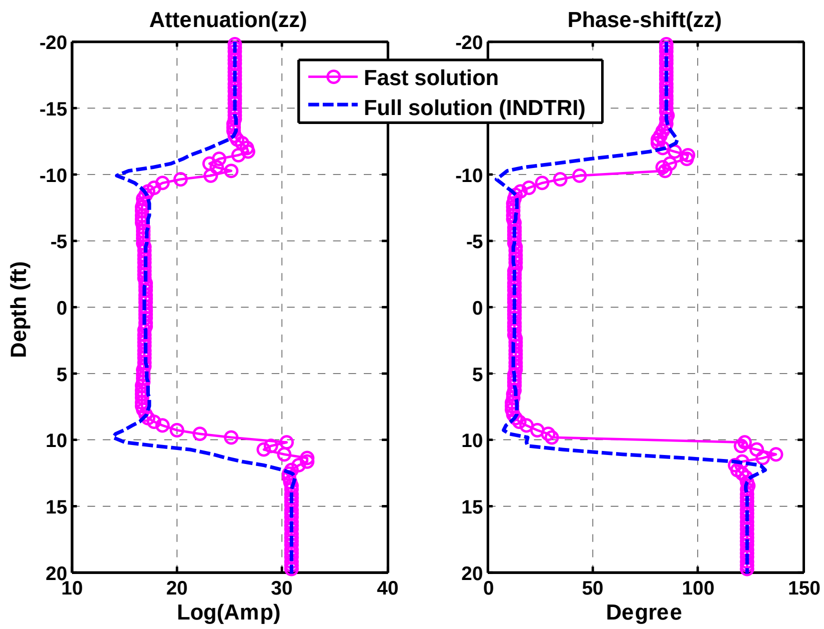

Figure 3.28 Phase difference and attenuation ($\sigma_1 = 1, \sigma_2 = 0.05, \sigma_3 = 2$, 2 MHz, long)

b) Frequency = 2 MHz, spacing = 22.265 in.

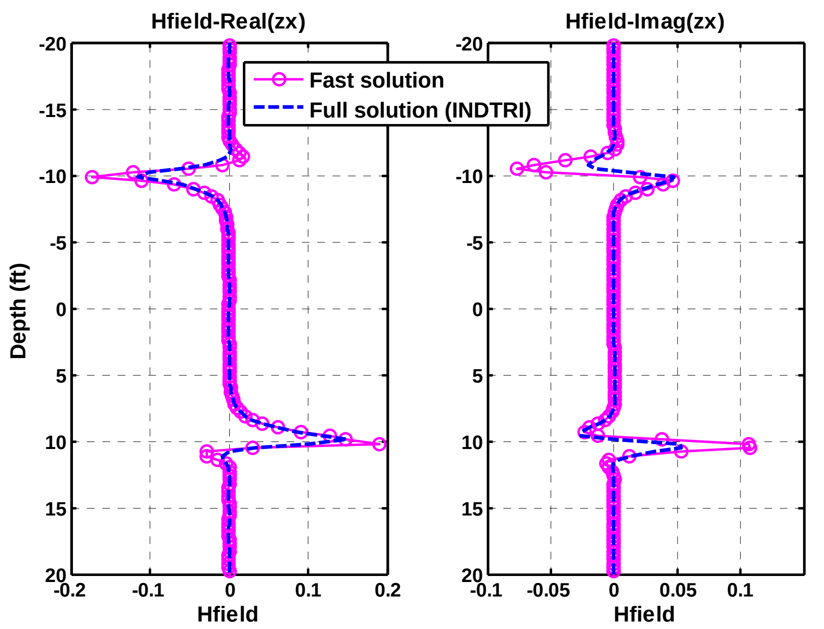

Figure 3.29 Tool response H_{zx} component ($\sigma_1 = 1, \sigma_2 = 0.05, \sigma_3 = 2$, 2 MHz, short)

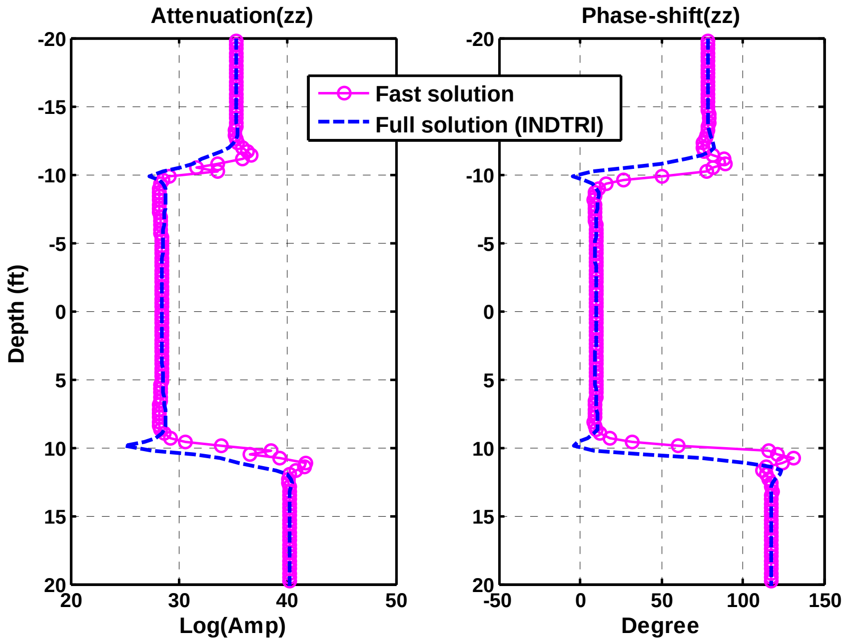

Figure 3.30 Phase difference and attenuation ($\sigma_1 = 1, \sigma_2 = 0.05, \sigma_3 = 2$, 2 MHz, short)

c) Frequency = 400 KHz, spacing = 33.375 in.

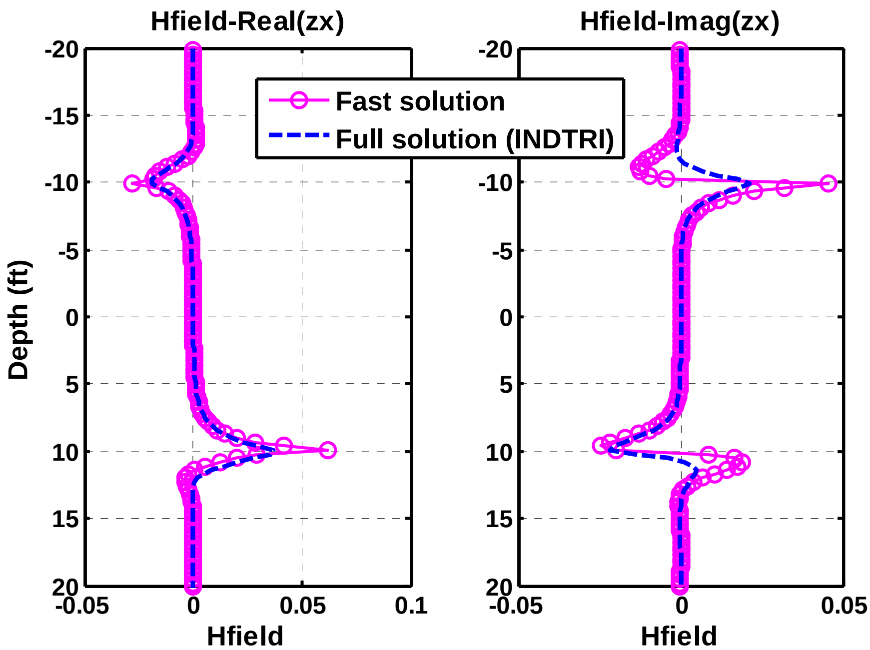

Figure 3.31 Tool response H_{zx} component ($\sigma_1 = 1, \sigma_2 = 0.05, \sigma_3 = 2$, 400 KHz, long)

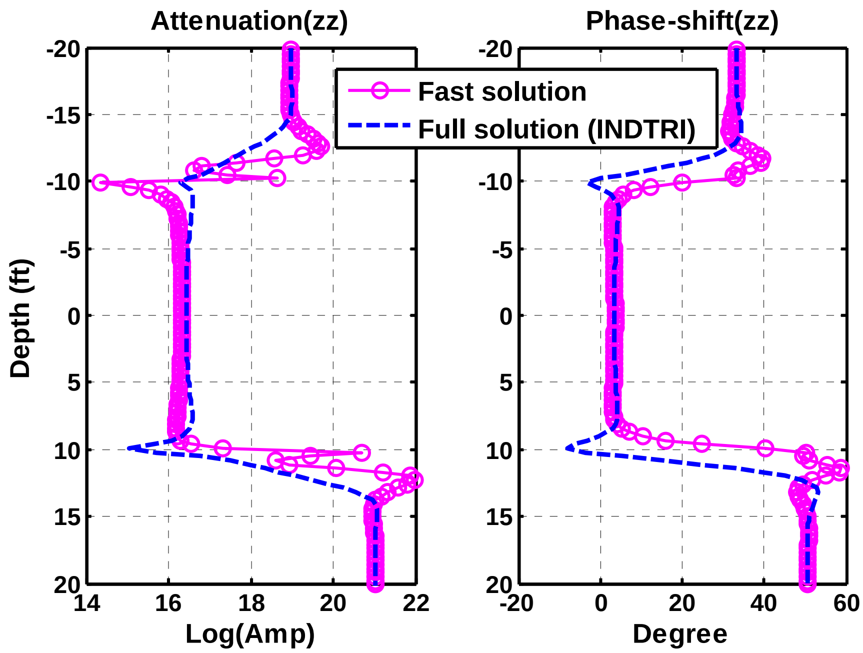

Figure 3.32 Phase difference and attenuation ($\sigma_1 = 1, \sigma_2 = 0.05, \sigma_3 = 2$, 400 KHz, long)

d) Frequency = 400 KHz, spacing = 22.265 in.

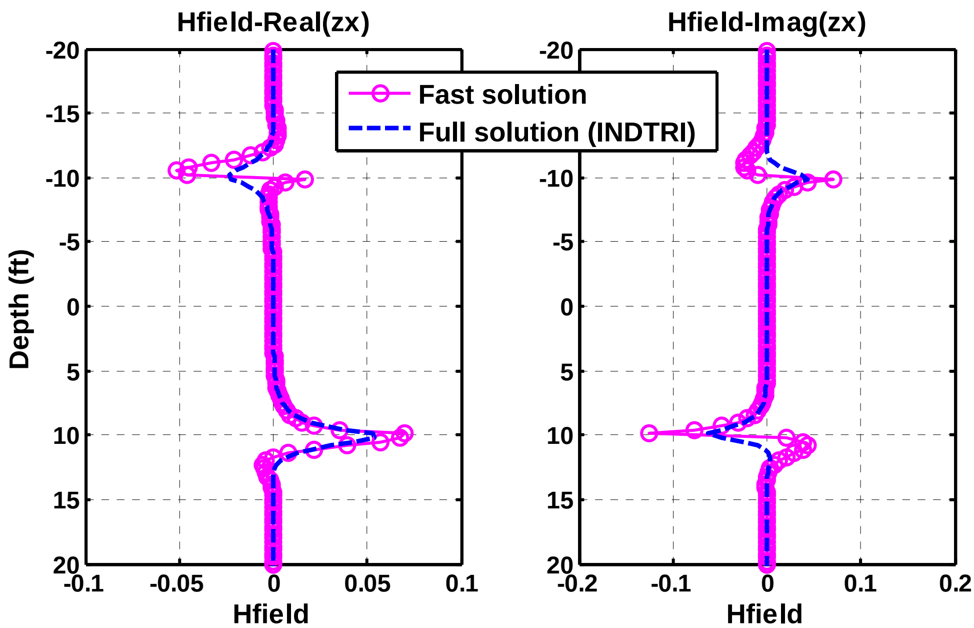

Figure 3.33 Tool response H_{zx} component ($\sigma_1 = 1, \sigma_2 = 0.05, \sigma_3 = 2$, 400 KHz, short)

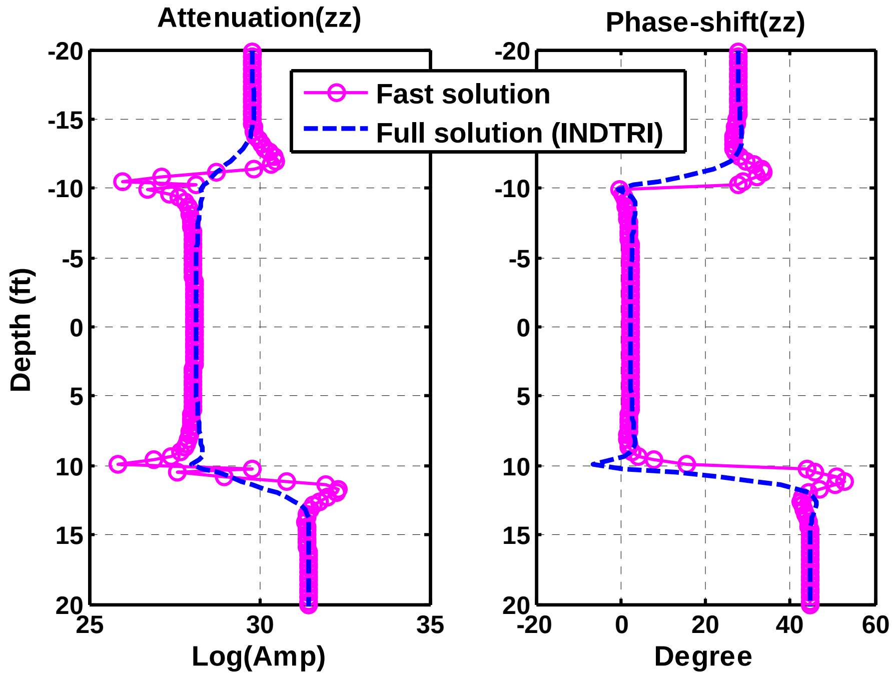

Figure 3.34 Phase difference and attenuation ($\sigma_1 = 1, \sigma_2 = 0.05, \sigma_3 = 2$, 400 KHz, short)

3.4 Discussion

According to the simulation results, cross component H_{zx} shows that nonzero values only exist near boundary. In the area far away from boundary, the values of H_{zx} are zero. This is the advantage of the orthogonal configuration tool. The cross component is only sensitive to the boundary. When the tool is approaching the boundary, the cross component will decrease. Then when the distance from the drilling bit to the boundary is larger than a specific value, the tool cannot detect the boundary any more. Based on the simulation results we have, tool's sensitivity of boundary is affected by the combination of frequency and spacing. Besides, the conductivity of formation also affects the tool response.

3.4.1 Effects of Conductivity Contrast

In this section, the tolerance of the image method at different conductivities contrast will be investigated for the two-layer model, as shown in Figure 3.35. The upper layer of the model is a low conductivity layer. The resistivity of the lower layer varies from 10 Ohm-m to 1k Ohm-m. The tolerance of the image method is tested at 2 MHz and antenna spacing is 34 in.

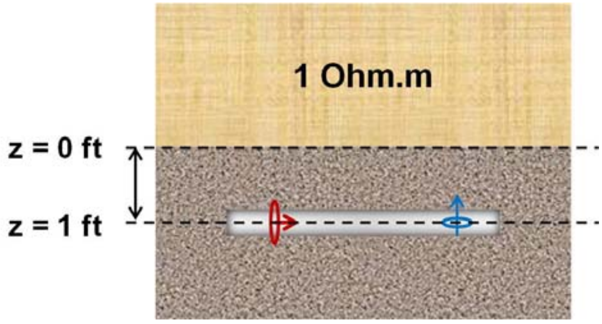

Figure 3.35 Observation point 1ft. away from boundary

Figure 3.36 and Figure 3.37 show the absolute error and relative error between the approximation results and full solution results at the observation point one ft. and two ft. away from the boundary, respectively. The results show that when the resistivity ratio between the upper layer and the lower layer is increased, the error between the approximation method and the full solution converges. The relative error of the *xz* component is smaller when the resistivity ratio of the upper layer and the lower layer is larger. At the observation point one ft. away from the boundary, when the resistivity ratio between the upper layer and the lower layer is more than 100, the absolute error is less than 0.0123; the relative error between the approximation method and the full solution is about 15%. When the observation point is at the area two ft. away from the boundary, the error will be less.

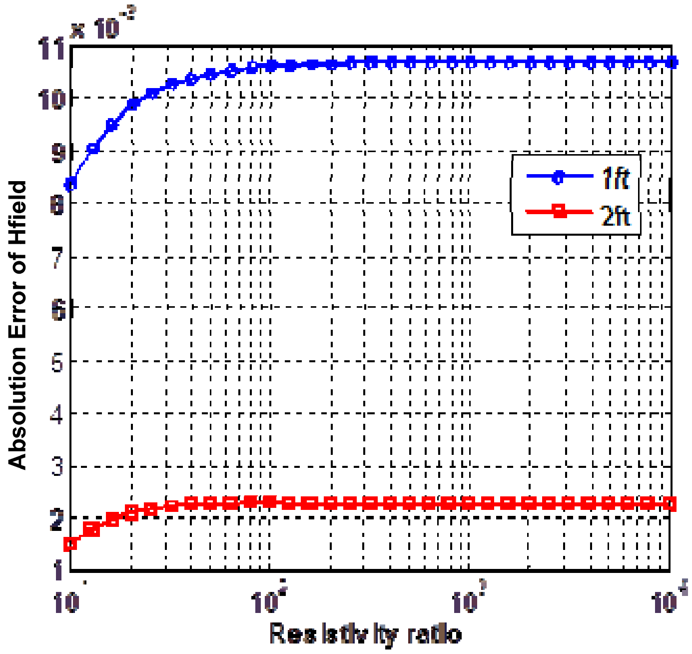

Figure 3.36 Absolute error of 2MHz tool at 1ft away from boundary

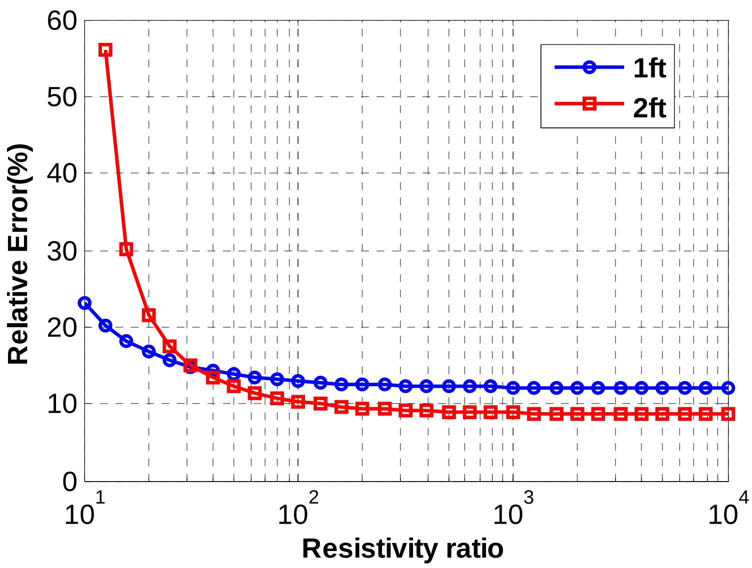

Figure 3.37 Relative error of 2 MHz tool at 1ft away from boundary

3.4.2 Frequency

In term of practical application, assume that the current excited into the transmitter is 200 mA. The area of antenna is 2.5 in^2. Then, the moment of single turn antenna is about 3.2e-4 A·m^2. Then the H_{zx} data in Figure 3.3 and Figure 3.7 can be converted to the received voltage signal, shown in Figure 3.38. For evaluating the sensitivity of the boundary detection, the detectable minimum signal power should be considered. Currently, the minimum detectable voltage is about 100 nV.

In Figure 3.38, the H_{zx} is converted into voltage by considering that the transmitter has only single turn and its moment is 3.2e-4 A·m^2. The parameters of the formation is $\sigma_1 = \sigma_3 = 1$ and $\sigma_2 = 0.01$. The yellow line shows the minimum voltage value that can be detected by the sensor.

As shown in Figure 3.38, in high resistive area, tool responses at two working frequencies have similar sensitivities. The signal of cross component fades to zero at the position about five ft. away from the boundary. In the high conductive range, the signal decays even further. The detectable distances are around two ft. to four ft. In this range, the high frequency signal decays faster, so the relatively low frequency working channel has better sensitivity. Tool can detect further at the relatively low frequency.

Similarly, by comparing the simulation results in other formations, we can always get at least five ft. detectable distance in high resistive region. The detectable distances in high conductive region are different caused by the different working frequencies. Low frequency channel has larger detectable distance.

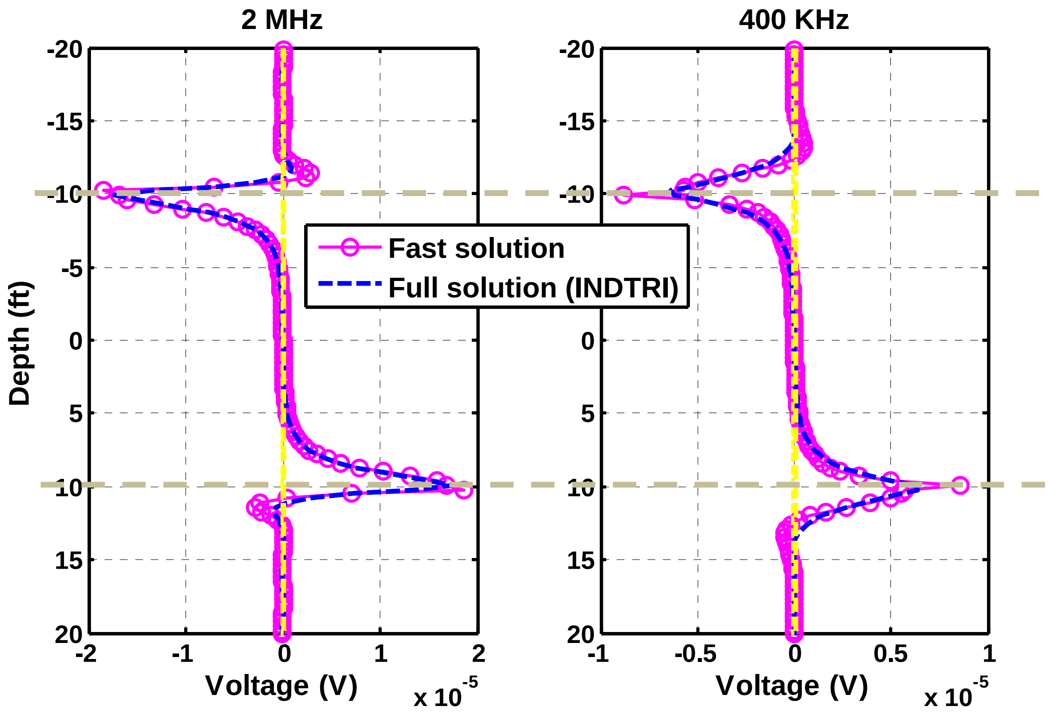

Figure 3.38 Voltage signal generated by cross component H_{zx} of single turn transmitter

$(\sigma_1 = \sigma_3 = 1, \sigma_2 = 0.01)$

3.4.3 Spacing

Figure 3.39 Two-layer model with boundary at z = 0ft

To investigate the effect of spacing, two-layer model with only one boundary is considered, shown in Figure 3.39. The parameters of the two layers are $\sigma_1 = 1$ and

$\sigma_2 = 0.01$. The boundary is located at z = 0. For testing the effect of spacing, frequency should be fixed. The fixed frequency is chosen to be 400 KHz, simply because the detectable distance is larger at low frequency. The spacing range is from 33 in. to 55 in.

Figure 3.40 shows the cross component simulation results with different spacing. The results are all divided by 100 nV, which is the minimum detectable voltage in application. When the spacing is larger, the peak at the boundary is lower. In the high resistive region, the detectable distance is larger. On the contrary, in the high conductive region, the detectable distance becomes smaller. Re-plot the results in log scale in Figure 3.41. It's easy to find that when spacing is 55 in., the detectable distance is about seven ft. The other thing the detectable distance is not sensitive to the spacing. That probably because the wavelength effect, which is compared with the wavelength, the spacing is relatively small. The property is good for tool design, which means the tool doesn't need to be too long.

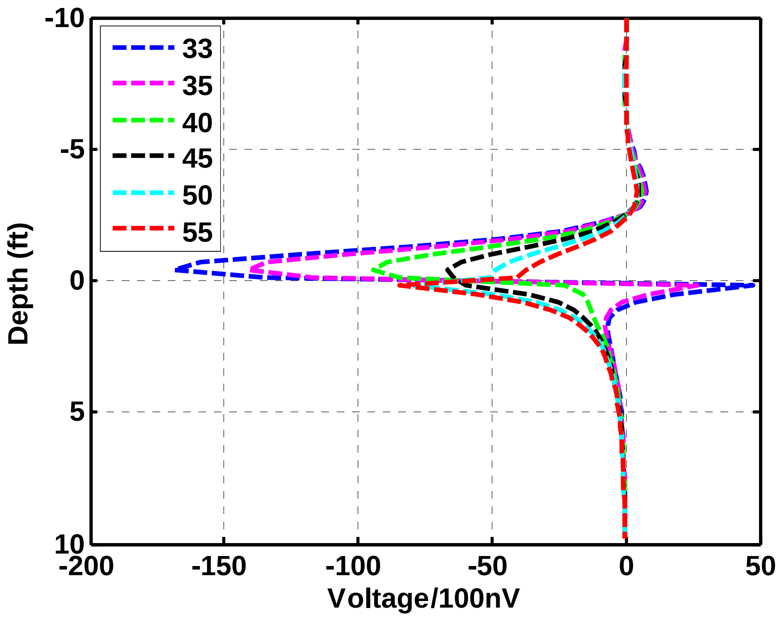

Figure 3.40 Cross component response vs. 100nV in different spacing (400 KHz)

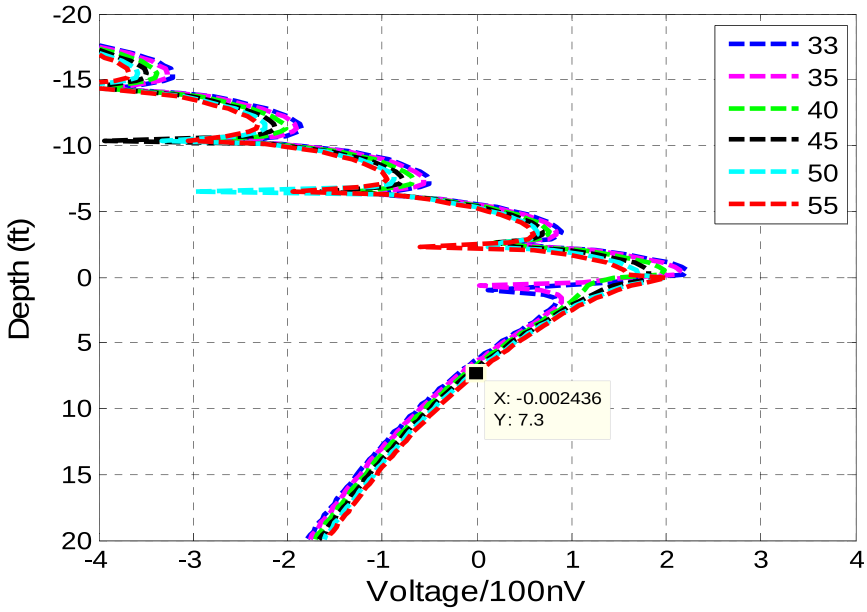

Figure 3.41 Cross component response vs. 100nV in different spacing in log scale (400 KHz)

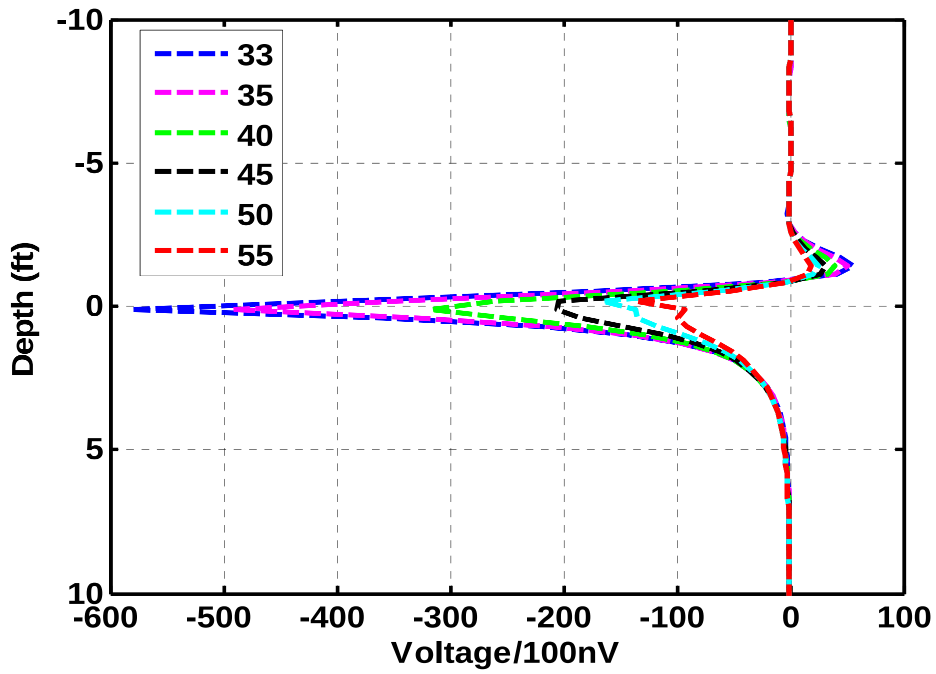

Figure 3.42 Cross component response vs. 100nV in different spacing (2 MHz)

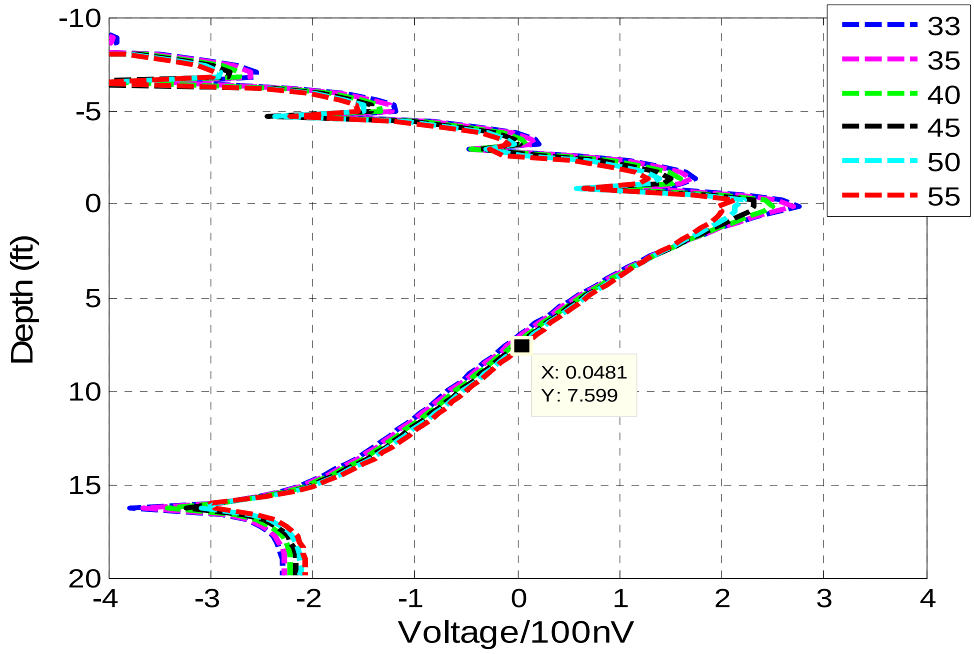

Figure 3.43 Cross component response vs. 100nV in different spacing in log scale (2MHz)

Figure 3.42 and Figure 3.43 show the same results when the tool is working at 2 MHz. Compared with the results at 400 KHz, when both transmitter and receiver have 1 turn, with spacing 55 in., the detectable distance of both frequency are around seven ft. However, when transmitter has ten turns, the receiving signal will be enlarged 10 times. In this situation, the tool working at 400 KHz has larger detectable distance than the tool working at 2 MHz.

3.4.4 Calculation Speed

Table I shows the CPU time comparison between the image method and the full solution for different numbers of iterations. The results show that the image method is much faster than the full solution. When the number of total logging points are 600,000, the image method is 160 times faster than the full solution. In addition, when iterative times increase, the image method will have a greater advantage in computation speed.

Testing model: Three-layered model

Testing tool: Frequency = 2 MHz Antenna Spacing = 19 in.

CPU parameter: Intel Q8200 @2.33GHz with 8.00 GB RAM

Table 1 Computation speed testing

Logging Points	6,000	60,000	600,000
Image Method (s)	0.12	0.59	5.37
Full Solution (s)	8.67	86.17	859.88
Speed Ratio	72	150	160

3.4.5 Logging with high deviated angle

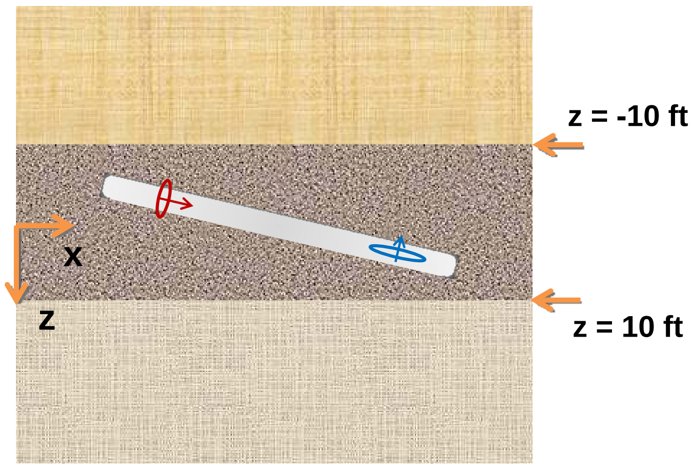

Figure 3.44 High deviated well in 3-layer formation

Until now, all simulation cases assume a horizontal well. However, in the real application, most cases are not in exactly horizontal situation. To further understand the effectiveness of the image theory method, the well with high deviated angle is investigated. The schematic of the well with high deviated angle is shown in Figure 3.44, where the tool is not exactly horizontal placed. The dipping angle of the simulated tool is from 60° to 85°. For convenience, phase shift and amplitude ratio is not shown. Only the cross component response is shown below.

The three-layer 1D model is shown in Figure 3.44. The parameters of this formation are $\varepsilon_{r1} = \varepsilon_{r3} = 1$, $\mu_{r1} = \mu_{r3} = 1$, and $\sigma_1 = \sigma_3 = 1$ for the upper and lower layer, $\varepsilon_{r2} = 1$, $\mu_{r2} = 1$, and $\sigma_2 = 0.01$ for the middle layer. The boundaries are at z = 10 ft. and z = -10 ft. The logging is working at 2 MHz and the spacing is 34 in.

a) Dipping angle = 85°

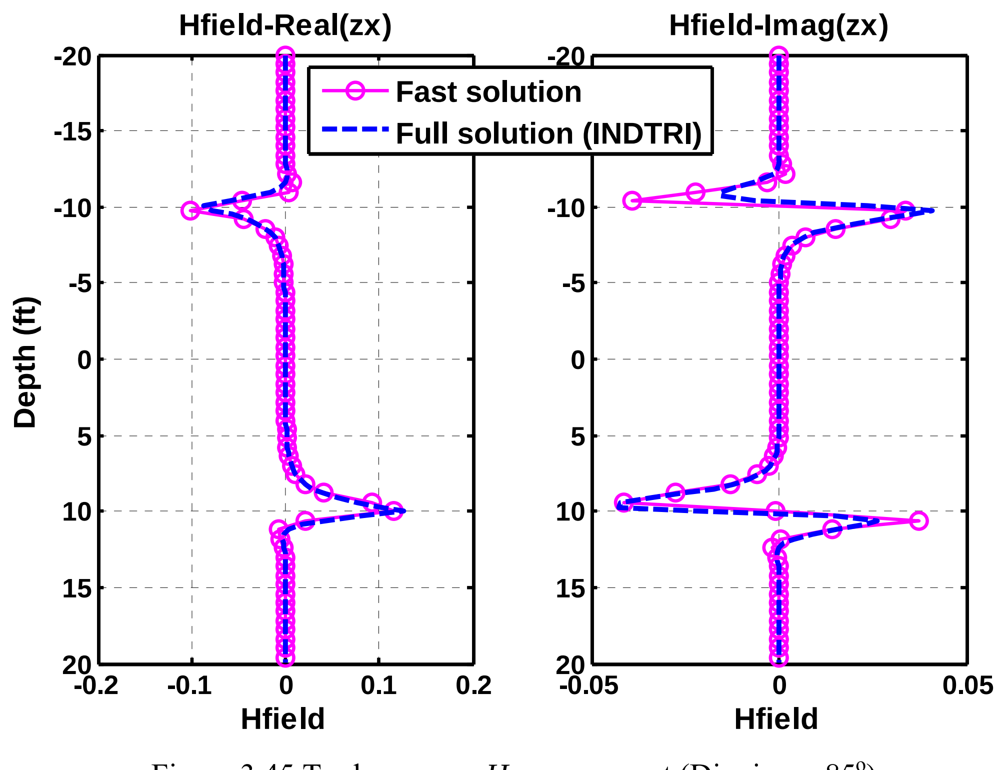

Figure 3.45 Tool response H_{zx} component (Dipping = 85°)

Figure 3.45 shows that when the dipping angle is 85°, the cross component of the simulation results. Because in this case, the tool is almost horizontally placed, the simulation results look similar as the case when the logging tool is placed exactly horizontally. Comparing the image theory method with the full solution, there is not much difference. The complex image theory works pretty well when the logging tool is placed almost horizontally.

b) Dipping = 75^o

Figure 3.46 shows the simulation results when the dipping angle is reduced to 75^o. In this case, the complex image method works well too. The fast solution shows enough agreement with the full solution. In addition, because the tool is not horizontal with the bed boundaries, although the formation is symmetry, the simulation results become asymmetry. The cross component shows stronger response at the lower boundary.

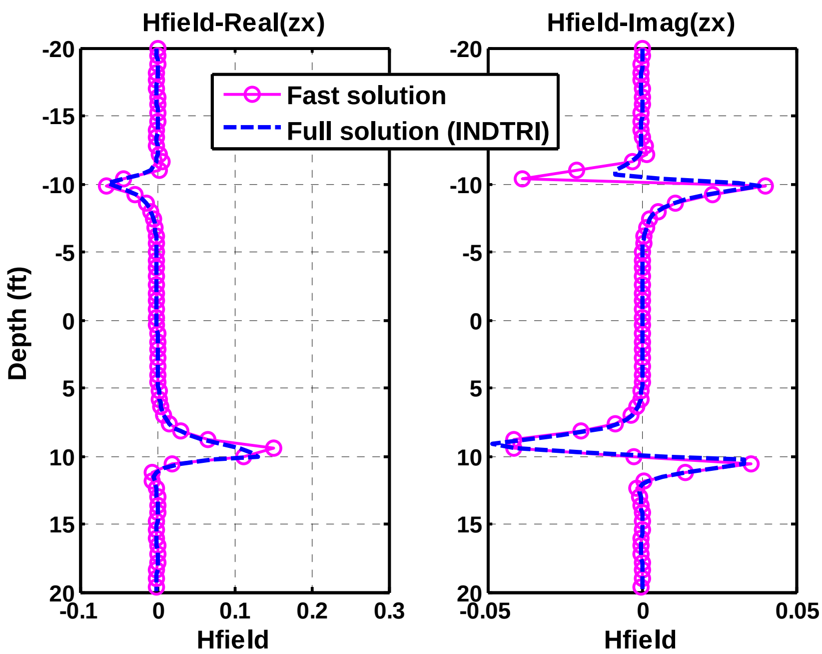

Figure 3.46 Tool response H_{zx} component (Dipping = 75^o)

c) Dipping angle= 65^o

When the dipping angle goes to 65°, the asymmetry of the cross component is more obvious, as shown in Figure 3.47. In this case, the complex image method gives the large peak when the tool is across the lower boundary. But, in the area near the upper boundary, the simulation results from complex image method can follow the full solution results closely. The reason is that, when the dipping angle is less than 90°, for the upper boundary, the transmitter is closer to the boundary and the receiver is relatively further away from the boundary. In opposite, for the lower boundary, the receiver is closer to the boundary than the transmitter. As the instruction shown before, the complex image method has larger error in the area near the boundary. So, in the Figure 3.47, there is lager error appearing near the lower boundary. But, as shown in Figure 3.47, the error is still within two to three ft. from the boundary. This is acceptable in the application of geo-steering system.

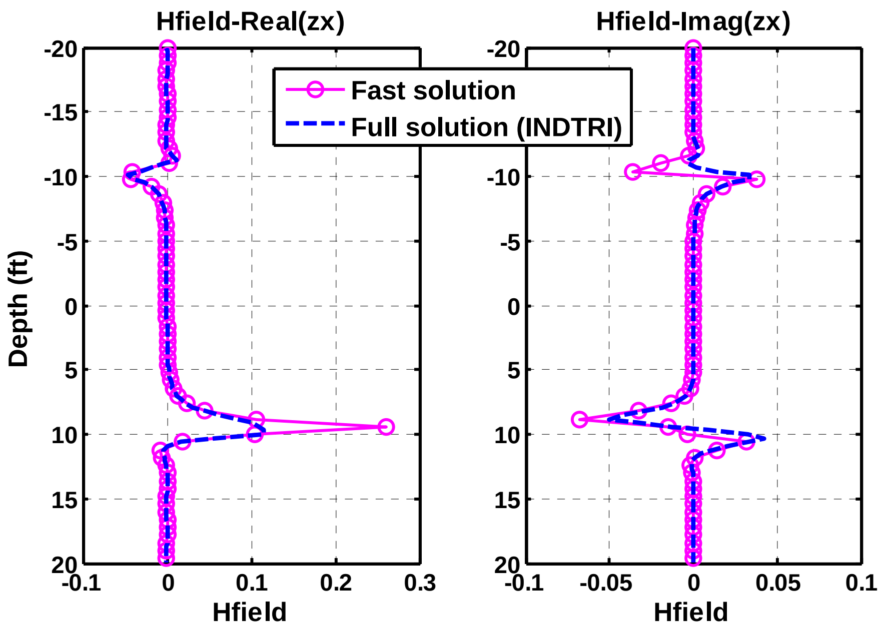

Figure 3.47 Tool response H_{zx} component (Dipping = 65°)

d) Dipping angle= 60°

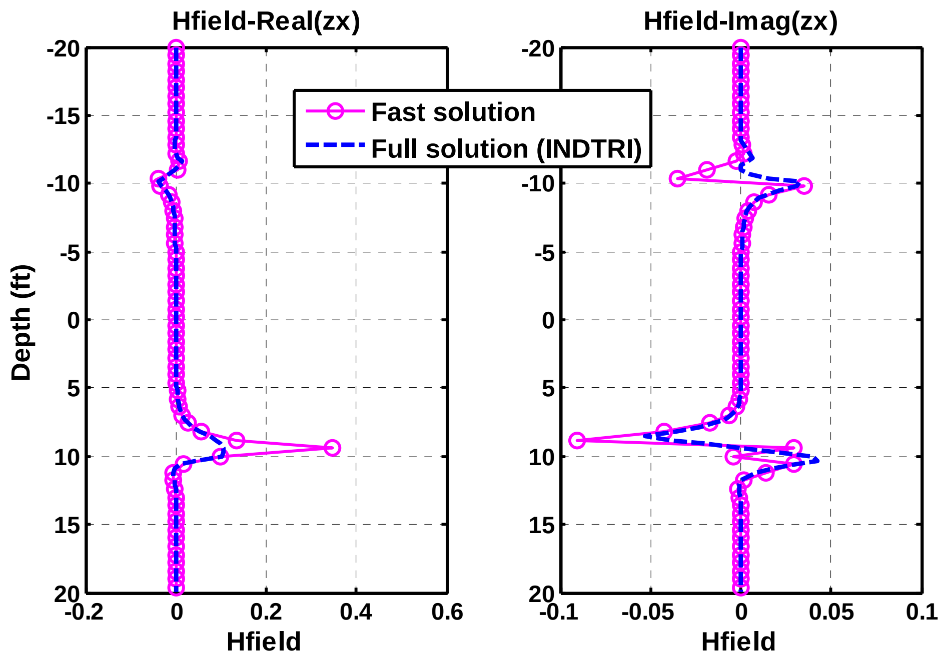

Figure 3.48 Tool response H_{zx} component (Dipping = 60^{o})

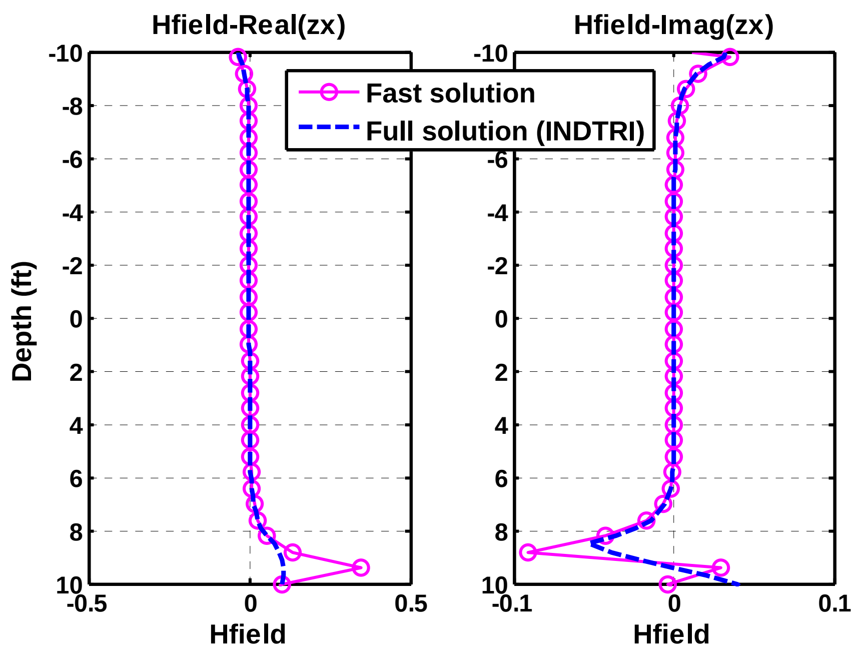

Figure 3.49 Tool response H_{zx} component in the middle layer (Dipping = 60^{o})

Similar, Figure 3.48 shows the cross component of the simulation results when the dipping angle is 60^o. Because the dipping angle is much more less than horizontal case, the simulation results shows more obvious asymmetric and the complex image method gives larger error near the lower boundary. It's already shown in Figure 3.44, that the middle layer is relative high resistive layer. Zoom in the figure and show the middle layer only in Figure 3.49. The simulation results show that the complex image method works well in the relative high resistive layer, even when the dipping angle is 60^o. The simulation results of complex image method can follow the variation of the results from full solution in the most area. Error only occurs near the lower boundary and the error area is within two ft. away from the boundary. Based on the discussion above, it can be concluded that the complex image method can work in the highly deviated well with dipping angle varying from 60^o to 90^o.

Chapter 4 Boundary Distance Inversion

4.1 Theory of Inversion

An inverse problem is a general framework used to convert observed measurements into information about a physical object or system. Basically, it is based on some pre-designed forward modeling. Depends on different requirements, many kinds of method can be used in to solve this problem.

4.2 Workflow of Inversion Problem

For real-time adjustment, Geo-steering system is a negative feedback system, which adjusts the direction of the drilling bit based on the real-time data collected from down hole. Such data includes the real-time position of the drilling bit and its distance away from the boundary. Boundary Detection is thus the key part of this system. A fast and accurate method is essential for real-time control.

Boundary detection is usually modeled as an inversion problem. In an iterative manner, we are to minimize the difference between the data collected from the receiving antenna and the simulation results from the forward modeling in certain tolerance. The value of parameters, for example, the distance to boundary, is calculated as a byproduct in the minimization process. Figure 4.1shows the flow chart of inversion process, which generally includes forward modeling and model correction. Because of such iterative procedure, real-time system requires that the forward modeling, which calculates the field distribution of dipole in multilayered media, to be fast and accuracy.

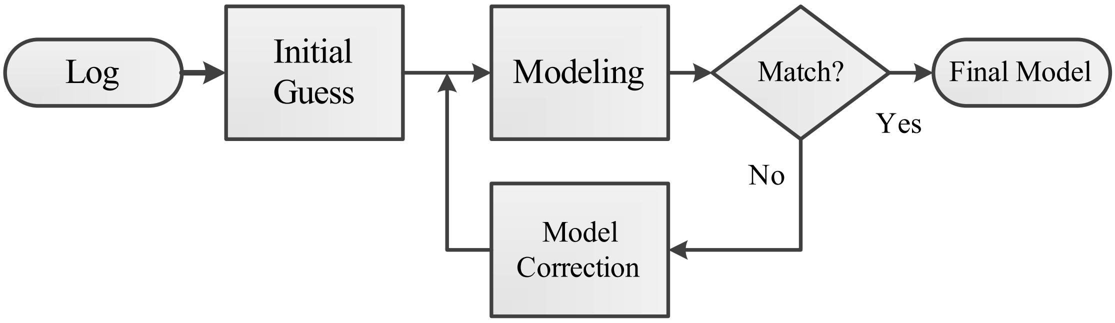

Figure 4.1 Flow chart of inversion problem

4.3 Processing Flow of Boundary Detection in Geo-steering

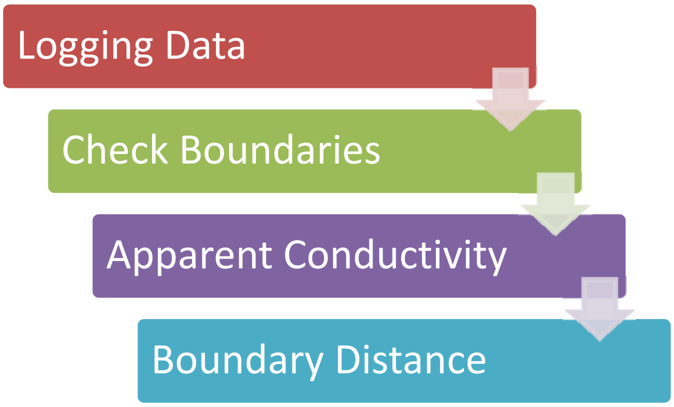

Figure 4.2 Boundary distance inversion flow

In the geo-steering system, there are three steps to process the measurement before going to the boundary distance inversion. Those steps help the system to get the basic information of the formation and initial the simulation model used into the boundary distance inversion. Figure 4.2 gives the general flow of such process. Firstly, logging data is collected by the receiver. Secondly, a brief geological model of the formation is generated from the logging data. This step mainly focuses on finding the positions of all boundaries. Thirdly, based on the phase-shift and attenuation of each layer, the apparent resistivity of each layer can be inverted out.

After those three steps, the depth of the boundary, the apparent conducvities of both layers and the logging curves are ready. The only unknown is the distance from the drilling bit to the boundary. Then follow the flow chart shown in Figure 4.1, by iterating the forward modeling, the optimized boundary distance can be inverted out. Because the boundary inversion in last step is supposed to be finished downhole, the fast forward modeling is required. The complex image method discussed in this paper is used to speed up the last step, which is the boundary distance inversion.

4.4 Bolzano Bisection Method

The bisection method is a root-finding method that repeatedly bisects an interval and then selects a subinterval in which a root must lie for further processing.

For a real variable x, where f is a continuous function $f(x)=0$ defined on an interval [a, b] and f(a)f(b) < 0. Then, f(x) has at least one root in [a, b]. The procedure of the bisection is shown below.

Firstly, let [a, b] = [a_1, b_1], denote the middle point of [a, b] as p_1,

$$p_1 = \frac{a_1 + b_1}{2}. \tag{45}$$

Give a threshold of length (TOL) (small enough). Plug p_1 back into the equation. If $\left|f(p_1)\right| < TOL$, then p_1 is the approximate root of the equation f(x) = 0. If $\left|f(p_1)\right| > TOL$, we will search the root in the interval [a_1, p_1] or [p_1, b_1].

Secondly, if $f(p_1)f(b_1)>0$, the root will be in the interval [a_1, p_1]. Else, the root will be in the interval [p_1, b_1]. Then the searching region is reduced by half. Repeat the previous steps, the approximate root with acceptable error will be found.

4.5 Simulation Results

The parameters of logging tool used in following cases:

Frequency = 2 MHz, Spacing = 36.375 in. and the dipping angle is 90°.

4.5.1 Sensitivity of Depth

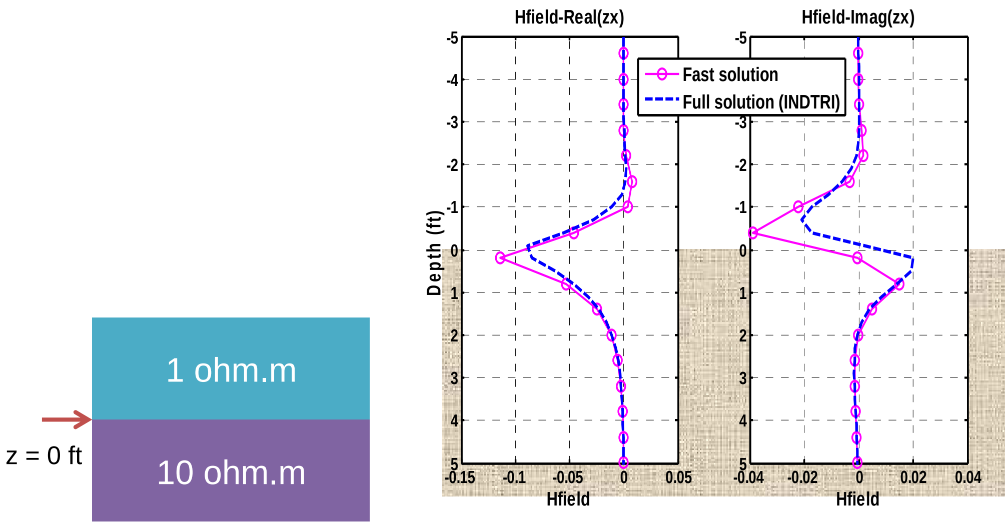

Figure 4.3 Testing model of inversion processing (R_1:R_2 = 1:10)

Sensitivity of depth is a parameter defined by $\Delta H/\Delta d$, which represents the variation speed of H field along with varies of depth. Higher sensitivity of depth contributes higher convergence speed of boundary distance inversion. It is an important parameter to choose the component used into boundary distance inversion.

One 2-layer model was used to test the inversion process. As shown in Figure 4.10, the 2-layer model has one boundary at z = 0 ft. The resistivities of the two layers are 1 Ohm-m and 10 Ohm-m, respectively. The right hand side of Figure 4.3 shows the simulation results of H_{zx}.

Figure 4.4 shows the depth sensitivity of the real part and amplitude of cross component, respectively. Because the real part and imaginary part of H_{zx} almost follow the same trend, there is not much difference shown in Figure 4.4. From zero to four ft., the absolute value of sensitivity are all larger than 0. This indicates that, in this range of depth, both the real part and the amplitude of the cross component can be used to inverse the boundary distance. Re-plot the depth sensitivity in Figure 4.5, which only shows the depth from four to ten ft. From this figure, it's easy to see that, the depth sensitivity of the amplitude of cross component decreases as the depth increases. But the absolute value of amplitude sensitivity is always larger than zero. However, the sensitivity of the real part of cross component moves closer to zero when the depth is larger than six ft. That means, with a depth larger than 6 ft., the real part of the cross component is non-sensitive to the boundary. With a depth from six to ten ft., the amplitude of cross component gives better performance.

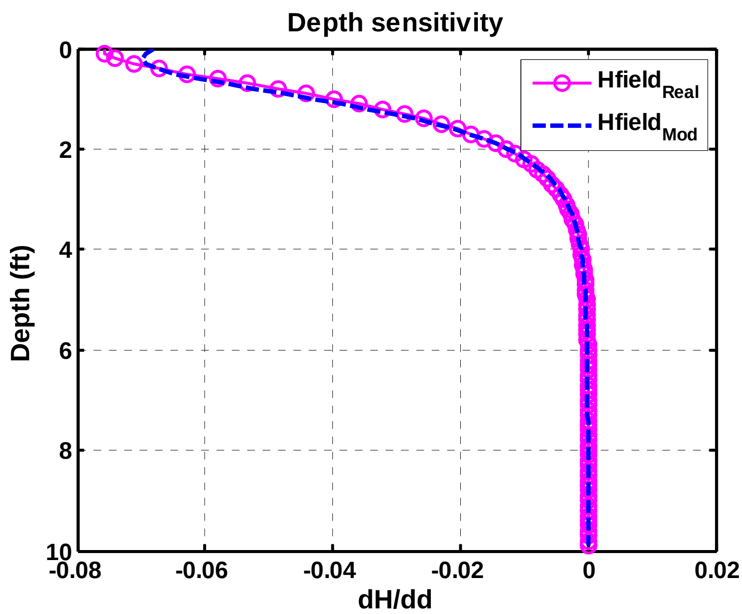

Figure 4.4 Depth sensitivity of H_{zx} (0ft. to 10 ft.)

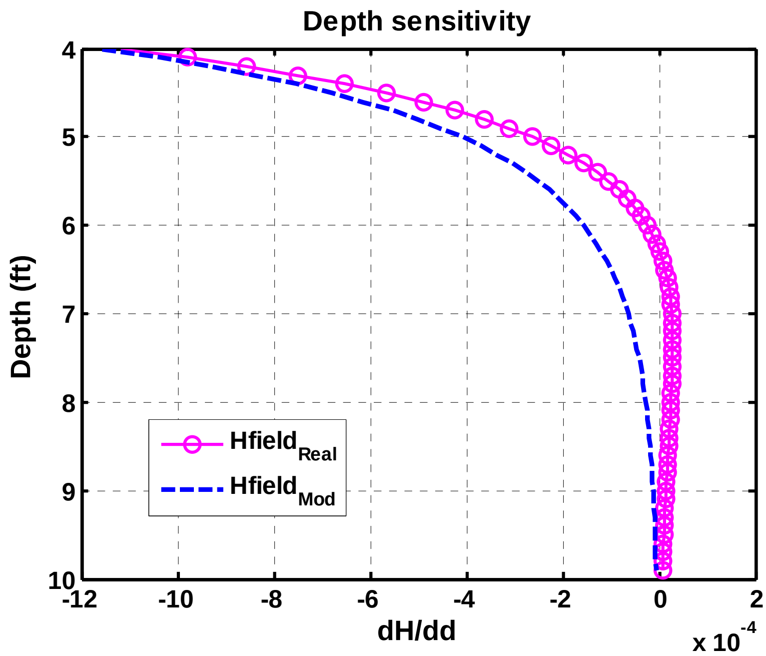

Figure 4.5 Depth sensitivity of H_{zx} (4ft. to 10 ft.)

4.5.2 R_1 = 1 Ohm.m, R_2 = 10 Ohm.m

Based on the processing flow shown in Figure 4.2, the boundary distance is last to calculate the distance from the drilling bit the boundary. In this processing, the apparent resistivity of the formation and the depth of the boundary are already known. The distance is the only unknown. For each distance, there will be a received H_{zx} corresponding. Then based on this model, by combining the received signal, the distance away from the boundary can be calculated. Generally, it can be calculated by solving a one unknown equation. The problem is that this equation is of high order. The unknown cannot be solved explicitly. In this part, Bisection method is used to calculate the distance.

Assume the unknown distance is d. We thus have a high order equation,

$$f(d) = V_r, \tag{46}$$

where V_r is the measurement of received H_{zx}. Rewrite the equation as

$$f(d) - V_r = 0. \tag{47}$$

Then the problem is to find the root of Equation 4.7. Here, the H_{zx} measurement is obtained from the analytical full solution. The inversion process is running the forward modeling with complex image theory. Because we already know the position of the boundary, in this case, the boundary is at z = 0; and in the most case, the logging tool is working in the high resistivity side, in this case, the high resistivity side is located in the area z > 0. In this part, only lower half space was tested. In the most cases, the tool is working in the high resistive layer and approaching to boundary.

a) Distance inversion from the real part of the H_{zx}

Table 2 Distance inversion table (H_{zx} _real, R_1:R_2 = 1:10)

Distance (ft)	H_{zx} _real(Abs)	Voltage (nV)	Inversion Results (ft)	Error (%)
5.0	**0.0006**	**192**	**4.1414**	**17.17**
4.0	**0.0007**	**224**	**4.0518**	**1.30**
3.0	**0.0031**	**992**	**3.0444**	**1.48**
2.0	**0.0111**	**3552**	**2.0489**	**2.45**

Table 2 shows the inversion results, when the logging points are located at 5.0, 4.0, 3.0, and 2.0 ft. away from the boundary. The real parts of the Hzx are all within the detectable range. The results show that when the distance from the drilling bit to the boundary is within four ft., the inversion method can find the distance accurately. However, when the distance between the drilling bit and the boundary is close to five ft.

or higher, the inversion process gives higher error. Figure 4.6 shows the real and imagine parts of the cross component Hzx in the range from four to ten ft. It's clear that, starting from five ft., the real part of Hzx is not monotonic. There exist two roots of Equation 47. This is why the error becomes larger around this depth.

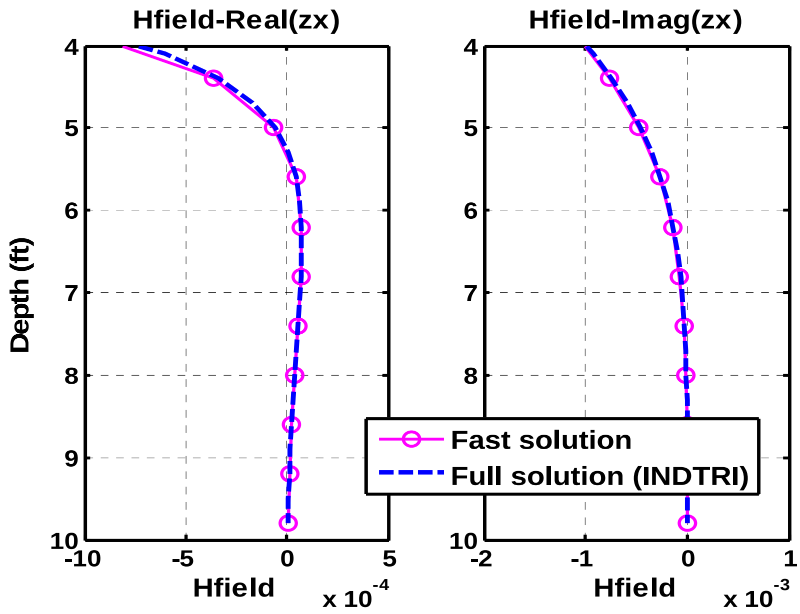

Figure 4.6 Zoom in cross component H_{zx} of tool response

b) Distance inversion from the amplitude of the H_{zx}

To solve the problems appearing in case (a), the amplitude of H_{zx} is used in the distance inversion. Figure 4.7 gives the amplitude of the cross component H_{zx}. It show that the amplitude of H_{zx} has a single value in each side of the boundary. The curve is monotonic. Figure 4.8 is the zoom in figure of the amplitude in the range from four ft. to ten ft. It's obvious that, the curve is monotonic and is always larger than zero. Then, the boundary distance is inversed based on the amplitude of the cross component H_{zx}.

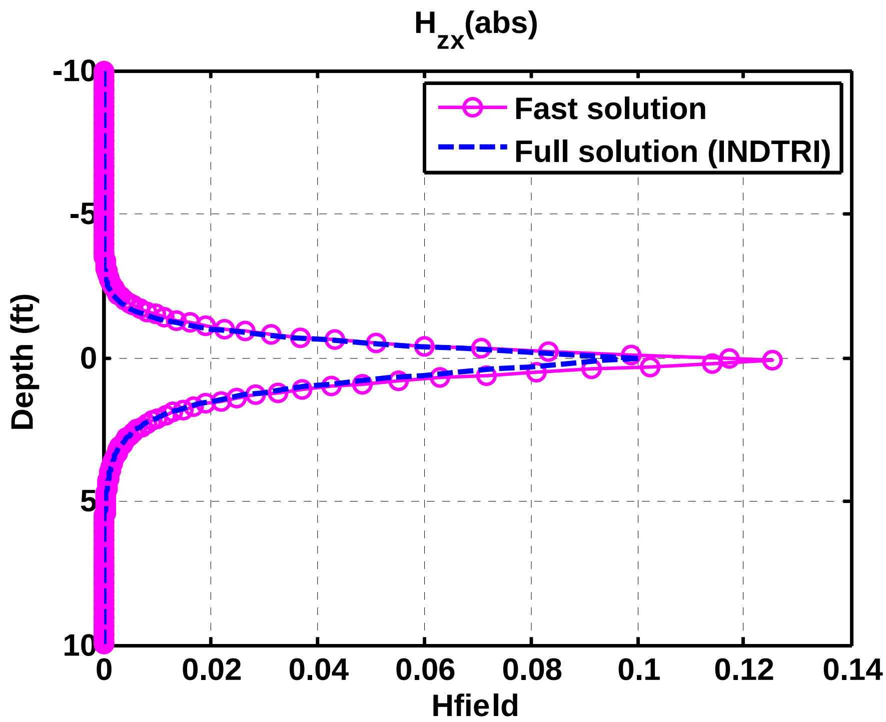

Figure 4.7 Amplitude of the cross component H_{zx}

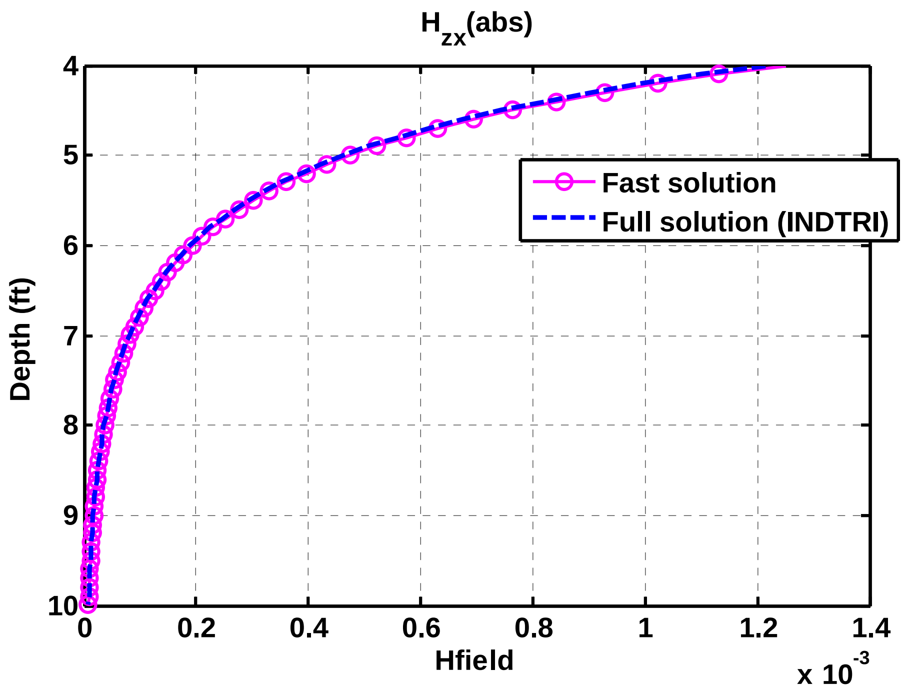

Figure 4.8 Zoom in amplitude of the cross component H_{zx}

Table 3 Distance inversion table (Hzx _abs, R1:R2 = 1:10)

Distance (ft)	H_{zx} (Abs)	Voltage (nV)	Inversion Results (ft)	Error (%)
10.0	7.7888e-06	2.4924	10.0418	0.42
9.0	1.6558e-05	5.2985	9.0403	0.45
8.0	3.6071e-05	11.5427	8.0394	0.49
7.0	8.1004e-05	25.9213	7.0392	0.56
6.0	0.0002	64.00	6.0384	0.64
5.0	0.0005	160.00	5.0390	0.78
4.0	0.0012	384.00	4.0381	0.95
3.0	0.0035	1120.00	3.0401	1.34
2.0	0.0111	3552.00	2.0502	2.51
1.0	0.0379	12128.00	1.0983	9.83

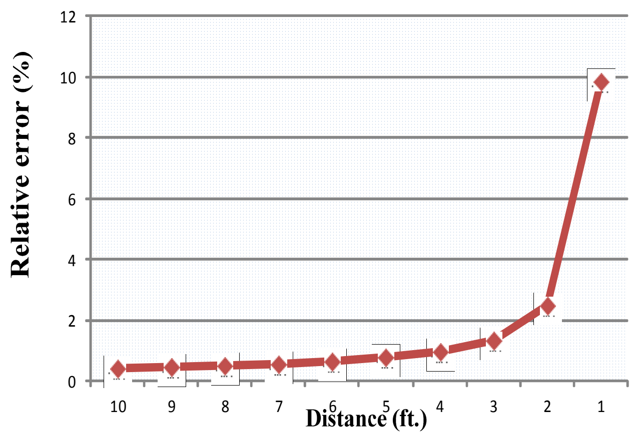

Figure 4.9 Relative error of the inversion results (H_{zx} _abs, R_1:R_2 = 1:10)

Table 3 shows the inversion results based on the amplitude of H_{zx}. Compared with the results in Table 2, the inversion method based on amplitude of H_{zx} is faster and more accurate. The algorithm can even handle the case when the logging point is 10 ft. away from the boundary and keeps the relative error within 1%.

Figure 4.9 shows the relative error of the inversion results in Table 3, which shows that, when the drilling bit is located in the range four to ten ft. away from the boundary, the relative error of the boundary distance inversion is within 1%. When the drilling bit is close to the boundary, within the area two to four ft. away from the boundary, the relative error is larger, but still within 3%. When the drilling bit moves to the area one ft. away from the boundary, the boundary distance inversion is not as accurate. The relative error goes up to 10%. That is because the complex image theory does not work well around boundary. For the two-layer formation, shown in Figure 4.4, considering the minimum detectable voltage 100nV, for the transmitter antenna with 3.2e5 A.m, the detectable distance is about six ft. Neglect the limitation of minimum detectable voltage, the inversion process can work even when the logging point is 10 ft. far away to the boundary.

4.5.3 R_1 = 1 Ohm.m, R_2 = 100 Ohm.m

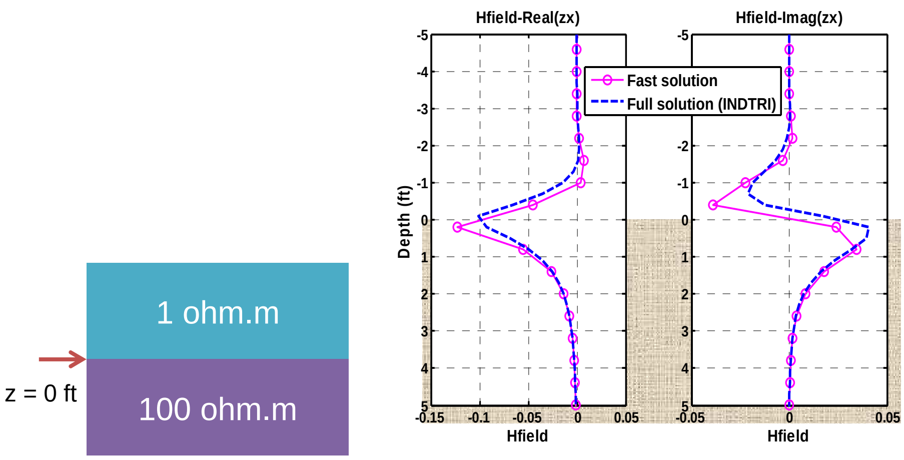

Figure 4.10 Testing model of inversion processing (R_1:R_2 = 1:100)

Table 4 Distance inversion table (${H_{zx}}$ _abs, R_1:R_2 = 1:100)

Distance (ft)	Hzx (Abs)	Voltage (nV)	Inversion Results (ft)	Error (%)
10.0	8.9276e-05	28.57	10.0135	0.14
9.0	1.3812e-04	44.20	9.0141	0.17
8.0	2.2105e-04	70.74	8.0147	0.18
7.0	3.6903e-04	118.09	7.0160	0.23
6.0	6.4986e-04	207.96	6.0166	0.28
5.0	12.2592e-04	392.29	5.0179	0.36
4.0	25.3043e-04	809.74	4.0196	0.49
3.0	58.7665e-04	1880.53	3.0227	0.76
2.0	0.0158	5056.00	2.0320	1.60
1.0	0.0476	15232.00	1.0740	7.40

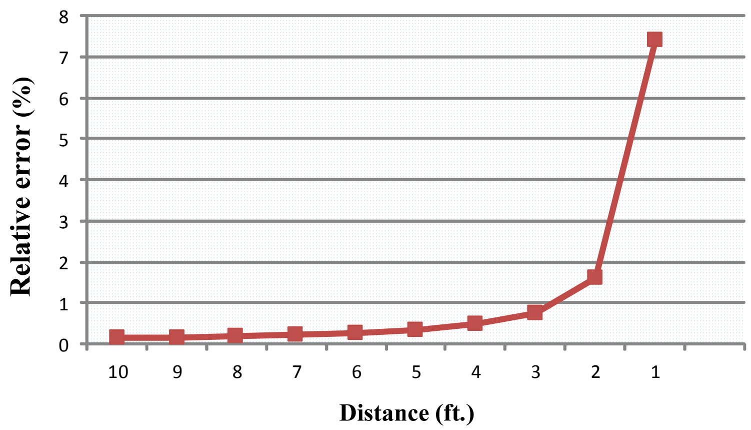

Figure 4.11 Relative error of the inversion results (${H_{zx}}$ _real, R_1:R_2 = 1:100)

Similar as 4.5.1, re-test the inversion method in the case when the lower layer is 100 Ohm-m and the upper layer is 1 Ohm-m. The boundary is still at z = 0. Figure 4.10 shows the formation model and the simulation results.

Table 4 shows the comparison between the inverted distance and actual distance. The results show that the inversion results are pretty close to the actual distance. Except the logging point at one ft. away from boundary, which is very close to the boundary, in the distance range from two to ten ft., the relative error stays within 2% as is shown in Figure 4.11.

Re-plot the relative error curves of the two cases in Figure 4.12. It shows that when the conductivity contrast of the two layers is larger, the relative error of the inversion results is smaller. That agrees with the discussion in Chapter 4.

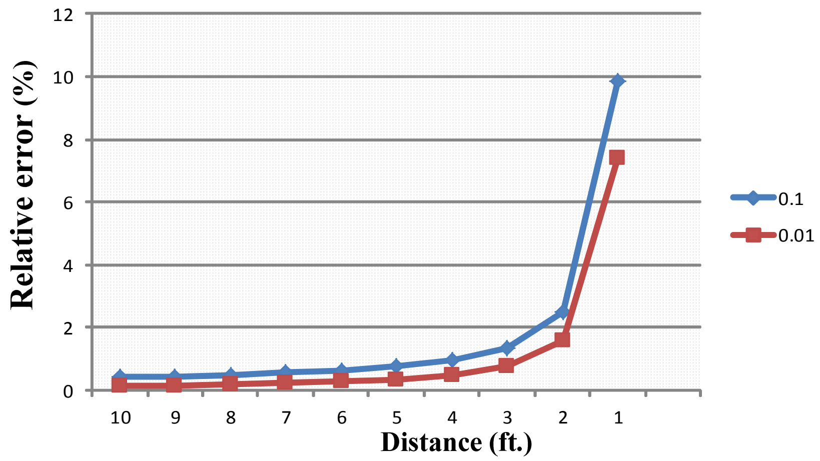

Figure 4.12 Comparison of the relative error in different formation

4.6 Simulation Results with Noise added

The behavior of the inversion method in the presence of noise and error is also evaluated. To simulate the noise, an array of random number between -1 and +1 was generated using a white-noise generator. This array was scaled to 1% to 10% of the minimum detectable voltage 100 nV. Convert the voltage to the H field. The array was scaled to 1% to 10% of 3.125e-04. Use the scaled array as a noise. Add this noise to the data simulated from the analytical full solution as a measured data. Then plug this data into the inversion processing. By iterating the forward modeling developed based on the complex image theory, calculate the distance away from the boundary.

4.6.1 R_1 = 1 Ohm.m, R_2 = 10 Ohm.m

Considering the effect of noise, re-process the two-layer model in Figure 4.3. Table 5 shows the cross component with 1% noise and the inversion results generated using the noised data. The inversion results show that, less than 1% noise, the inversion method still gives reliable result. The relative error between the inversed distance and the accurate distance stays within 3%.

Table 6 shows processing results, when the noise is increased to 5%. In this case, because the added noise is at the same order of the ideal data far from the boundary, the noise causes higher error to the inversion results. The relative errors of the logging points within six ft. away from boundary still remain within 3%. For logging points away from boundary for more than six ft., the relative error can be as high as 20%.

Figure 4.13 shows the curves of relative error when different percentages of noise are added to the ideal data. It's easy to see that when the added noise is increasing, the relative error is larger. The noise effects more in the area relatively further away from boundary than the area close to the boundary. That is because, in noise study, the noise level is fixed, but for a fixed level of transmitter power, the received signal reduces a lot as the distance from the boundary is enlarged. The noise has more effect in the area further away from the boundary.

Table 5 Distance inversion table with 1% noise added (H_{zx} _abs, R_1:R_2 = 1:10)

Distance (ft)	H_{zx} _ideal (Abs)	Voltage (nV)	H_{zx} _noise (1%)	Inversion Results (ft)	Error (%)
10.0	7.7888e-06	2.4924	6.7448e-06	9.8850	1.15
9.0	1.6558e-05	5.2985	1.9574e-05	9.0272	0.30
8.0	3.6071e-05	11.5427	3.5953e-05	8.0038	0.05
7.0	8.1004e-05	25.9213	7.8162e-05	7.0756	1.08
6.0	1.8906e-04	64.00	1.8968e-04	6.0496	0.83
5.0	4.6384e-04	160.00	4.6693e-04	5.0448	0.90
4.0	1.2157e-03	384.00	1.2137e-03	4.0403	1.01
3.0	3.4783e-03	1120.00	3.4781e-03	3.0401	1.34
2.0	1.1089e-02	3552.00	1.1092e-02	2.0502	2.51

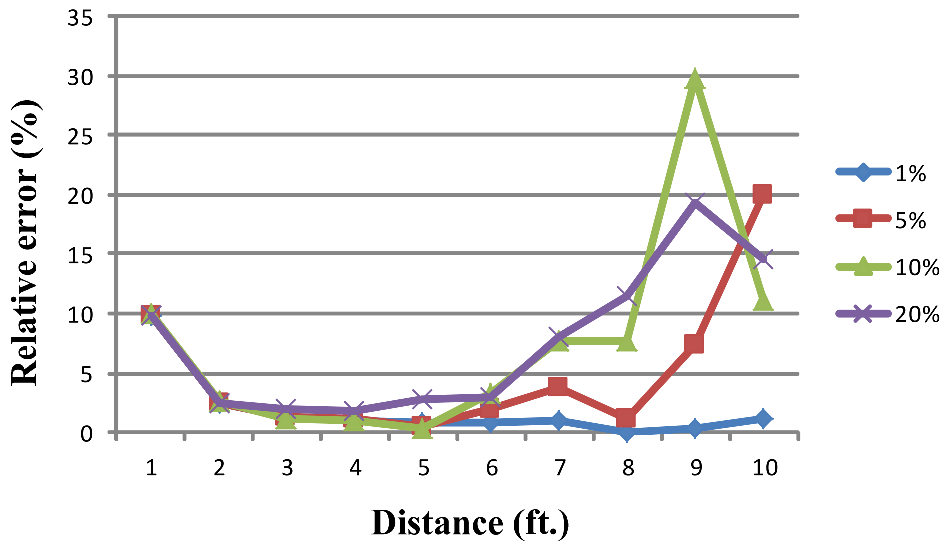

Figure 4.13 Relative error with different noise added (R_1:R_2 = 1:10)

Table 6 Distance inversion table with 5% noise added (H_{zx} _abs, R_1:R_2 = 1:10)

Distance (ft)	**H_{zx} _ideal (Abs)**	**Voltage (nV)**	**H_{zx} _noise (5%)**	**Inversion Results (ft)**	**Error (%)**
10.0	**7.7888e-06**	**2.4924**	**7.1562e-06**	**12.0000**	**20**
9.0	**1.6558e-05**	**5.2985**	**2.4941e-05**	**8.3353**	**7.38**
8.0	**3.6071e-05**	**11.5427**	**3.8697e-05**	**7.9036**	**1.21**
7.0	**8.1004e-05**	**25.9213**	**6.8256e-05**	**7.2593**	**3.70**
6.0	**1.8906e-04**	**64.00**	**1.7833 e-04**	**6.1237**	**2.06**
5.0	**4.6384e-04**	**160.00**	**4.7825e-04**	**5.0273**	**0.55**
4.0	**1.2157e-03**	**384.00**	**1.2240e-03**	**4.0483**	**1.21**
3.0	**3.4783e-03**	**1120.00**	**3.4874e-03**	**3.0401**	**1.34**
2.0	**1.1089e-02**	**3552.00**	**1.1088e-02**	**2.0505**	**2.53**

4.6.2 R_1 = 1 Ohm.m, R_2 = 100 Ohm.m

For the two-layer model shown in Figure 4.10, where the conductivity of low medium is 100 Ohm-m, compared with the two-layer model in Figure 4.3, where the conductivity of low medium is 10 Ohm-m, the received cross component has larger amplitude at the relative far area. For example, at the observation point 10 ft. away from the boundary, in the case with 100 Ohm-m lower medium, the amplitude of the cross component is 8.9276e-05 In the case with 10 Ohm-m lower medium, the amplitude of the cross component is only **7**.7888e-06 which is one magnitude lower That means, in the same noisy environment, the logging tool has better performance in the case with larger conductivity contrast. This conclusion agrees with the results shown in the section 3.4.

Since in the high conductivity contrast formation, the cross component is stronger. The amount of noise in this formation is started to be added from 5%.

Table 7 shows the ideal data of the cross component, data with 5% noise of the cross component, inversion distance generated from the noised data as measurements and the relative errors between the inversed distance and real positions of the logging points.

Figure 4.14 shows the curves of relative error when the added noise is increased to 10%, 20% and 50%. It shows that, when the noise is increased to 20%, in the most area, the relative error of the inversion distance still remains within 5%. When the noise is increased to 50%, there is huge error for the testing logging points six ft. or further away from boundary. Within six ft., the relative errors are always less than 5%.

Table 7 Distance inversion table with 5% noise added (H_{zx} _abs, R_1:R_2 = 1:100)

Distance (ft)	H_{zx} (Abs)	Voltage (nV)	H_{zx} _noise (5%)	Inversion Results (ft)	Error (%)
10.0	8.9276e-05	28.57	8.5212e-05	9.8007	1.99
9.0	1.3812e-04	44.20	1.4027e-04	9.1521	1.69
8.0	2.2105e-04	70.74	2.2331e-04	8.0140	0.18
7.0	3.6903e-04	118.09	3.6820e-04	6.9739	0.37
6.0	6.4986e-04	207.96	6.5107e-04	5.9904	0.16
5.0	1.2259e-03	392.29	1.2238e-03	5.0085	0.17
4.0	2.5304e-03	809.74	2.5257e-03	4.0163	0.41
3.0	5.8767e-03	1880.53	5.8691e-03	3.0256	0.85
2.0	1.5786e-02	5056.00	1.5799e-02	2.0320	1.60

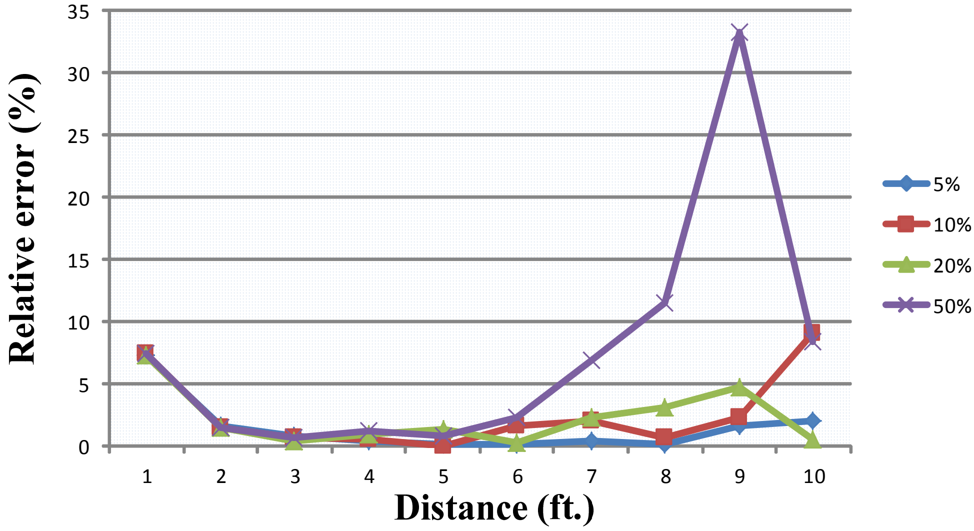

Figure 4.14 Relative error with different noise added (R_1:R_2 = 1:100)

Chapter 5 Conclusion

Image theory, as a method used to simplify the inhomogeneous media, can be applied in Geo-steering to speed up the simulation. The advantage of this theory is the simplicity in formulation and fast in computation.

The complex image approximation method was tested at 2 MHz and 400 KHz respectively. Compared with the full solution results, the complex image method has very good agreement at both frequencies. Error only occurs near boundary. However, in the application of geo-steering, the error is acceptable. It works better at higher frequencies than lower frequencies. This is because when the frequency is higher, the skin depth of the formation is shorter, which is closer to a perfect conductor, and therefore the image theory is more accurate.

The accuracy of the complex image theory also depends on the conductivities of both layers. When the conductivity difference between the upper layer and the lower layer increases, the error decreases. The absolute error and relative error are collected at different observation points. The error is larger when the drilling bit is closer to the boundaries. For the 2MHz tool, when the logging point is more than two ft. away from the boundary, the relative error is less than 10%. For the 400 KHz tool, this distance is increased to three ft. Compared with the full solution method, the complex image approximation method can significantly speed up the simulation. In the testing with 1000 iteration and 600,000 logging points in total, the complex image method is more than 100 times faster than the full solution. This difference in efficiency is also enlarged along with the increase of the logging point. This method can be used in real time data inversion of the distance to boundary computation in a geo-steering system.

Effects of frequency and spacing are investigated. For one turn antenna, with area $2.5in^2$ and excited by 200 mA, the general detectable distance in high resistive layer is about five ft. When tool is working at 400 KHz, longer spacing gives larger detectable distance. The simulation shows that when the spacing is 55 in., the detectable distance is about seven ft.

Inversion process is given in last part. Two-layer model with boundary at z = 0 is tested. Boundary distance is inversed based on the amplitude curve of the cross component H_{zx}. The inversion results show that the inversion code works well in the distance range from two to ten ft. The relative error is kept in 2%. By comparing the relative error form different formation combination, it can be concluded that larger conductivity contrast of the formation contributes more accurate inversion results.

The effect of noise was discussed in inversion processing. A random white noise with amplitude 100 nV, scaled from 1% to 50%, was added into the analytical full solution data to test the anti-noise capacity. The relative errors of inversion results generated using ideal data with different amount noise added in two different formations are calculated and plotted. The results show that the proposed method is more robust in formations with higher conductivity contrast. Compared with the area relatively further away from the boundary, the relative error can be kept in a lower range in the area within six ft. away from the boundary.

Reference

[1] Z.Z Zhang, “1D Modeling and Inversion of Triaxial Inductional Logging Tool in Layered Anisotropic Medium”, University of Houston, 2011

[2] Q. Li, D. Omeragic, L. Chou, L. Yang, K. Duong, J. Smits, J. Yang, T. Lau, C. Liu, R. Dworak, V. Dreuillault and H. Ye, "New directional electromagnetic tool for proactive geo-steering and accurate formation evaluation while drilling," 46th SPWLA Annual Logging Symposium, Paper UU, 2005.K. Elissa, “Title of paper if known,” unpublished.

[3] D. Omeragic, T. Habashy, C. Esmersoy, Q. Li, J. Seydoux, J. Smits and J. R. Tabanou, "Real-time interpretation of formation structure from directional EM measurements," SPWLA 47th Annual Logging Symposium, June 4-7, 2006.

[4] T. Wang, H. Meyer and L. Yu, "Dipping bed response and inversion for distance to bed for a new while-drilling resistivity measurement," SEG New Orleans 2006 Annual Meeting, pp. 416-420, 2006.

[5] M.S. Ifnik, M. Hamawi, A. Shamri, A. Madjidi, C. Shade, ”Using New Advances in LWD technology for Geosteering and Geologic Modeling,” SPE/IADC 57537, 1999.

[6] M. Dautel, J. Pitcher and M. Bittar, “Modern Azimuthal Resistivity Tools and Their Application to Mature Field Development”, SPWLA-INDIA 3rd Annual Logging Symposium, Mumbai, India, Nov 25-26, 2011.

[7] M. Bittar, J. Klain, G. Hu, J. Pitcher, C. Golla, G. Althoff, M. Sitka, V. Minosyan and M. Paulk, "A new azimuthal deep-reading resistivity tool for geo-steering and advanced formation evaluation," SPE Annual Technical Conference and Exhibition, SPE 109971, 2007.

[8] J. R. Wait, "Image theory of a quasi-static magnetic dipole over a dissipative half-space," Electron. Letter. Vol. 5, No. 13, pp. 281-282, June, 1969.

[9] P. R. Bannister, "Summary of image field expressions for the quasi-static fields of antennas at or above the earth's surface," Proceedings of the IEEE, Vol. 67,No. 7, July, 1979.

[10] I. V. Lindell and E. Alanen, "Exact image theory for the Sommerfeld half-space problem, Part I: Vertical magnetic dipole," IEEE Trans. Antennas Propagateion, Vol. AP-32, No. 2, pp. 126-133, February, 1984.

[11] Q. Z. Dong and T. Wang, "A fast forward model for simulating a layered medium using the complex image theory," SEG San Antonio 2011Annual Meeting, pp. 573-577, 2011.

[12] J.A Stratton, "Electromagnetic Theory," pp. 573-587, McGraw-Hill Book Company, Inc., New York, 1941.

[13] Roy Harold Lien, "Radiation from a Horizontal Dipole in a Semi-Infinite Dissipative Medium," Applied Physics, Vol. 24, No. 1, January, 1953.

Appendix I IMAGE 12 USER MANUAL

I.1 Application

IMAGE12 is a fast forward modeling code for the LWD tool response used in geo-steering, by applying the complex image theory. As shown in Figure I.1, in geo-steering, well is horizontal. The logging points will be along the depth direction, as shown in Figure I.1. The output file has the tool response versus depth, while the dipping angle is 90 degree and spacing is unchanged.

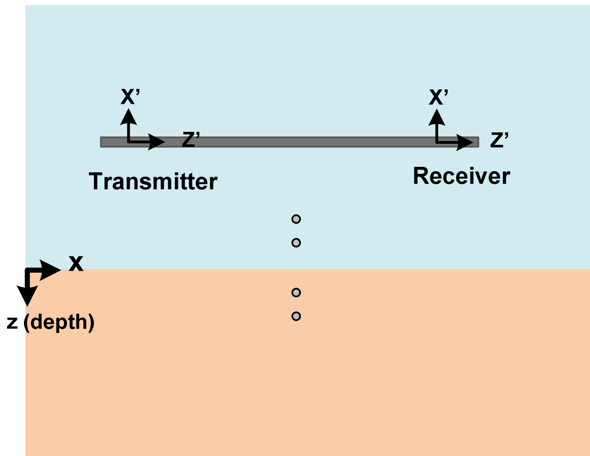

Figure I. 1 A tool is located horizontally in the production layer

The code is based on the complex image theory. The restriction is that the transmitter is required to be within the relative high resistivity layer (compared with other boundary layers). However, in most geo-steering application, logging tool is kept in the oil or gas layer, which is of relatively higher resistive. In addition, only two or three layers media could be calculated. Compared with the full solution results, there is noticeable error when the logging tool is approaching to the boundary. The computation speed is improved extremely compared with the full solution. Detailed theory can be found in the 2012 Well Logging Lab progress report.

I.2 Input and Output Files

I.2.1 Input files

There are two input files required by the code IMAGE12: frm.in and diptool.in.

Input File 1: frm.in

In the input file frm.in, users can define the information of the formation (such as the dip, azimuth and tool angle, number of layers, conductivities, permittivity and permeability of each layer and the boundary position of each layer) and the starting, ending and step of the observation points according to their requirements.

The format of **frm.in** is as follows:

```
AngA, AngB, AngC
    Layer
    Sig(1),Epr(1),Mu(1)
    Sig(2),Epr(2),Mu(2),Hp(1)
    ……
    Sig(Nlayer),Epr(Nlayer), Mu(Nlayer),Hp(Nlayer-1)
    Zstart,Zstep, Zfinal
```

where

AngA = the dip angle in degrees

AngB = the azimuth angle in degrees

AngC = the tool rotation angle in degrees

Layer = the number of layers in the formation

Sig(i) = the conductivity of the i^{th} layer, S/m

Epr(i) = the relative permittivity of the i^{th} layer

Mu(i) = the relative permeability of the i^{th} layer

Hp(i) = the position of the lower boundary of the i^{th} layer along the borehole, the unit is ft.

Zstart = the depth of the starting receiver point, in ft.

Zstep = the step depth of the receiver points, in ft.

Zfinal = the depth of the ending receiver point, in ft.

It should be noted that in the input file, the layer is numbered from top to bottom and all the depths are apparent depth (measured depth) along the tool.

Input File 2: diptool.in

The format is as follows:

```
FREQ
NBCT, NBCR
TTM(i), ZTM(i)    (1≤i≤NBCT)
…
TRE(i), ZRE(i)    (1≤i≤NBCR)
```

where

FREQ = The operating frequency of the tool

NBCT = number of transmitter coils.

NBCR = number of receiver coils.

TTM(i) = number of turns of the i^{th} transmitter coil

ZTM(i) = position of the i^{th} transmitter with respective to the tool center, in inch

TRE(i) = number of turns of the i^{th} receiver

ZRE(i) = position of the i^{th} receiver with respective to the tool center, in inch

This software can handle multi transmitter and receiver coils. The input file diptool.in is used to input the information of the tool, such as number of transmitter and receiver coils, number of turns of each coil and positions of the transmitter and receiver coils.

I.2.2 Output files

At the completion of program execution of the code, two output files named Hfield.dat and app_cond.dat will be generated.

Output File 1: Hfield.dat gives the magnetic field responses of the tool. There are 20 columns in the file. The first column is the apparent depth of all observation points in ft., the second column is the true depth of all observation points in ft., the third to twentieth columns give the real and imaginary part of all nine components of the magnetic fields, i.e., Real(Hxx), Imag(Hxx), Real(Hxy), Imag(Hxy), Real(Hxz), Imag(Hxz), Real(Hyx), Imag(Hyx), Real(Hyy), Imag(Hyy), Real(Hyz), Imag(Hyz), Real(Hzx), Imag(Hzx), Real(Hzy), Imag(Hzy), Real(Hzz), Imag(Hzz).

<u>**Output File 2:**</u> Output file app_cond.dat gives the apparent conductivity calculated from the magnetic fields. The format of the file is the same as Hfield.dat. The unit of the apparent conductivity is S/m.

I.3 Examples

The following examples show the use of these computer codes.

Example 1. A 2-layered formation

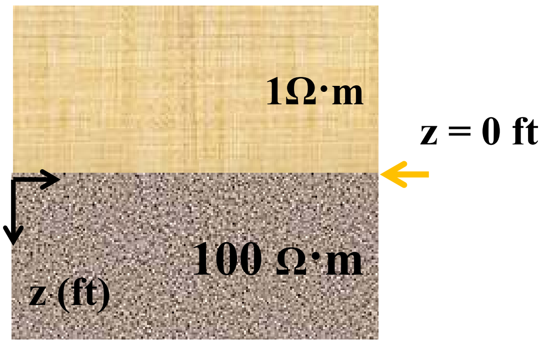

Figure I. 2 Two-layer model

The formation data for this example are:

2 layers

Dip angle (degree) Azimuth angle (degree)

Rotation angle (degree)

89.9 0

0

Conductivities(S/m)	Permittivity(f/m)	Permeability(h/m)
1	10	1
0.01	10	1

The input files are as follows:

Diptool.in

```
    2000000.0
               1             1
               1        11.00000
               1       -36.37500
```

frm.dat

```
89.9     0     0
               2
1.0000     1.000     1.000
0.01000    1.000     1.000     0
      -5     0.3     5
```

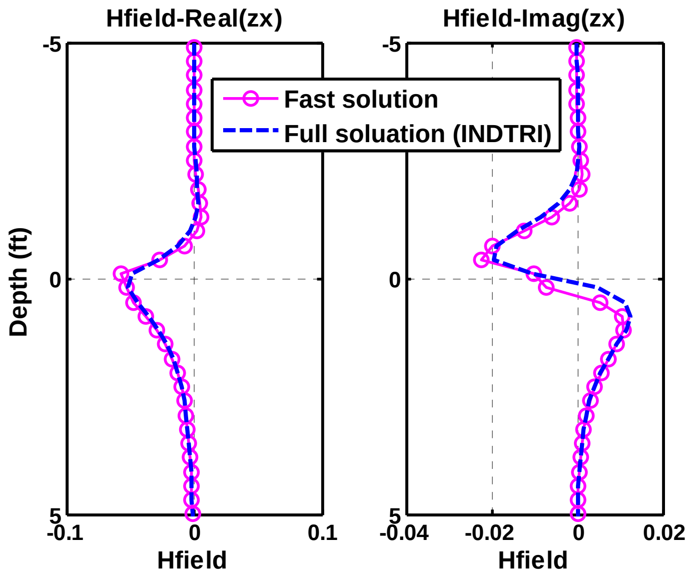

Figure I. 3 *zx* component of the 2-layered model

Example 2. A 3-layered formation

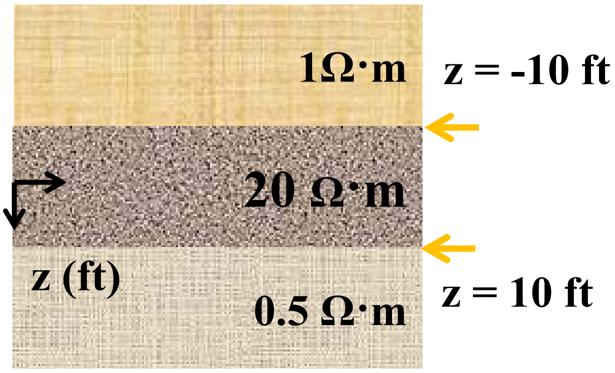

Figure I. 4 Three-layer model

The formation data for this example are:

3 layers

Dip angle (degree) Azimuth angle (degree)

Rotation angle (degree)

89.9 0

0

Conductivities(S/m)	Permittivity(f/m)	Permeability(h/m)
1	10	1
0.05	10	1
2	10	1

The input files are as follows:

<u>Diptool.in</u>

```
2000000.0
      1        1
      1     11.00000
      1    -36.37500
```

frm.dat

89.9 0 0

3

1.000000 10.00000 1.000000

0.05 10.00000 1.000000 -10

2.000000 10.00000 1.000000 10

-10 0.3 10

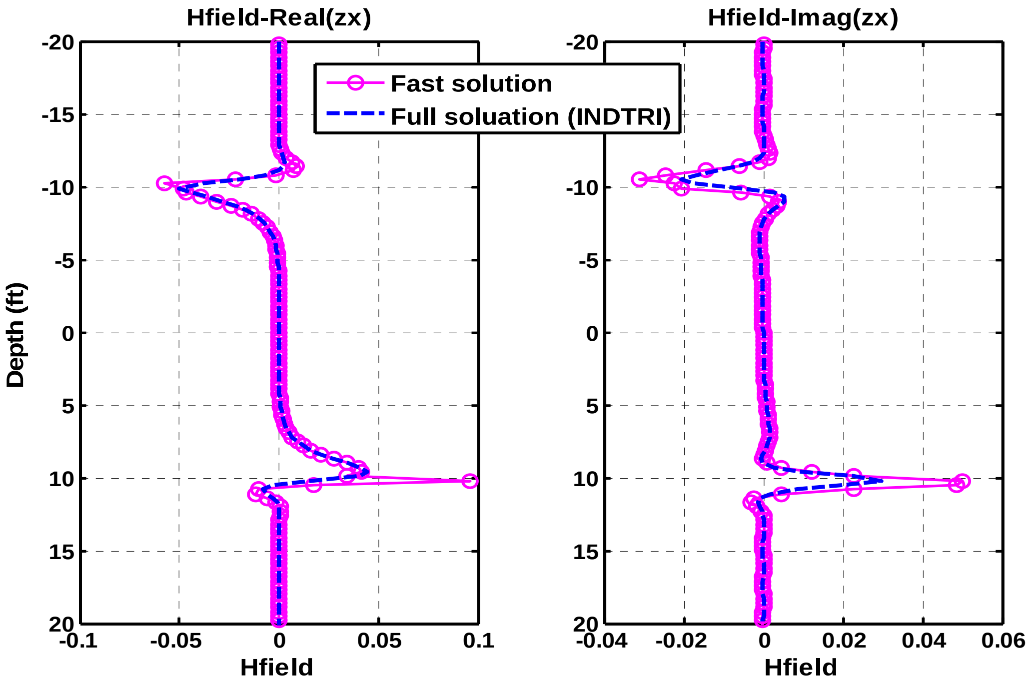

Figure I. 5 *zx* component of the 3-layered model

I.4 Limitation

This code now only works in isotropic formation and horizontal well, which means the dipping angle should be kept in 89.9°. The number of formation layers should be less than 3. The code can only handle the tool with one transmitter and one receiver. Error may occur around boundaries. Accuracy varies along with different frequencies and difference formations.